PROPAGATION OF 1-10 MeV SOLAR FLARE PROTONS IN INTERPLANETARY SPACE

Thesis by

Stephen S. Murray

In Partial Fulfillment of the Requirements

For the Degree of

Doctor of Philosophy

California Institute of Technology

Pasadena, California

1971

(Submitted 28 December 1970)

ACKNOWLEDGMENTS

I wish to express my gratitude to Professor Edward C. Stone who was my faculty sponsor and suggested this research project, and provided guidance and encouragement throughout its duration.

My thanks are also extended to Professor Rochus E. Vogt, who is co-investigator on the OGO-VI experiment, and with whom I have had many stimulating discussions. It is also a pleasure to acknowledge rewarding discussions with Professor J. R. Jokipii, Professor L. Davis, Jr., Dr. J. L. Fanselow, Dr. D. S. Intriligator and Messrs. J. E. Lupton, G. J. Hurford, T. L. Garrard and L. C. Evans.

The experiment was built through the joint efforts of the personnel of the Space Radiation Laboratory, the staff of Central Engineering Services and the staff of Analog Technology Corporation. I also appreciate the skilled workmanship of the personnel of the Bridge Laboratory Machine Shop under Mr. David Vail.

The success of the OGO-VI experiment is due in part to the efforts of Messrs. William Althouse and William Blodgett in the design, construction and testing of the electronics system of the experiment and the ground support equipment.

Thanks are due to Professor R. L. Walker for extending the privilege of using the external electron beam of the Caltech Synchrotron for detector calibrations, and to the members of the synchrotron staff. Also, thanks are due to Professor C. A. Barnes for allowing us the use of the Caltech Tandem Van de Graaff Accelerator, and to the members of the accelerator staff.

I also wish to thank the staff at TRW Systems, Inc. responsible for the OGO spacecraft, and in particular my thanks to Mr. Victor Sculteure who was the engineer assigned to this experiment. Finally I am appreciative of the fine work done by all those associated with the National Aeronautics and Space Administration OGO Project Office.

I am indebted to the National Aeronautics and Space Administration, the National Science Foundation and the California Institute of Technology for financial aid during my graduate studies. The research described in this thesis was supported by the National Aeronautics and Space Administration under grants NGR-05-002-160 and NGL-05-002-007, and contract NAS5-9312.

ABSTRACT

Observations of 1-10 MeV solar flare protons associated with the 7 June 1969 solar event are used in an investigation of the physical processes affecting particle propagation in interplanetary space. The observations were made with the Caltech Solar and Galactic Cosmic Ray Experiment on board OGO-VI, a low altitude polar orbiting satellite. We find during the decay of the event that the physical processes of diffusion, convection and energy change must all be considered to obtain satisfactory agreement between the observations and theoretical predictions. In particular we find that for this event, there is clear evidence for energy change processes occurring in interplanetary space. We find in fact that the observed energy change is not simply due to adiabatic deceleration in a uniformly expanding solar wind. We also find that during the decay of this event the effects of diffusion are consistent with an energy independent diffusion coefficient $\kappa_{\parallel}$ for 1-10 MeV with a value of approximately 5×10^{20} cm^2/sec.

To Judith

TABLE OF CONTENTS

LIST OF TABLES

LIST OF FIGURES

I. INTRODUCTION

Knowledge of the physical processes involved in the propagation of energetic charged particles in the interplanetary medium is one of the fundamental goals of cosmic ray physics. An understanding of these processes bears upon those astrophysical problems which are investigated through observations of cosmic rays near the earth. Such observations do not result directly in the interstellar cosmic ray spectrum. Rather, they reflect the effects of solar modulation due to the propagation properties of the solar wind. [A review of solar modulation is given by Webber (1).]

The propagation of energetic particles in the solar wind can be studied through observations of galactic cosmic rays, over long periods of time, near the earth, in which case the quasi-steady state properties of interplanetary space are investigated. Alternatively, investigation of the propagation of solar cosmic rays leads to observations of more transient phenomena which provide another viewpoint for the study of the interplanetary medium. In this thesis we will discuss observations of the latter type, specifically the propagation of solar flare protons in the energy range 1-10 MeV for a solar flare which occurred on 7 June 1969.

Theoretical considerations of the physical processes which affect the transport of cosmic rays in the interplanetary medium have resulted in considerable progress in our understanding of these processes. The beginnings of the modern theoretical approach to this problem can be found in the work by Fermi (2) in 1949 in which a statistical approach to cosmic ray propagation was first suggested. In the 21 years that have followed, the basic transport processes of diffusion, convection and energy change have been incorporated in theoretical models which attempt to describe the transport of energetic particles in a turbulent magnetic plasma such as the solar wind. [For a review of this theoretical development see references (3, 4, 5).] By 1963 (4), the current picture of the interplanetary medium was essentially in its present form, and the basic concept of the solar wind as a medium in which energetic particles diffuse was well established. The additional concepts of convection and energy change were already contained in this picture and were explicitly pointed out by Parker (6) in 1965, and Gleeson and Axford (7) in 1967. The possibility of anisotropic diffusion due to the average direction of the interplanetary magnetic field was also discussed by these authors.

The relationship of the cosmic ray diffusion tensor ($\underline{\underline{\kappa}}$) to the interplanetary magnetic field power spectrum was

derived by Jokipii (8, 9, 10) in 1966 and 1967, and by others (11, 12). This quantitative relationship between cosmic ray diffusion and the interplanetary magnetic field has made possible the utilization of spacecraft observations in calculating the parameters of theoretical models for particle propagation. The validity of various theoretical models can therefore be tested by a detailed comparison of the theoretical predictions with actual cosmic ray observations.

The observations reported in this thesis represent some of the first detailed measurements at low energies (1-10 MeV) that have been used to study the effects of non-diffusive processes on particle propagation. We shall present results which clearly demonstrate the existence of energy change processes in the propagation of solar cosmic rays. We will also present evidence for the existence and importance of an acceleration process which competes with uniform adiabatic deceleration of cosmic rays in the expanding solar wind. We find in the energy range under consideration (1-10 MeV), that the effects of diffusion cannot be completely neglected and that the component of the diffusion tensor along the average magnetic field is of the same order of magnitude as that calculated by Jokipii (5) from measurements of the magnetic field power

spectrum. In particular we find a value of $\kappa_{\parallel} \sim 5 \times 10^{20} cm^2/sec$ at 10 MeV to be compatible with our observations.

The data discussed in this thesis were derived from an experiment on board the National Aeronautics and Space Administration satellite OGO-VI which was launched from Vandenberg Air Force Base on 5 June 1969.

II. INSTRUMENT

A) General Description

The detector system (13) was designed as a series of three telescopes. Each is optimized for specific performance characteristics so that there is adequate charge and energy resolution over the broad range of incident particle energies being studied. In addition, the experiment must be operable over a large range of incident particle fluxes. An onboard priority system enables the three telescopes to time-share the available electronics and telemetry with a minimum amount of ground control intervention. This insures proper operation of the experiment regardless of the incident flux of particles. If necessary, various alternate modes of operation can be commanded from the ground when desired.

The rapid motion of a polar orbiting satellite through the geomagnetic field limits the collection time for the various rates monitored by an experiment. For playback data (recorded at 8000 bits/sec) on OGO-VI the sampling time for key rates is 431 msec (14). In this time the satellite moves typically 1.5 minutes in latitude. Thus several samples of a rate can usually be averaged to decrease statistical fluctuations without a need to worry about geomagnetic variations. At higher bit rates (real time data) a more detailed study of geomagnetic related phenomena (such as cutoffs) can be made.

The charge (Z) and the incident kinetic energy (E) of a cosmic ray particle can be determined by various combinations of measurements. The choice of the combination used is generally determined by the energy interval of interest. In this experiment we employ measurements of total energy, rate of energy loss, range and velocity. When taken in suitable combinations, these measurements determine Z and E.

In this thesis we will be discussing only data derived from the Range telescope. Thus we will limit further discussion to this part of the experiment and the associated electronics.

B) Description of the Range Telescope

1) Physical

A cross-sectional view of the Range telescope is shown in figure II-1. The telescope consists of seven gold-silicon surface barrier detectors, a cylindrical plastic scintillator and photomultiplier tube and five absorbers. The physical properties of the detectors and absorbers are listed in table II-I. This telescope is designed for making either a simultaneous measurement of energy loss and range, or a measurement of energy loss and total energy, of a cosmic ray particle in the energy range 1-300 MeV/nucleon. The energy lost in detectors D1, D2 and D3 is measured, or the energy lost in D2 and D3 is measured and the range of the incident particle is

Figure II-1

Cross-sectional view of Range telescope

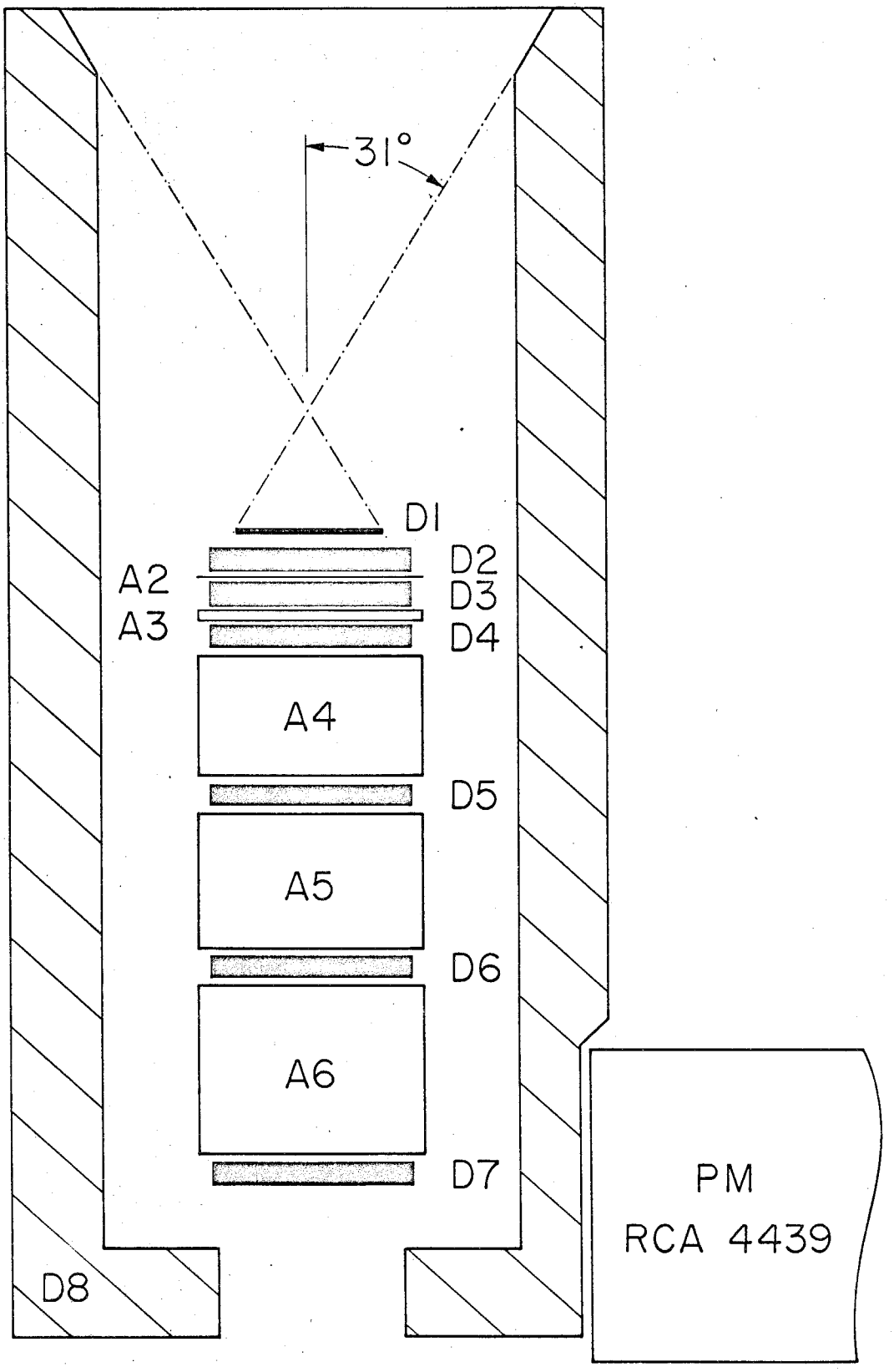
31°
D1
A2
A3
D2
D3
D4
A4
D5
A5
D6
A6
D7
D8
PM
RCA 4439

TABLE II-I

PHYSICAL PROPERTIES OF RANGE TELESCOPE DETECTORS AND ABSORBERS

Detector/Absorber	Thickness[1] mg/cm^2	Area[2] cm^2	Maximum ΔE for Protons[3] MeV
Window (Mylar)	2.32	-	-
D1 (Silicon)	22.1	2.01	3.05
D2 (Silicon)	233	3.80	12.2
A2 (Aluminum)	206	-	-
D3 (Silicon)	227	4.08	12.0

1. Error ±3% due to accuracy of range-energy tables.
2. Error ±6% due to ±3% error in determination of radius.
3. Error ±1% due to measurement error from accelerator calibration. (See Appendix A.)

determined by detection in D4, D5, D6 or D7, which are sandwiched between layers of tungsten. Since this thesis deals only with protons of energy less than that required to reach D4 (45 MeV), we will dispense with further description of the range detectors. The entire range stack is surrounded, except for entrance and exit apertures, by a plastic scintillator anticoincidence cup (D8) which acts as a collimator. The anticoincidence also aids in rejecting events due to nuclear interactions and side showers. The top of the Range telescope is covered with a 3/4 mil (0.00075") aluminized mylar light shield. The low energy threshold of the telescope (1.17 MeV) is due mainly to this shield.

Analysis of an event in the Range telescope for low energy (<45 MeV) protons is normally initiated by a $D1\overline{D8}$ or $D2D3\overline{D8}$ coincidence. For such events no range detector (D4-D7) has been triggered and the experiment reads out the energy deposited in D1, D2 and D3 (even if this is zero). To provide this capability there are three 256-channel pulse height analyzers contained in the experiment.

D1 is a thin detector (~100 microns) which when coupled with the high threshold (~400 keV) of the discriminator insures that D1 is relatively insensitive to electrons. Typical efficiency for D1 to detect electrons is ~1% for 400 keV incident energy (15). For other energies the D1 efficiency decreases. The active area of D1 (~2 cm^2) is less than the

area of D2 (~4 cm^2) so that the geometrical factor for $D1\overline{D8}$ and $D1D2\overline{D8}$ events is the same. Table II-II lists the various events of interest and the threshold energy and the geometrical factor for these events.

2) Detectors

a) Solid State Detectors

As mentioned, there are seven solid state detectors in the Range telescope. These are totally depleted gold-silicon surface barrier detectors manufactured by ORTEC. These were chosen for the high resolution at room temperature and high reliability which they possess. The detectors used in the flight unit were screened for reliability in the thermal-vacuum environment expected on the satellite. Of the detectors which qualified for use in the experiment a further selection was made in that the detectors used have similar depletion depths and active areas (excluding D1). See table II-I for actual values. The depletion depths of the detectors in the flight unit were determined by exposing the assembled Range telescope with flight electronics to the low energy proton beam of the Caltech Tandem Van de Graaff accelerator. Details of this calibration are contained in appendix A.

The thresholds of the discriminators for these detectors (except D1) were set so that at least 99% of all minimum ionizing charge 1 particles trigger the discriminator. Thus

TABLE II-II

RANGE TELESCOPE EVENTS

Event	Threshold Energy[1]	Geometrical Factor[2]
$D1\overline{D8}$	1.17 MeV±1%	1.14 cm^2-sterad ±6%
$D1D2\overline{D8}$	3.31 MeV±1%	1.14 ±6%
$D2D3\overline{D8}$	17.9 MeV±1%	1.62 ±6%

1. Error due to measurement errors during accelerator calibration. (See Appendix A.)
2. Error due to 3% uncertainty in radius.

the desired discriminator threshold is a function of the detector thickness. Due to practical limitations in the electronic adjustment of these levels, it was not always possible to set thresholds to the desired value. However, in all cases the thresholds are sufficiently low for 99% or better efficiency while still above the noise level of the detector and amplifier. The theoretical energy loss distribution (16) for a minimum ionizing muon (~500 MeV) in D2 (233 mg/cm^2 thick) is shown in figure II-2, along with an actual distribution due to cosmic ray muons at ground level. The arrows on the plot indicate the 99% and actual thresholds.

b) Anticoincidence Scintillator

The anticoincidence shield is a cylindrical cup open on the bottom. The light output of this scintillator (NE 102, 0.375" thick) is coupled through a 0.024 inch gap to an RCA 4438 photomultiplier tube. The PM tube used was selected from a group on the basis of a high signal to noise ratio when tested with a NaI crystal and a Cs^{137} source. The selected tube was potted in an aluminum housing with the voltage divider chain wired on to the end of the tube. The completed assembly (scintillator and PM tube) was then tested using ground level cosmic ray muons which were collimated with a 3-fold coincidence telescope as shown in figure II-3. The response of the PM tube was pulse height analyzed for

Figure II-2

Energy loss distribution in D2 (233 mg/cm^2 Si) for muons. Theoretical curve is computed according to Symon (16) for 500 MeV muons. Data are from cosmic ray muons observed at ground level. $\frac{\Delta P(E)}{\Delta E}$ is the probability (percent per MeV) of an energy loss between E and E + ΔE.

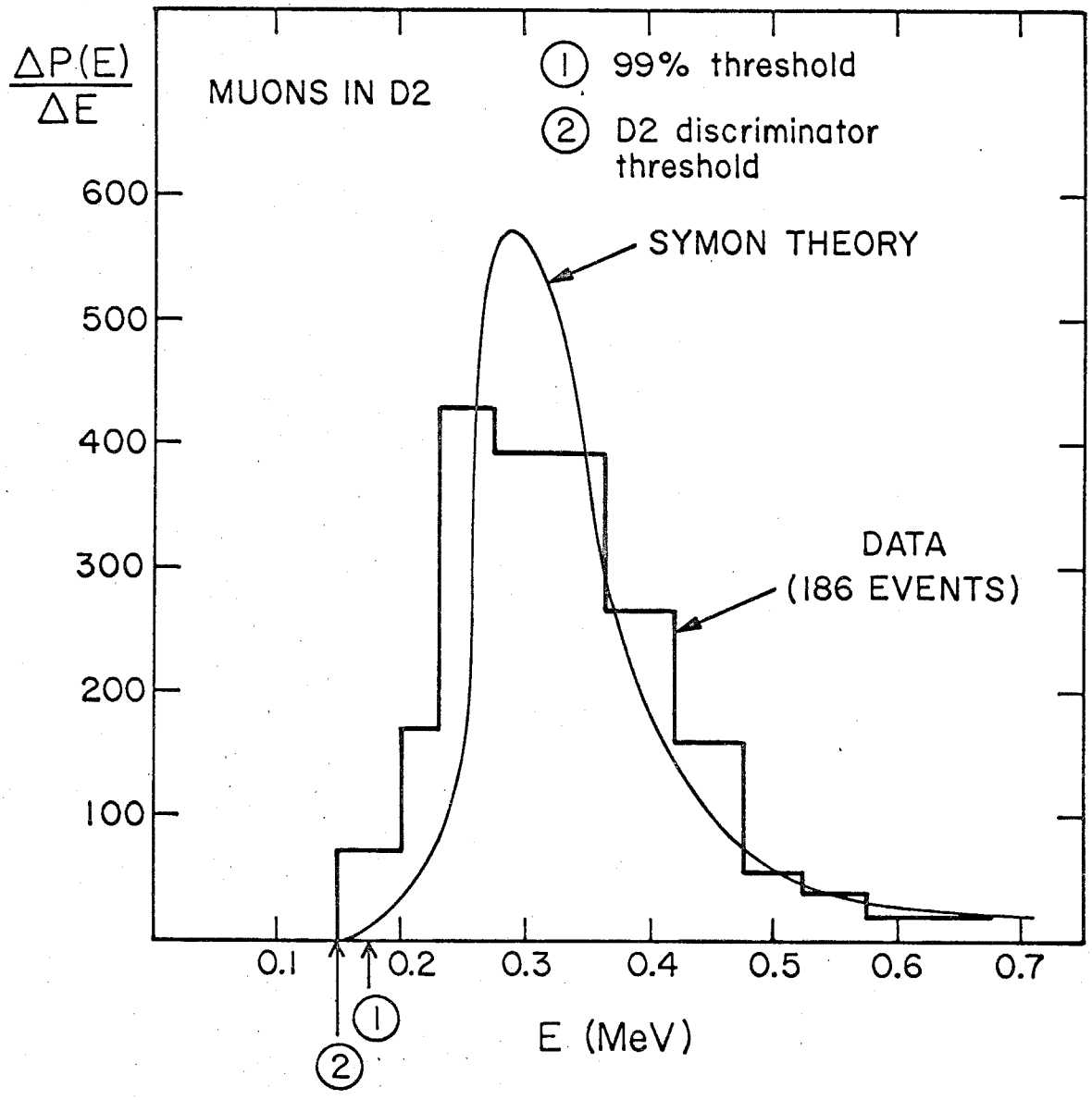
ΔP(E)/ΔE
MUONS IN D2
① 99% threshold
② D2 discriminator threshold
SYMON THEORY
DATA
(186 EVENTS)
600
500
400
300
200
100
0.1
0.2
0.3
0.4
0.5
0.6
0.7
E (MeV)
①
②

Figure II-3

Setup for muon calibration of the Range telescope anticoincidence detector. LMs are shaping amplifiers for the PM tube signals; COINC is a 3-fold fast coincidence circuit. The RIDL PHA is a 100 channel pulse height analyzer used for obtaining the muon spectrum in D8. CSA is a charge sensitive amplifier.

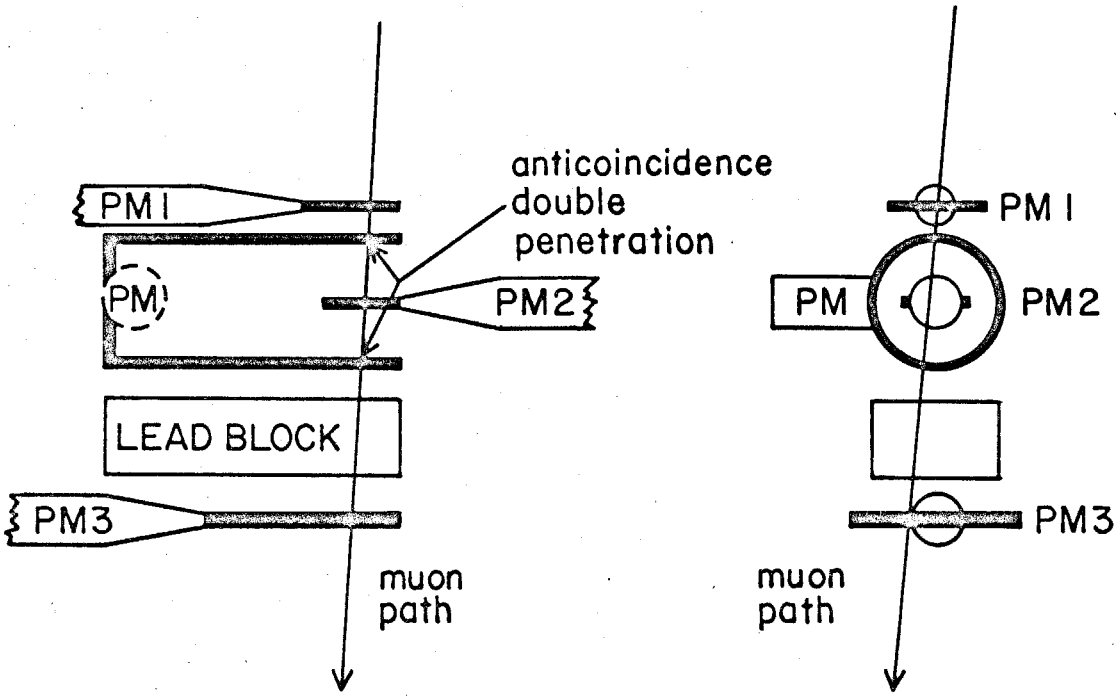
PM1
PM
PM2
anticoincidence
double
penetration
LEAD BLOCK
PM3
muon
path
PM 1
PM
PM2
PM3
muon
path

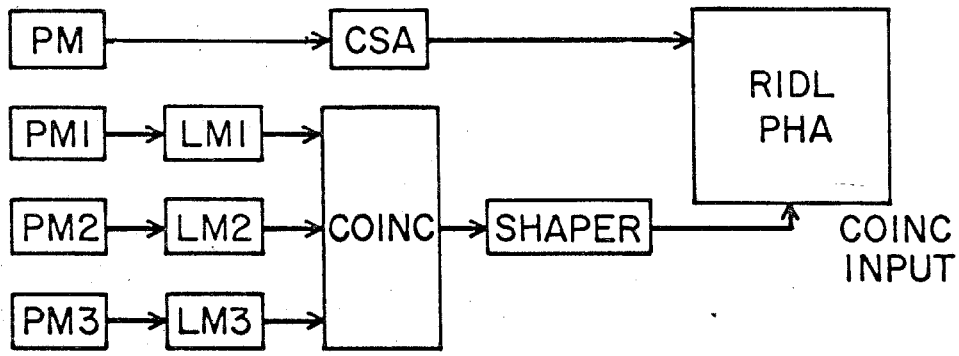
PM
CSA
RIDL
PHA
PM1
LM1
PM2
LM2
COINC
SHAPER
COINC
INPUT
PM3
LM3

events which twice penetrated the plastic scintillator at the end farthest from the tube. (This situation represents the worst case for light collection.) Using the pulse height spectrum from these data, the threshold of the D8 discriminator was set so that at least 99% of all minimum ionizing charged particles which pass once through the scintillator trigger D8. Figure II-4 illustrates a typical muon pulse height spectrum for doubly penetrating particles. The arrows show the 99% thresholds for doubly penetrating particles, singly penetrating particles, and the actual threshold of the D8 discriminator.

3) Electronics

The electronic configuration of this experiment is described in detail in a paper presented to the Fourteenth Nuclear Science Symposium of the IEEE in 1967 (13). The essential functions of the electronics package are:

a) Analog Processor

Each detector has associated with it a charge sensitive preamplifier followed by a shaping amplifier. These components [referred to collectively as charge sensitive amplifier (CSA)] amplify and shape the detector signals for analysis by the pulse height-to-time converter (HTC). The three independent pulse height analyzers (PHA) digitize the energy loss measurements made by the detectors.

Figure II-4

Muon spectrum in D8 for cosmic ray muons detected at ground level using the setup shown in figure II-3.

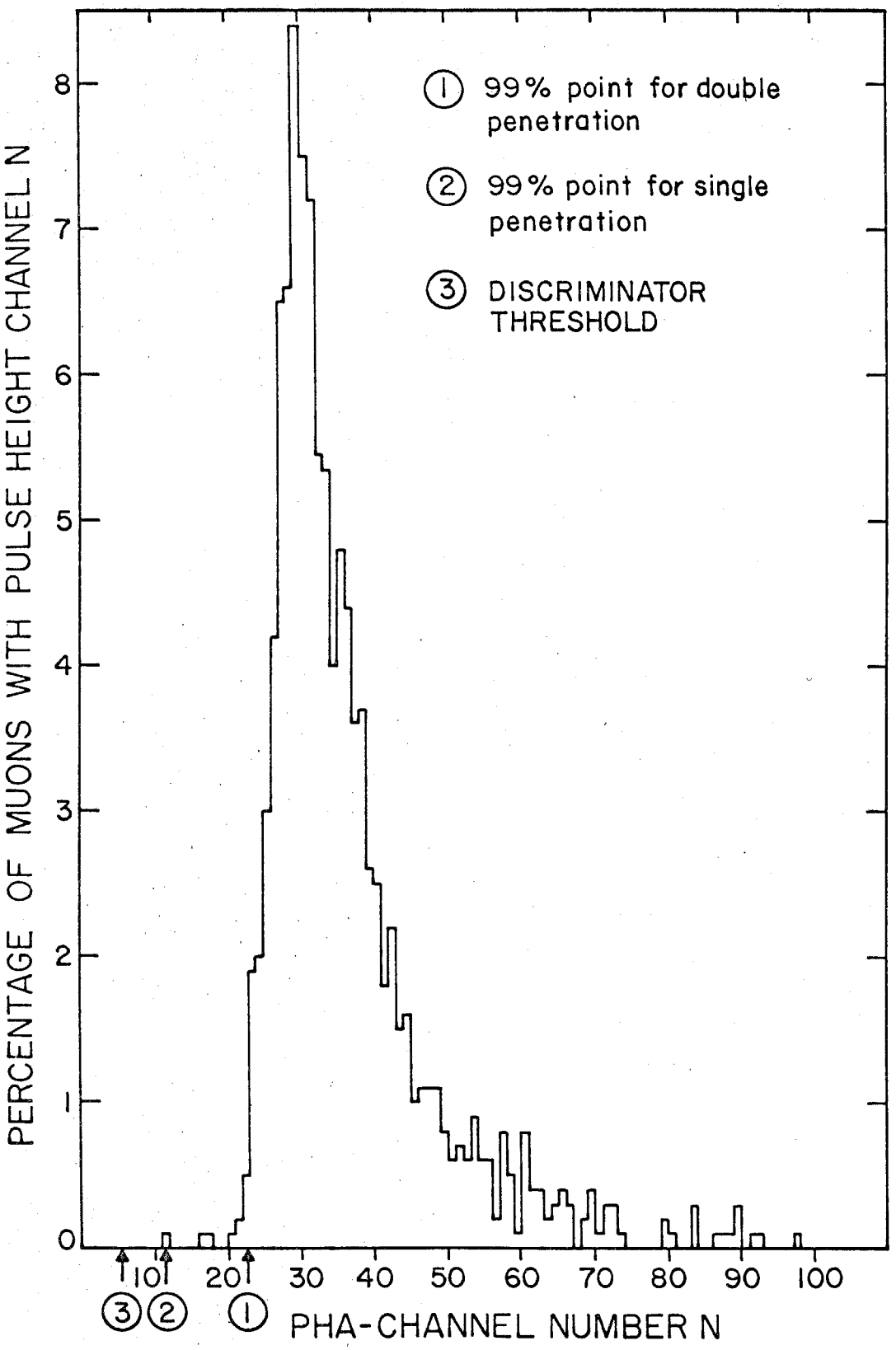
① 99% point for double penetration
② 99% point for single penetration
③ DISCRIMINATOR THRESHOLD
PERCENTAGE OF MUONS WITH PULSE HEIGHT CHANNEL N
0
1
2
3
4
5
6
7
8
10
20
30
40
50
60
70
80
90
100
③
②
①
PHA-CHANNEL NUMBER N

b) Coincidence and Priority Logic

This subsystem controls the use of the analog processor. It determines whether a new event has occurred, and if this event should be analyzed. The event definitions required by the coincidence logic may be modified through ground commands. Any of D1, D2 or D3 may be disabled and, if desired, the entire Range telescope may be turned off.

c) Rate Accumulator Subsystem

In addition to event analysis, the rates of several coincidences along with the singles rate of each detector in the experiment are monitored. To conserve telemetry bits, these rates are commutated so that only two rates are read out at a time. A more detailed description of the telemetry assignments for this experiment, and the interpretation of the data bits can be found in the references (14, 17).

III. SATELLITE

A) Spacecraft

The Orbiting Geophysical Observatory (OGO) satellite series is a program of the National Aeronautics and Space Administration which is designed to provide spacecraft which can support a large number of experiments with a large data capacity. OGO-VI is the last in the series of OGO satellites. It is a polar orbiter which was launched on 5 June 1969, into an orbit with perigee height of 397 km, apogee height of 1098 km, inclination of 82 degrees and period of 99.8 minutes (18).

The Caltech Solar and Galactic Cosmic Ray experiment is mounted on the -Z door of the spacecraft which is facing radially away from the earth.

B) Orbit

In figure III-1 several consecutive orbital trajectories (rev) are plotted. These are polar plots of the geocentric latitude vs. geocentric longitude of the satellite as it passes over the northern hemisphere. Also shown on this plot is the location of the geomagnetic north pole and a contour of constant invariant latitude (19, 20) of ~72°. The plane of the orbit of the satellite is approximately fixed in space so that the earth will be rotating as viewed

Figure III-1

Orbital trajectories for OGO-VI in the northern hemisphere. Plots are in geocentric coordinates with the magnetic north pole indicated by the "x". A contour of constant invariant latitude (or equivalently constant L value) is shown by the dashed line.

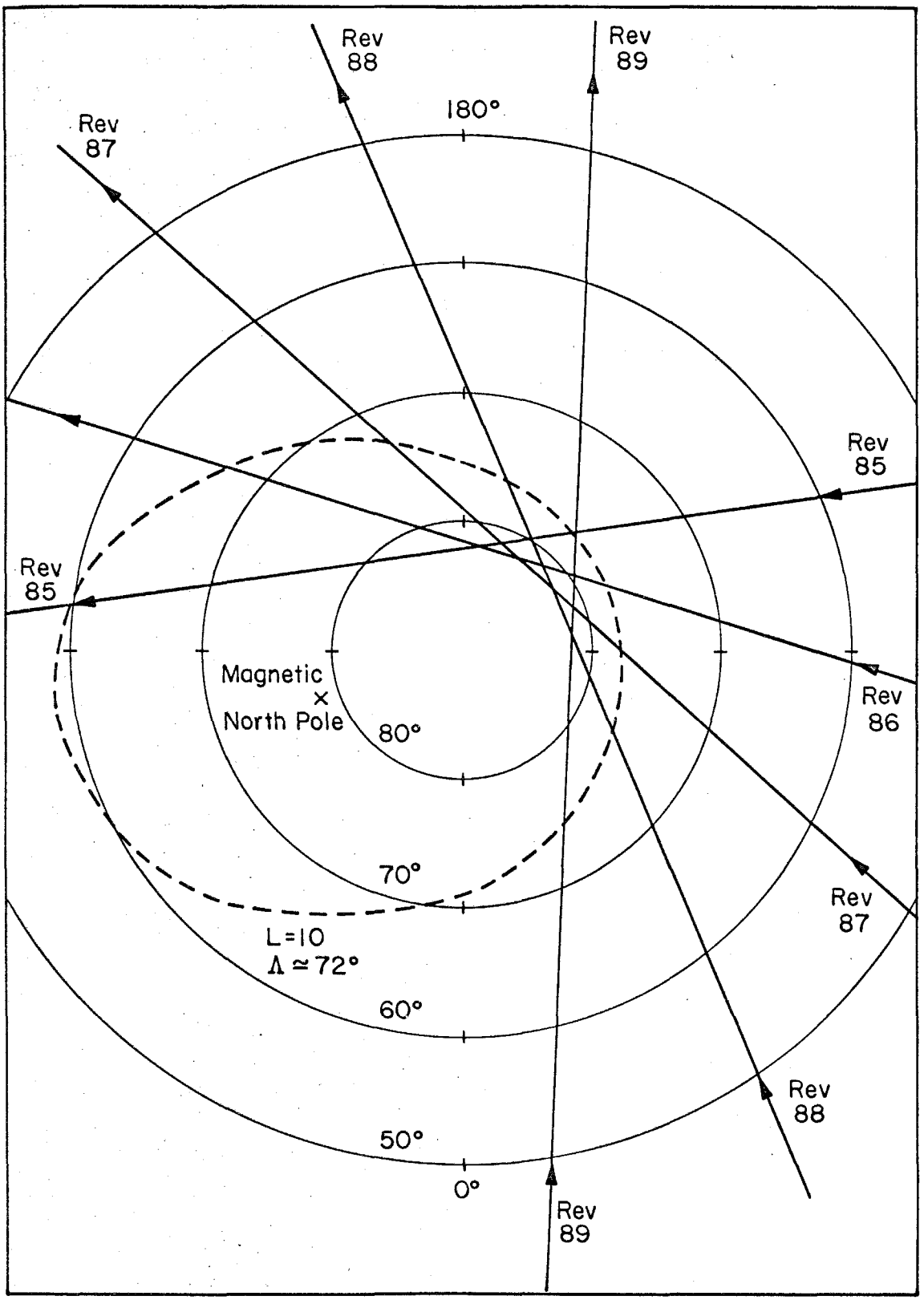
Rev 88
Rev 89
180°
Rev 87
Rev 85
Rev 85
Magnetic
×
North Pole
80°
Rev 86
70°
Rev 87
L=10
Λ ≃ 72°
60°
Rev 88
50°
0°
Rev 89

from the spacecraft. Thus, successive orbits bring the satellite over different longitudes of the earth. In fact the orbit drifts approximately 24° in longitude per revolution. Because of the rotation of the orbit relative to a fixed location on the earth, there will be orbits during which the satellite remains relatively far from the geomagnetic pole. In figure III-1 for example, on revolutions 87 and 88 the satellite just barely comes within the 72° invariant latitude contour. For orbits like these, there will be little useful low energy cosmic ray data since the geomagnetic field prevents these particles from reaching the satellite (21, 22, 23).

IV. DATA ANALYSIS

A) Calibrations

The experiment calibrations may be divided into two categories - electronic and particle. The electronic calibration results in a precise knowledge of the discriminator and HTC responses as a function of charge at the CSA input. In addition, the temperature dependence of these responses is determined as is the time variation. The detector calibration, particularly at low energies, gives the response of the solid state detectors and their resolution. We will describe the procedures below.

1) Electronic Calibration

The electronic calibrations were made using a Berkeley Nucleonics Co. (BNC) Tail Pulse Generator (model RP-2). The voltage step (50 nsec rise time) from this pulser was fed into a test capacitor which is connected to the input of the charge sensitive amplifier (CSA) being calibrated. Each CSA contains a test capacitor and test input connection. The pulser and test capacitor simulated the current pulse produced by a detector (solid state detector or photomultiplier tube). By varying the amplitude of the pulser output, the discriminators and PHAs associated with each detector were calibrated. Due to the random noise generated by the detector and electronics, the output of a pulse height analyzer is not

constant for a series of constant amplitude input signals. Upon plotting the frequency distribution of pulse heights measured (i.e., the number of times a pulse height is observed vs. the pulse height), we obtain a Gaussian distribution which is centered on the pulse height corresponding to the input if there was no noise, and with a standard deviation which depends on the rms value of the noise. Therefore, in order to find the correspondence between input signal amplitude and pulse height channel, the input signal which results in a Gaussian distribution of pulse heights centered on the channel of interest must be found. This is done by measuring the integral of the distribution rather than the distribution itself since, when 50% of the measured pulse heights are greater than or equal to a particular pulse height channel number, the Gaussian distribution will be centered on the threshold of that channel. Similarly, when either ~16% or ~84% of the measured pulse heights are greater than or equal to the channel being calibrated, the Gaussian distribution will be minus or plus one standard deviation from the channel threshold. Therefore, by varying the input signal amplitude until ~16%, 50% or ~84% of the measured pulse height channel numbers are greater than or equal to the channel number of interest, the threshold of that channel and the standard deviation of the Gaussian spreading due to noise are found. A similar technique is used for determining the threshold of each

discriminator. In actual practice, measurements are made for several input amplitudes and the results are plotted on integral Gaussian paper. From this graph the threshold and standard deviation are found. In figure IV-1 a typical integral Gaussian plot is shown for the D1 discriminator.

To convert the electronic calibration, which is in arbitrary units fixed by the pulser normalization, to energy units, a standard reproducible source of detectable pulses was used. This consisted of the output from a fully depleted gold-silicon surface barrier detector which was exposed to a Th B source of alpha particles. [Th B decays producing either a 8.776, 6.083 or 6.045 MeV alpha particle (24).] Using this standard signal source, the BNC pulser was normalized so that 8.00/20 PHU into a 10.0 pf capacitor = 8.776 MeV. (PHU = Pulse Height Unit. 10.0 PHU = full scale output of pulser. Pulser settings are expressed as dial setting/attenuation.) The standard source was also used to determine for each CSA the correspondence between PHU into the test input and energy lost in a detector as measured by that CSA. This was done by finding the value of the test input signal (in PHU) which results in the same amplifier output as the standard source input. The ratio of the test signal (PHU) to the energy of the standard source alpha particle used gives the conversion factor (CF) for that CSA. Using these calibration

Figure IV-1

D1 discriminator calibration for two temperatures. The percentage of pulses which trigger the discriminator is plotted vs. the input pulse height in PHU. (See text.)

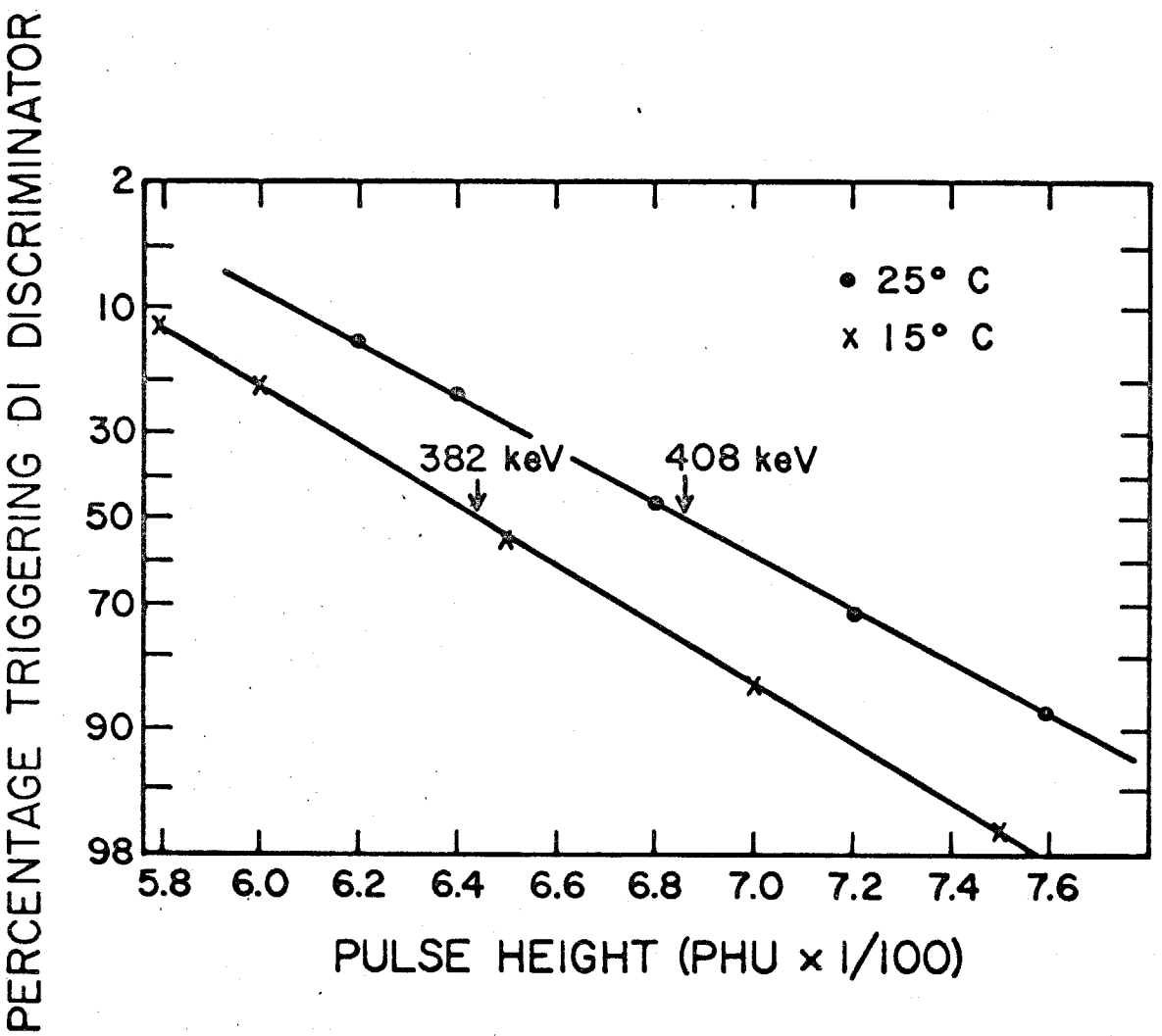
PERCENTAGE TRIGGERING DI DISCRIMINATOR
2
10
30
50
70
90
98
5.8
6.0
6.2
6.4
6.6
6.8
7.0
7.2
7.4
7.6
PULSE HEIGHT (PHU x 1/100)
• 25° C
x 15° C
382 keV
408 keV

methods, the normalization of the pulser and the conversion factors for the amplifiers were determined to at least 1%. Table IV-I lists the conversion factors and calibration results for the Range telescope detector amplifiers discussed in this thesis. In addition, calibration curves for the pulse height analyzers for D1, D2 and D3 are shown in figures IV-2 through IV-4. Typical channel widths are ~50 keV. The standard deviations of the Gaussian spreading due to detector and electronic noise are ~20 keV. Calibrations were made at various temperatures of the unit and over a period of one year. In flight the temperature of the experiment was generally between 15°C and 25°C, and the calibration uncertainties listed in the table IV-I refer to these extremes. There was no noticeable long term drift of the pulser normalization or the conversion factors, nor was there any noticeable drift of the PHA and discriminator calibrations.

2) Particle Calibration

The response of the detectors used in this experiment to low energy protons was experimentally determined with the Caltech Tandem Van de Graaff accelerator. The assembled Range telescope with the flight electronics was used for these calibrations. From the data obtained, the D1, D2 and D3 depletion depths were accurately determined. Using the Th B source mentioned in section IV A1 above, the thickness

TABLE IV-I

CONVERSION FACTORS - RANGE TELESCOPE

Detector	CF PHU/MeV	PHA		
		Channel 1 Threshold (keV)	Saturation Threshold (MeV)	Disc. Threshold (keV)
D1	8.42×10^{-2}	153±2	14.1±.2	402±16
D2	8.63	195±4	13.7±.1	147±4
D3	8.76	183±5	13.5±.1	153±3

Figure IV-2

Dl-PHA calibration at 25°C. The threshold energy vs. channel number is plotted.

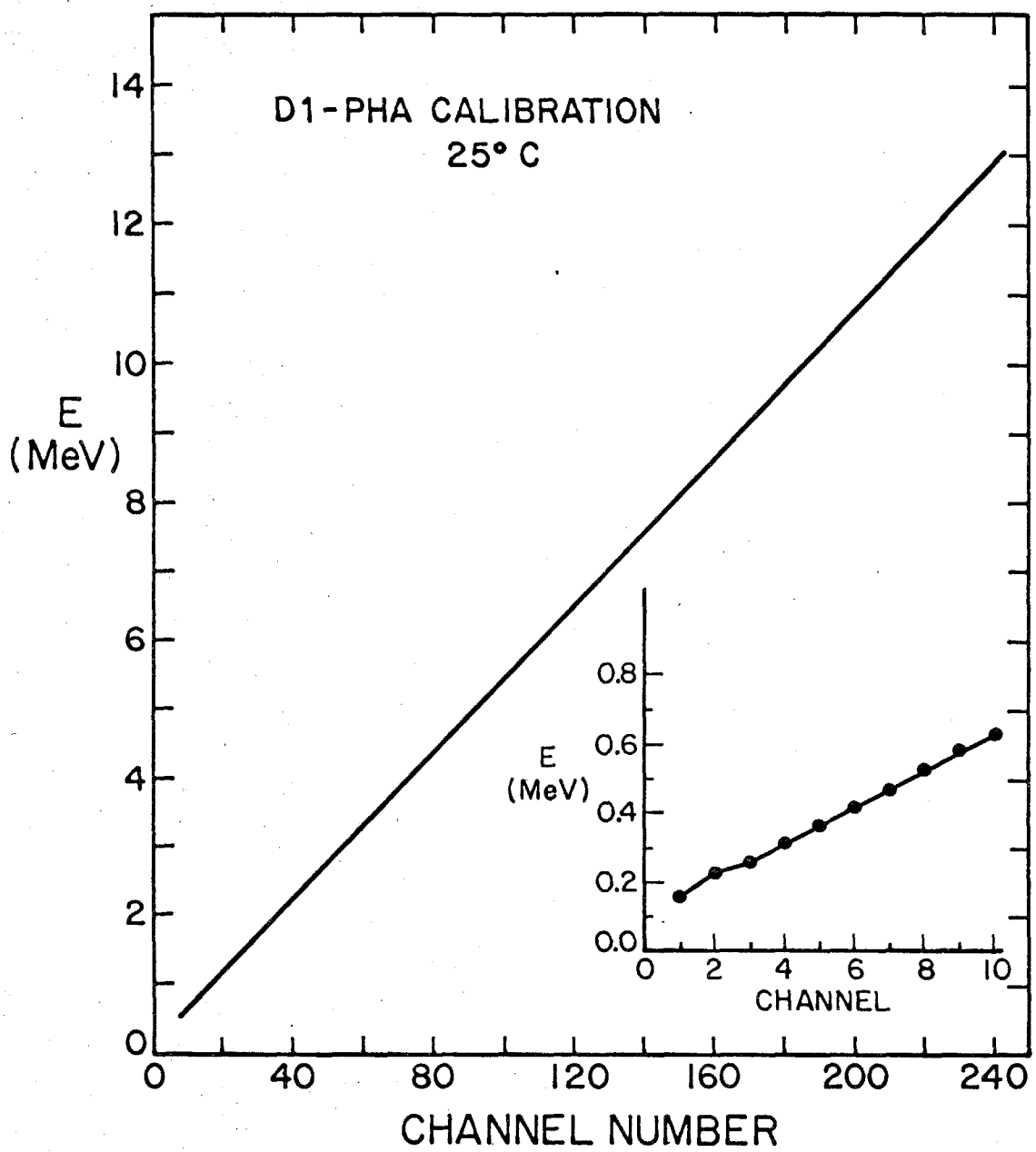
D1-PHA CALIBRATION
25° C
E
(MeV)
0
2
4
6
8
10
12
14
0
40
80
120
160
200
240
CHANNEL NUMBER
E
(MeV)
0.0
0.2
0.4
0.6
0.8
0
2
4
6
8
10
CHANNEL

Figure IV-3

D2-PHA calibration at 25°C. The threshold energy vs. channel number is plotted.

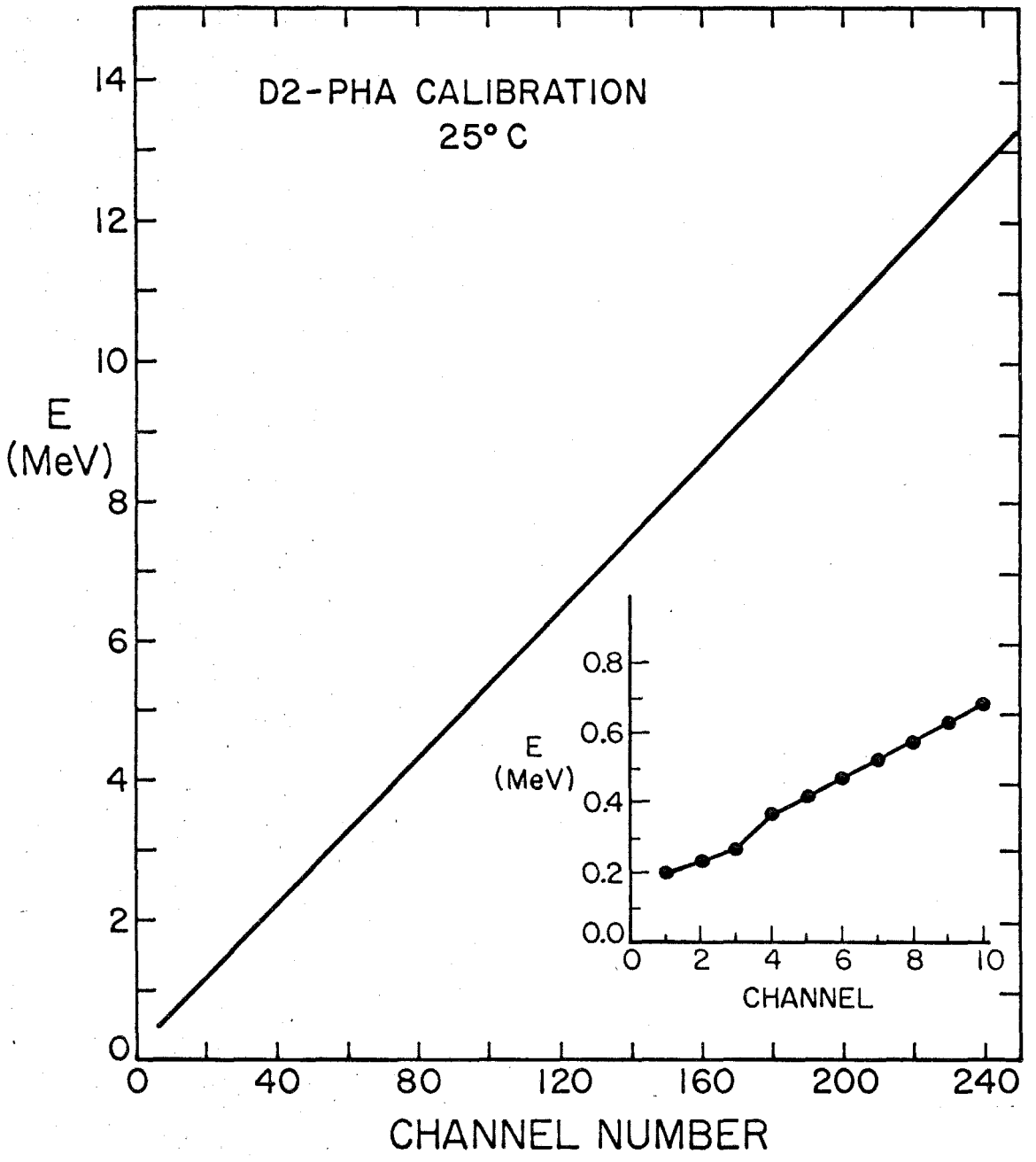
D2-PHA CALIBRATION
25° C
E
(MeV)
0
2
4
6
8
10
12
14
0
40
80
120
160
200
240
CHANNEL NUMBER
E
(MeV)
0.0
0.2
0.4
0.6
0.8
0
2
4
6
8
10
CHANNEL

Figure IV-4

D3-PHA calibration at 25°C. The threshold energy vs. channel number is plotted.

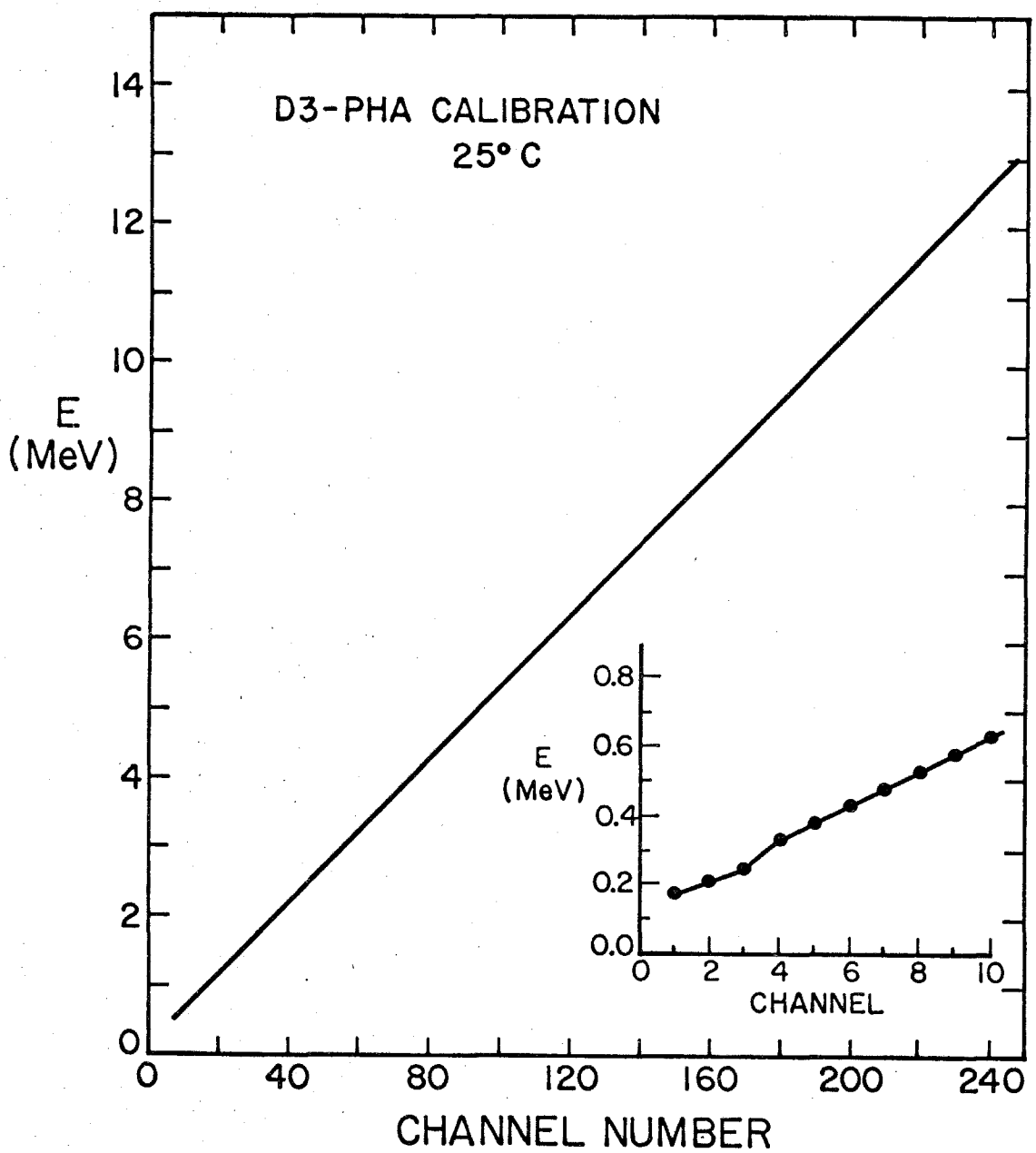
D3-PHA CALIBRATION
25° C
E
(MeV)
0
2
4
6
8
10
12
14
0
40
80
120
160
200
240
CHANNEL NUMBER
E
(MeV)
0.0
0.2
0.4
0.6
0.8
0
2
4
6
8
10
CHANNEL

of the aluminized mylar light shield was also measured. The details of this calibration are contained in Appendix A, and the results are summarized in table II-I. The estimated uncertainty in the detector thicknesses is ~3% which is mainly due to the expected uncertainty of the absolute accuracy of the range-energy tables (25) used in the thickness calculation. The measurement errors for this calibration are ~1% and therefore do not contribute significantly to the total error. For all of the analysis of data discussed in this thesis, the detector thicknesses are used in conjunction with the range-energy tables to interpolate between calibration points. Thus any systematic errors in the detector thicknesses due to errors in the range-energy tables will not be relevant and only the actual measurement errors, which are small, contribute to the uncertainties in the reduced data.

B) Response

Using the results of the calibration described in section IV A, the response of the detector system for 1-15 MeV protons can be predicted. Figure IV-5 shows the average energy loss in D1 and D2 vs. kinetic energy for both protons and alpha particles. These plots are based on interpolation of data from the range-energy tables mentioned in section IV A. The tables are the result of integrating semi-empirical energy loss functions. The particular form for

Figure IV-5

Average energy loss in D1 and D2 vs. incident kinetic energy for protons and alpha particles.

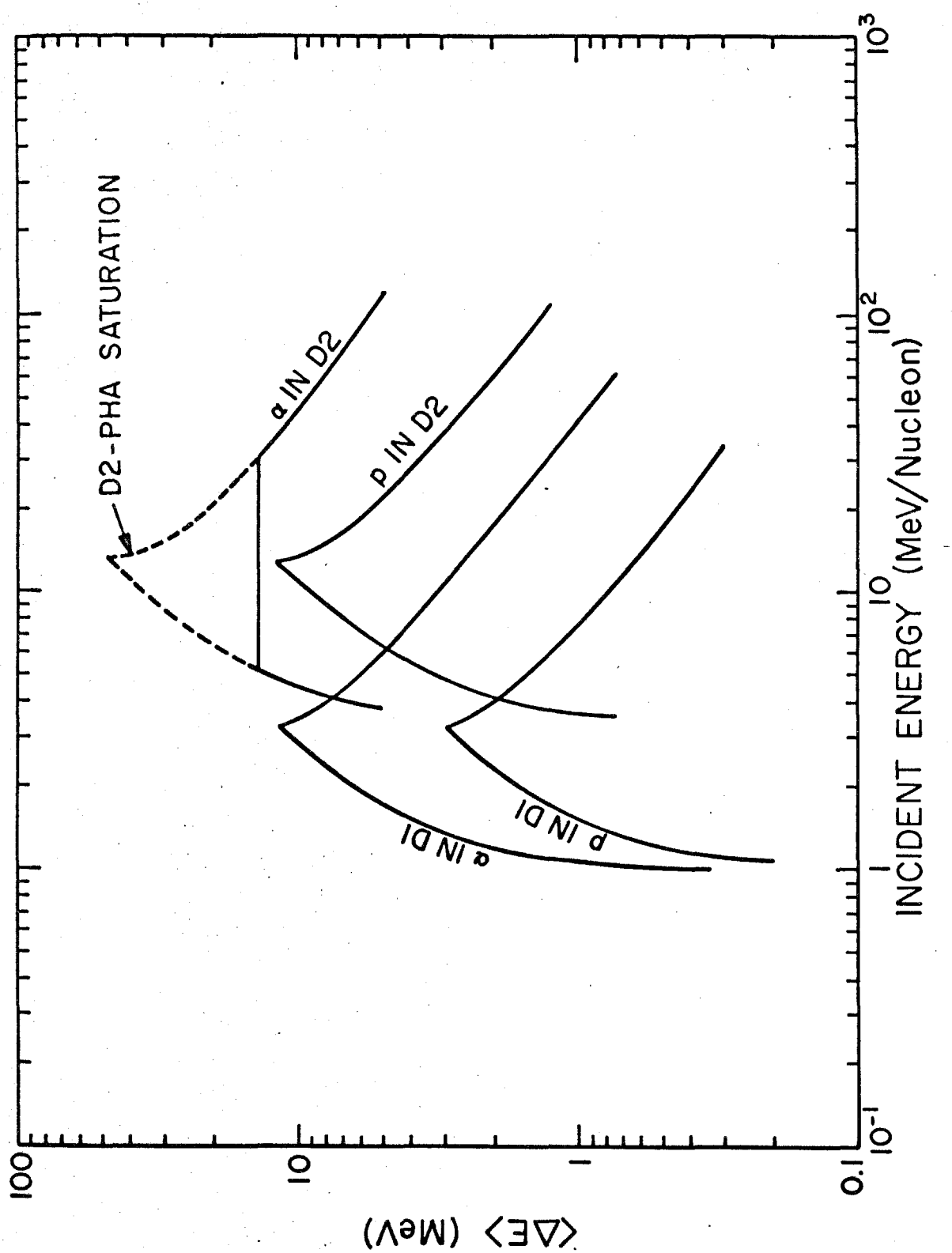
D2-PHA SATURATION
α IN D2
p IN D2
α IN D1
p IN D1
100
10
1
0.1
⟨ΔE⟩ (MeV)
10⁻¹
1
10
10²
10³
INCIDENT ENERGY (MeV/Nucleon)

this function used by Janni (25) is

$$\frac{1}{\rho}\frac{dE}{dx} = -\frac{4\pi N_0 z^2 e^4}{mc^2\beta^2}\frac{Z}{A}\left\{\log\left(\frac{2mc^2\beta^2}{I_{adj}(1-\beta^2)\sqrt{1+\frac{2M}{M\sqrt{1-\beta^2}}+\left(\frac{m}{M}\right)^2}}\right) - \beta^2 - \frac{\sum_i C_i}{Z} - \frac{\Delta}{2}\right\} \qquad (4\text{-}1)$$

where

ρ = density of material

z = effective charge of particle

c = velocity of light

e = electron charge

m = rest mass of electron

A = atomic weight of stopping material

N_0 = Avogadro's Number

Z = atomic number of stopping material

I_{adj} = adjusted ionization potential

β = particle velocity in units of c

$\sum_i C_i$ = sum of effects of shell correction on stopping power

Δ = polarization effect correction term

From the data plotted in figure IV-5, we can find the expected energy loss in both D1 and D2 as a function of kinetic energy. Plots of the average energy loss in D1 vs. the average energy

loss in D2 for increasing kinetic energy are shown in figure IV-6 for protons and alpha particles. The arrows on the curves indicate the direction of increasing kinetic energy of the incident particle. Also included on the proton plot are several measured points from the accelerator calibration. Using the data from this calibration, a band can be constructed on the D1 vs. D2 pulse height plot in which essentially all protons should lie. The band is constructed by using the accelerator calibration data to determine the distribution of protons along a line of constant total energy loss on the D1-D2 plot. In figure IV-7 we show an expanded view of the measured D1 vs. D2 pulse height distribution for 4.00 MeV protons incident on the Range telescope. Since the D1 and D2 pulse height analyzer channel widths are approximately equal (~50 keV), lines of constant total energy loss are simply slope -1 lines on this linear plot. As expected, the D1-D2 channel pair with the largest number of events is that which corresponds to the average energy loss in D1 and D2 for a 4.00 MeV proton. Furthermore, as can be seen from the figure, the protons are strongly clustered about the slope -1 line which passes through this most probable channel pair. Taking a width along this line of 13 D1 channels*, we form one segment of the band which will

*The width of the band is made larger than that indicated by the accelerator calibration to insure that all protons are included. In the energy range of interest (1-15 MeV) this does not introduce any contamination since the separation on the D1-D2 plot of protons and alpha particles is quite large.

Figure IV-6

Average energy loss in D1 vs. average energy loss in D2 is plotted for protons and alpha particles. Arrows indicate the direction of increasing kinetic energy of the incident particle. For protons several measured points from an accelerator calibration are also plotted.

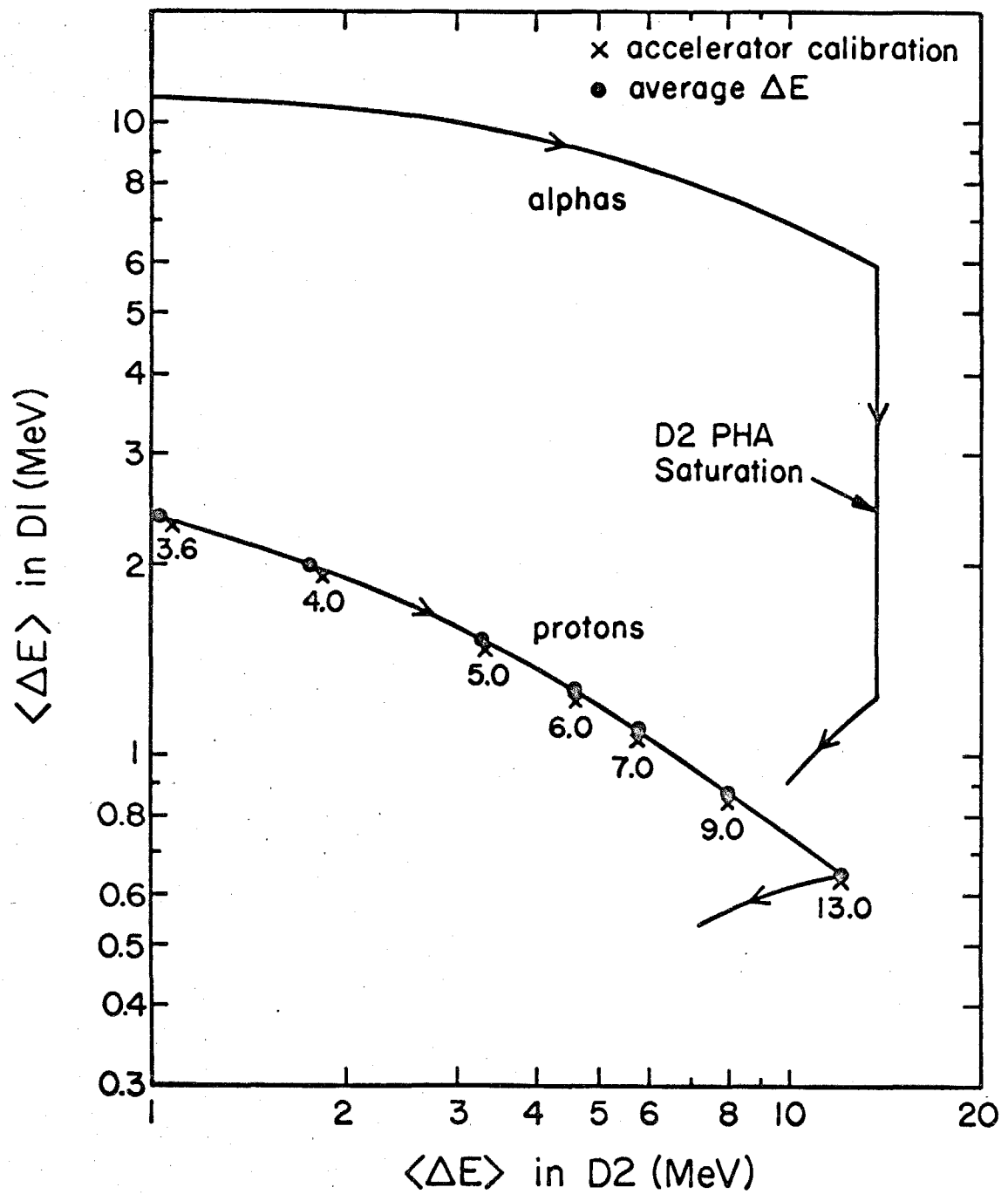
× accelerator calibration
● average ΔE
alphas
D2 PHA
Saturation
protons
3.6
4.0
5.0
6.0
7.0
9.0
13.0
10
8
6
5
4
3
2
1
0.8
0.6
0.5
0.4
0.3
1
2
3
4
5
6
8
10
20
⟨ΔE⟩ in D1 (MeV)
⟨ΔE⟩ in D2 (MeV)

Figure IV-7

Accelerator calibration data for 4.00 MeV protons incident on the Range telescope. The number of protons with a given D1 and D2 pulse height pair is listed in the figure at the appropriate location in the D1-D2 pulse height matrix.

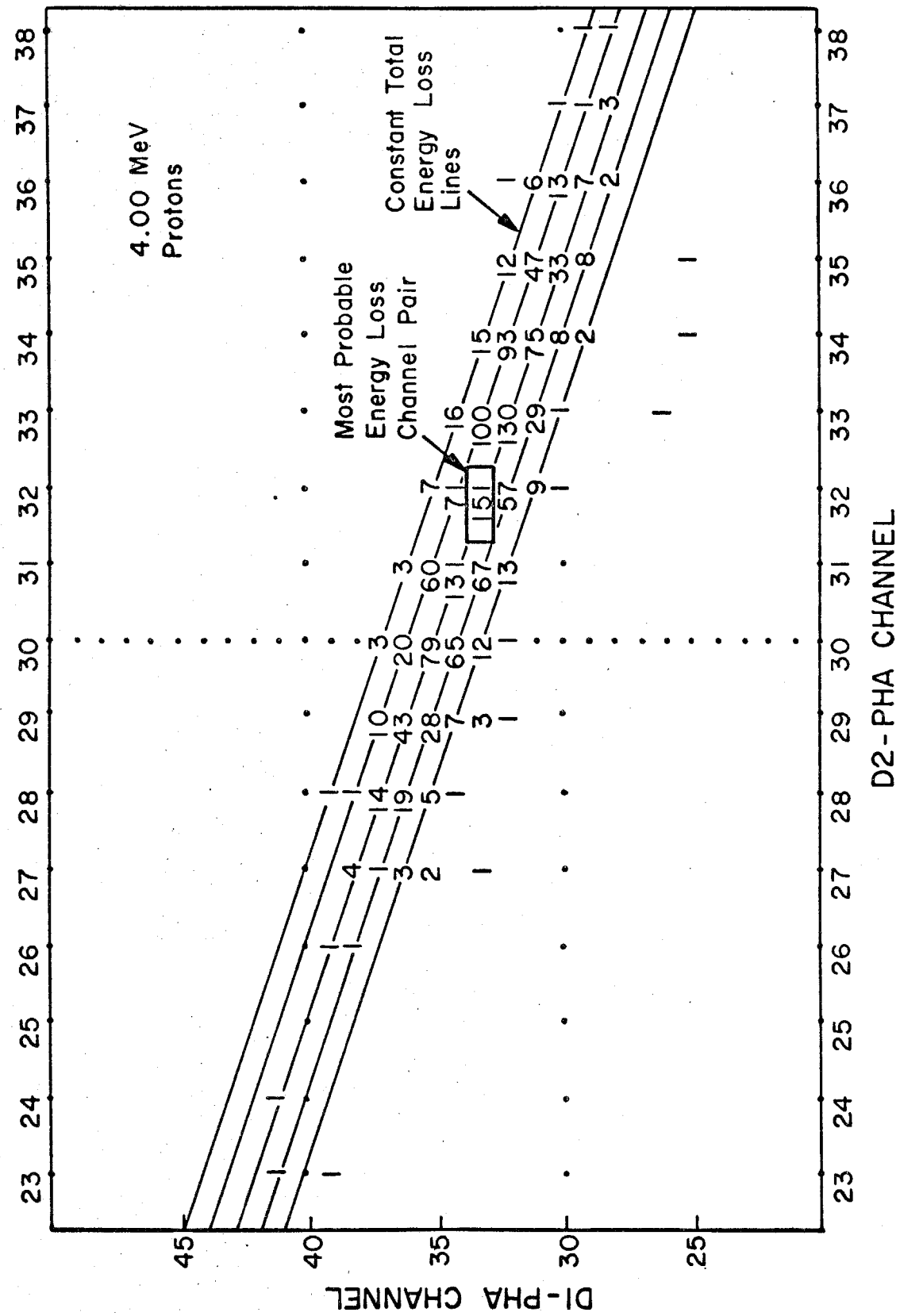
4.00 MeV
Protons
Most Probable
Energy Loss
Channel Pair
Constant Total
Energy Loss
Lines
D1-PHA CHANNEL
D2-PHA CHANNEL

include essentially all of the protons which are incident on the telescope. Similarly, the band width can be found at each of the calibration energies and a smooth band is then constructed in which all protons of energies 1-15 MeV will lie. In figure IV-8 this band as well as the average energy loss trajectory is shown. In addition, the average energy loss trajectory for alpha particles is shown. Except for those alpha particles which stop in D1 with total energy less than ~3.3 MeV, there is a clean separation of protons and alpha particles. It is possible to correct the low energy proton data for any alpha particle contamination by extrapolating the alpha particle spectrum available from data at higher energies to energies below 3.3 MeV, and subtracting this from the observed data. For the 7 June 1969 flare which we will be discussing, such corrections were found not to be necessary.

The proton band as described above is a region on a D1 vs. D2 pulse height plot in which protons of energies from 1-15 MeV lie. By segmenting this band in an appropriate manner, the energy spectrum of these protons can be determined. For protons stopping in D1 we simply add the contents of 3 pulse height channels together to form a single energy bin. In this manner protons with incident energies from 1.174-2.993 MeV are resolved in 14 separate bins. For

Figure IV-8

Energy loss in D1 vs. energy loss in D2. The proton band and trajectory on a D1-D2 plot is shown for protons from ~3.6 to 15 MeV. Also plotted is the alpha particle trajectory from ~10 to 180 MeV.

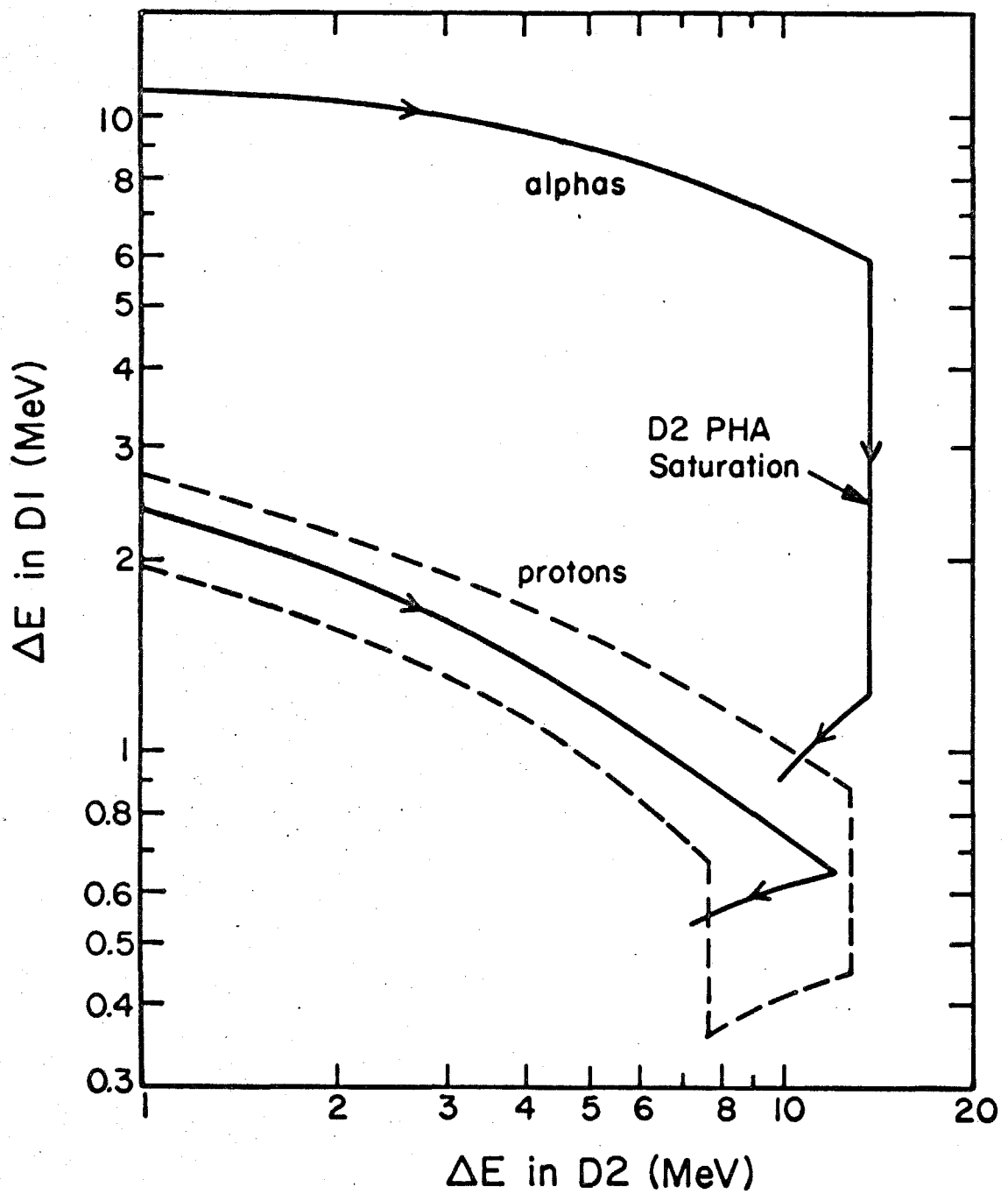
alphas
D2 PHA
Saturation
protons
ΔE in D1 (MeV)
ΔE in D2 (MeV)
10
8
6
5
4
3
2
1
0.8
0.6
0.5
0.4
0.3
1
2
3
4
5
6
8
10
20

protons which penetrate D1, the bins are created by making cuts along lines of constant total energy loss in D1 + D2. The energy limits assigned to these bins are the energies which correspond to the energy loss along the cut lines. The energy limits of the 24 bins used in processing the data are listed in table IV-II.

A typical D1-D2 data plot for the 7 June 1969 flare observed is shown in figure IV-9. The proton band is indicated by the contour. Clearly there are very few events outside of the contour. It is possible that most of these anomalous events are due to the effects of channeling in D1 (26). However, since the number of these event is small, they are ignored in the data analysis. Also shown is the trajectory for alpha particles. As is apparent, there are only a small number of these present.

C) Data Processing

Figure IV-10 illustrates the general data processing scheme used for the OGO-VI data. The raw data received at Caltech consists of two types of magnetic data tapes - experimenter data tapes and attitude-orbit tapes. The experimenter data tapes contain decommutated experiment raw data as received from the spacecraft (14). The attitude-orbit tapes contain the position and orientation of the spacecraft

TABLE IV-II

BIN ENERGIES

Bin Num.	Lower Limit	Upper Limit
1	1.174 MeV	1.268 MeV
2	1.268	1.373
3	1.373	1.485
4	1.485	1.607
5	1.607	1.733
6	1.733	1.865
7	1.865	2.001
8	2.001	2.141
9	2.141	2,280
10	2.280	2.419
11	2.419	2.560
12	2.560	2.703
13	2.703	2.847
14	2,847	2.993
15	2.993	3.141
16	3.141	3.300
17	3.30	3.60
18	3.60	4.00
19	4.00	4.50
20	4.50	5.00
21	5.00	6.00
22	6.00	7.00
23	7.00	9.00
24	9.00	15.00

Figure IV-9

Observed D1 vs. D2 pulse height distribution for a typical polar pass during the decay of the 7 June 1969 solar flare event. The number of particles* with a given D1 and D2 pulse height pair is listed in the figure at the appropriate location in the D1-D2 pulse height matrix. The D1 and D2 pulse height scales are pseudo logarithmic*. Therefore, the scale labels do not refer directly to pulse height channels for the D1 or D2 PHA. The proton band from figure IV-8 is outlined and the alpha particle trajectory is also shown.

*See Appendix D for correspondence between plotted symbol and number of events. Also listed is the correspondence between the plotted channels and the actual pulse height analyzer channels.

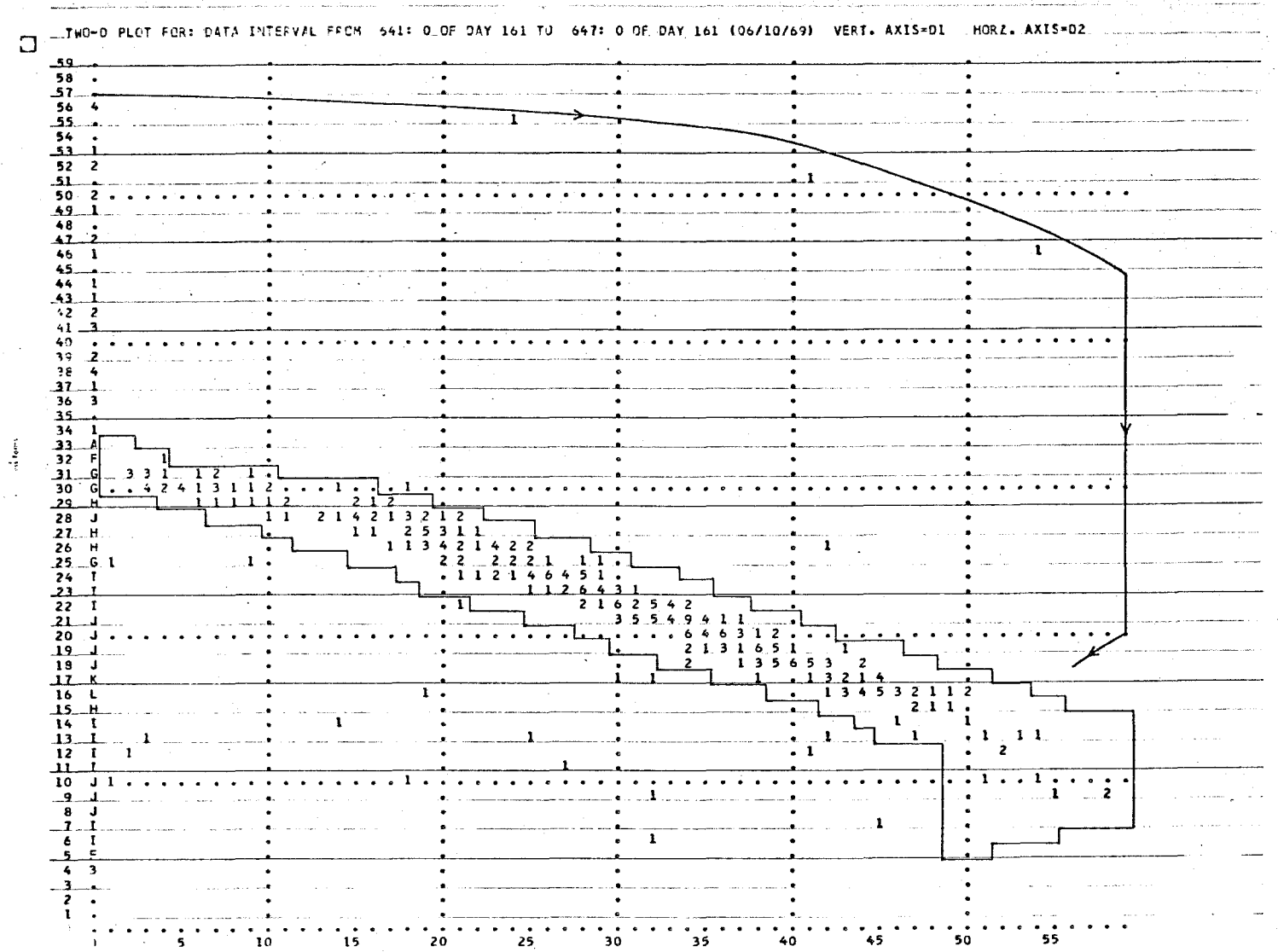
TWO-D PLOT FOR: DATA INTERVAL FROM 541: 0 OF DAY 161 TO 647: 0 OF DAY 161 (06/10/69) VERT. AXIS=01 HORZ. AXIS=02
1
5
10
15
20
25
30
35
40
45
50
55

Figure IV-10

Three-step data processing plan for the experiment. "Exp't" tape is the experimenter data tape received from Goddard Space Flight Center (GSFC) which contains decommutated raw experiment data. "A-0" tape is the altitude orbit data tape also received from GSFC, which contains spacecraft position data. "Abs't" tape is the abstract and merge tape which contains all pertinent data from the experiment and spacecraft in a condensed format for use in the data analysis.

(1)

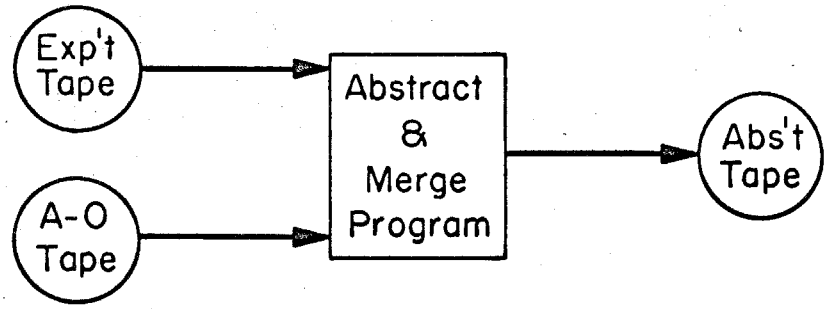
Exp't Tape
A-O Tape
Abstract & Merge Program
Abs't Tape

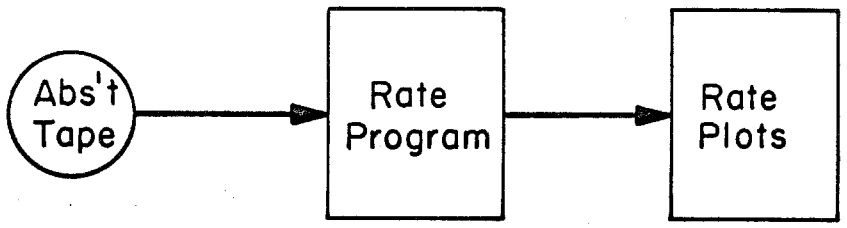
Abs't Tape
Rate Program
Rate Plots

(2)

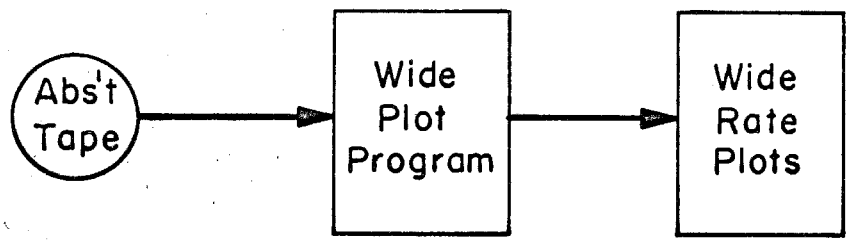
Abs't Tape
Wide Plot Program
Wide Rate Plots

(3)

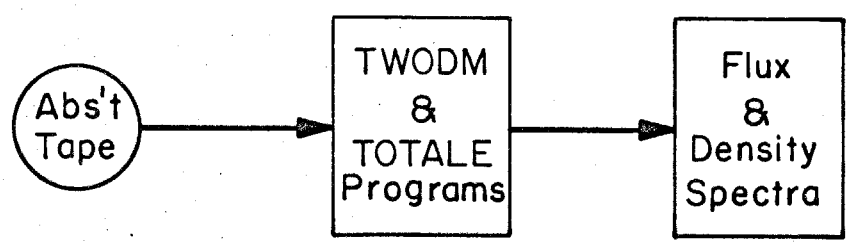
Abs't Tape
TWODM & TOTALE Programs
Flux & Density Spectra

as a function of time (one point per minute) as calculated from observations made by tracking stations (27). These tapes are abstracted and merged to produce time ordered tapes which contain all of the pertinent information from the experiment and spacecraft. In the next step of the data analysis, we further condense the data and produce what are called 'rate plots'. These are plots of various rates vs. time for each orbit of data.

This graphical output enables one to examine the data in an overall sense and thereby begin making evaluations as to performance and interest. From the rate plots, times of interest can be determined and used as input to other programs which further analyze the selected data. Examples of the rate plots as well as a more complete description of them can be found in Appendix B.

In the study of solar flares, it has been found useful to replot some of the data on a high resolution plot called 'wide' plots. Figure IV-11 shows an example of such a plot. In these 'wide' plots, the variations in rates over polar regions can be seen. (See Appendix B.) These variations are due to structure in the earth's magnetic field which limits or allows access by low energy particles to the polar regions (21, 22, 23). As can be seen from the sample plot,

Figure IV-11

Typical "wide" plot for an orbit of data during the 7 June 1969 solar flare event. The data plotted are several of the rates monitored by the experiment. AD8 is the Range telescope anticoincidence rate. D18 is the $D1\overline{D8}$ rate; D128 is the $D1D2\overline{D8}$ rate; D28 is the $D2\overline{D8}$ rate, and D238 is the $D2D3\overline{D8}$ rate. For further discussion see appendix B.

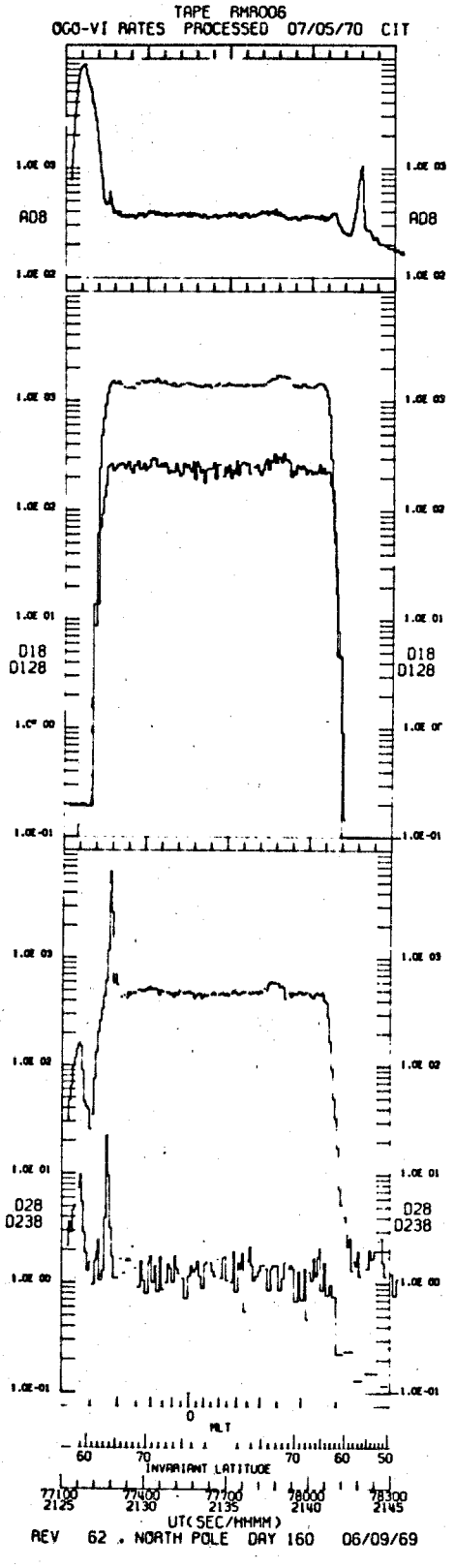
TAPE RMR006
OGO-VI RATES PROCESSED 07/05/70 CIT
AD8
D18
D128
D28
D238
0
MLT
60 70 INVARIANT LATITUDE 70 60 50
77100 77400 77700 78000 78300
2125 2130 2135 2140 2145
UT(SEC/HHMM)
REV 62 . NORTH POLE DAY 160 06/09/69

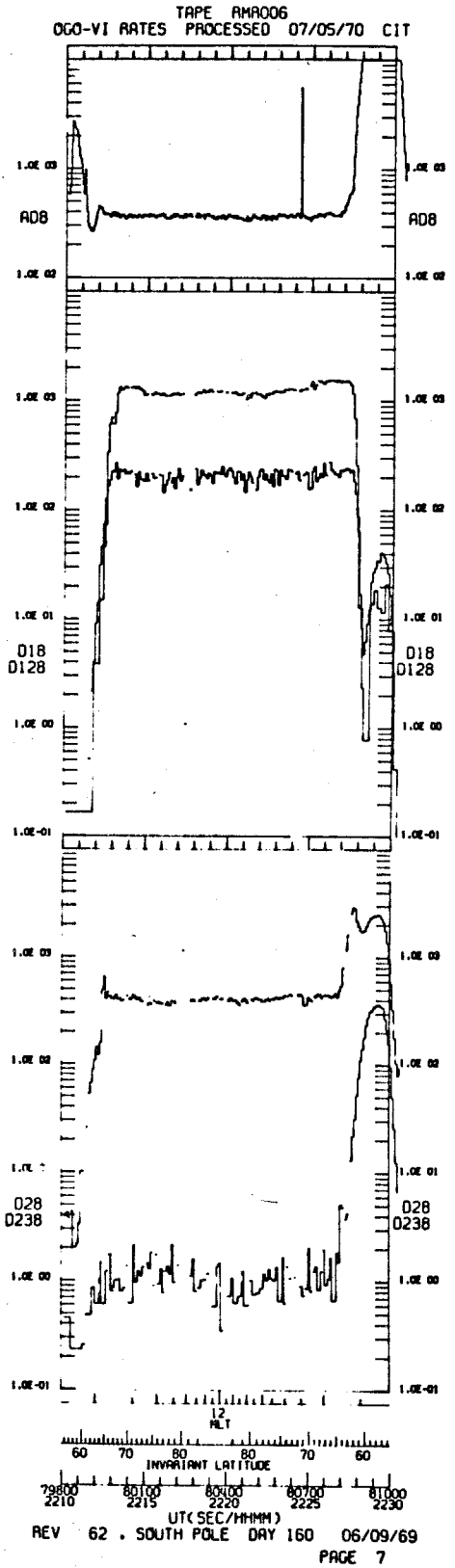
TAPE RMR006
OGO-VI RATES PROCESSED 07/05/70 CIT
AD8
D18
D128
D28
D238
12
MLT
60 70 80 INVARIANT LATITUDE 80 70 60
79800 80100 80400 80700 81000
2210 2215 2220 2225 2230
UT(SEC/HHMM)
REV 62 . SOUTH POLE DAY 160 06/09/69

there are several regions of interest. For low energy protons, the geomagnetic field limits the access of these particles to high magnetic latitudes ($\gtrsim 65°$ invariant latitude), above which there is approximately equal access, for this event, by all particles. As is clearly evident in the plot shown, there is considerable fluctuation of the various rates even in the high latitude regions. In analyzing the data from the 7 June 1969 flare, we have chosen regions of maximum flux in each pole as representative of the near earth flux.

Using the 'wide' plots to select these regions of maximum flux, the next step in the data analysis is the construction of differential flux spectra for protons from 1-15 MeV. As discussed in section IV B, this is done by counting the number of protons in each of the 24 energy bins of the proton band on a D1 vs. D2 pulse height plot. The absolute flux of protons is computed according to

$$F_{abs} = \text{number of protons}/(\text{time} \times A\Omega \times \Delta E) \qquad (4\text{-}2)$$

where $A\Omega$ is the geometrical factor and ΔE is the energy interval. The results of this step in the data processing are the reduced data for the event being studied. Examples of these data are shown in figures V-1 and -2. In figure V-1 the flux of protons at several energies is plotted as a function of time. In figure V-2 the adjusted differential

density is plotted as a function of kinetic energy for several orbits. These plots will be discussed in more detail in chapter V.

V. OBSERVATIONS

Utilizing the data processing plan outlined in section IV, data from a solar flare which occurred on 7 June 1969 were analyzed. A flare which was located at about 45°E solar longitude and 15°S solar latitude in McMath plage region 10135 (28) is taken as the probable source of the particles observed. There was type IV radio emission in the decimeter band and enhanced X-ray emission observed at 0415 GMT, and optical flares of importance 1N and -N were observed at 0630 and 0730, respectively. This type of activity frequently accompanies the injection of energetic particles into interplanetary space (29). Data coverage for this event is essentially complete from 1200 on 7 June through 1200 on 13 June. We will be interested mainly in the observations made during the decay phase of this event, that is, the time during which the flux of protons is smoothly decreasing with time. For this event we will study the decay phase during the 3 day interval from 0000 on 10 June through 0000 on 13 June. During this interval there were 72 polar passes which yielded usable data out of a possible 90 passes. (See section III B.) Typical results from the analysis of the data available are shown in figure V-1. These differential flux plots [log (flux) vs. time] illustrate some of the typical characteristics of solar flare

Figure V-1

Flux of protons vs. universal time for the 7 June 1969 solar flare event. (7 June 1969 is day 158.) The dashed lines are exponential fits to the decays of these fluxes.

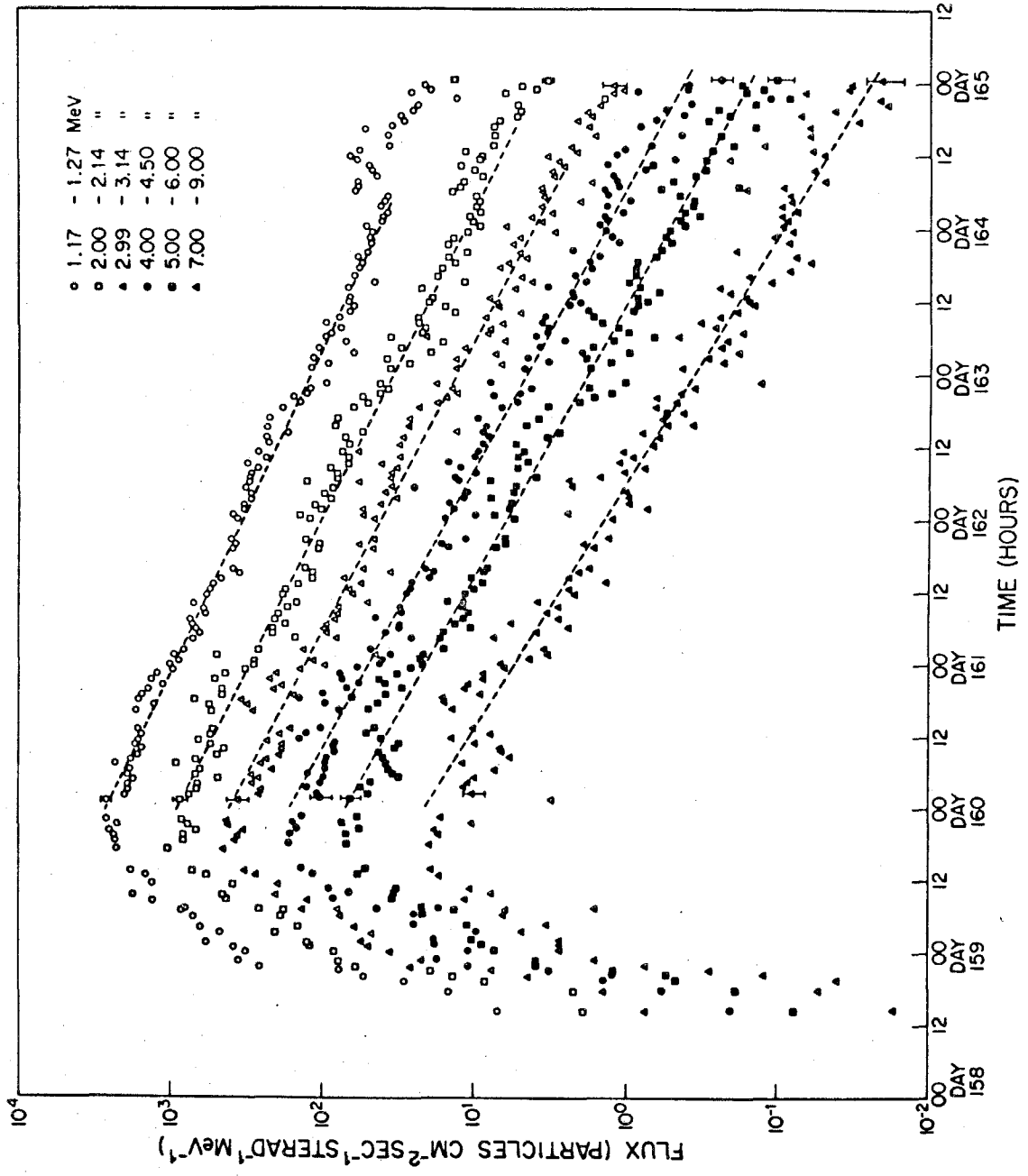
1.17 - 1.27 MeV
2.00 - 2.14 "
2.99 - 3.14 "
4.00 - 4.50 "
5.00 - 6.00 "
7.00 - 9.00 "
FLUX (PARTICLES CM⁻²SEC⁻¹STERAD⁻¹MeV⁻¹)
TIME (HOURS)
DAY 158
DAY 159
DAY 160
DAY 161
DAY 162
DAY 163
DAY 164
DAY 165

proton observations (30, 31). There is a relatively rapid rise compared to the decay, and a smooth turnover after the maximum flux is observed. The region during which the decay in flux is smooth is approximately exponential. The straight lines plotted in the figure are exponential functions of the form

$$F(T,t) = F_0(T)e^{-t/\tau} \qquad (5\text{-}1)$$

which were fit to the data using a linear regression technique (32). In table V-I the results from fitting all of the observed fluxes to these exponential functions are summarized. As can be seen, the decay time constants τ tend to decrease with increasing proton energy. These results will be discussed more fully in chapter VI.

It should be pointed out that there are statistically significant deviations from the exponential decay of these proton fluxes. We will primarily be interested in investigating the effects of energy change processes during the passage of energetic charged particles through interplanetary space. The theoretical models which we will utilize in this investigation require several simplifying assumptions in order to have tractable solutions. Among these are that the solar wind velocity be constant, and that the observations be made from a fixed location in space. Upon

TABLE V-I

EXPONENTIAL DECAY TIME CONSTANTS

Energy Range	Absolute Fluxes		Adjusted Fluxes	
	τ(hrs)	χ^2	τ(hrs)	χ^2
1.174-1.268	23.4±0.1	5.3	23.4±0.1	
1.268-1.373	23.6±0.1	4.0	23.3±0.1	2.3
1.373-1.485	22.6±0.2	3.5	22.9±0.1	1.3
1.485-1.607	22.8±0.2	5.4	22.9±0.2	2.2
1.607-1.733	22.8±0.2	4.5	23.1±0.2	1.7
1.733-1.865	22.8±0.2	3.7	22.7±0.2	1.6
1.865-2.001	22.2±0.2	2.5	22.1±0.2	1.4
2.001-2.141	22.3±0.2	3.4	22.1±0.2	1.5
2.141-2.280	21.5±0.2	2.6	21.4±0.2	1.3
2.280-2.419	21.7±0.2	1.7	21.7±0.2	1.2
2.419-2.560	22.0±0.2	2.4	22.0±0.2	1.8
2.560-2.703	21.6±0.2	2.2	21.4±0.2	1.5
2.703-2.847	21.5±0.3	2.8	21.6±0.2	1.3
2.847-2.993	20.2±0.2	5.0	20.4±0.2	1.2
2.993-3.141	20.9±0.3	2.0	20.8±0.3	1.1
3.141-3.300	20.2±0.2	1.7	20.2±0.2	1.3
3.30-3.60	20.4±0.3	3.7	20.5±0.2	1.6
3.60-4.00	19.8±0.2	3.4	20.3±0.2	1.6
4.00-4.50	20.0±0.2	3.6	20.0±0.2	1.8
4.50-5.00	19.6±0.3	2.1	20.1±0.2	1.5
5.00-6.00	19.7±0.2	1.9	19.6±0.2	1.3
6.00-7.00	18.2±0.3	1.6	18.3±0.3	1.2
7.00-9.00	17.6±0.3	1.3	17.8±0.3	1.2
9.00-15.00	18.4±0.5	1.0	18.2±0.5	0.9

studying the fluxes plotted in figure V-1, we note that at any given time the deviations from exponential decay tend to be correlated. This indicates that these deviations from exponential decay of the fluxes are due to some energy independent process. Likely causes for the observed deviations are fluctuations in the solar wind velocity, or fluctuations in the sampling location for the data. We assume that the observations which we make from within the earth's magnetic field are representative of the near earth interplanetary flux of particles. It is quite possible that the structure of the magnetosphere results in our sampling from a varying location in space. In any case, we will assume, as is indicated from the data, that the cause of the variations in our data is an energy independent process; and as a first order correction we will adjust the data so that during the period of interest, the 1.17-1.27 MeV flux will be exactly exponential, the exponential being the one derived from the linear regression fit. That is, we let a(t) be the adjustment parameter defined by

$$a(t) = \frac{F_{abs}(t_0,1.17)\ \exp\left[-(t-t_0)/\tau_{1.17}\right]}{F_{abs}(t,1.17)} \qquad (5\text{-}2)$$

then

$$F_{adj}(t,T) = F_{abs}(t,T) \times a(t) \qquad (5\text{-}3)$$

The effect of this adjustment on the fluxes is evident from the results of the linear regression used to fit the data. In table V-I we have listed the values of the time constant for exponential decay and the goodness of fit parameter χ^2 for fits to the decay with and without the adjustment. In all cases the value of χ^2 for the fit to the adjusted data is smaller than for the absolute data which indicates that the adjustment has indeed resulted in a more nearly exponential time dependence for the fluxes. The decay time constants in either case are essentially the same indicating that the adjustment has not altered any of the energy dependent features of the data. In addition to looking at the time dependence of the flux of protons at a specific energy, we will also be interested in the spectrum of protons at various times. For this purpose it is useful to have available plots of the differential density spectrum which are related to the flux spectra by

$$n(T \to T+\Delta T) = \frac{4\pi\ F(T \to T+\Delta T)}{v} \qquad (5\text{-}4)$$

where n = protons/cm^3 MeV

F = protons/cm^2 sec ster MeV

v = velocity of protons with energy $T+\frac{\Delta T}{2}$

Examples of adjusted spectra are shown in figure V-2. Notice that two power laws in kinetic energy have been fit to the data.

$$n(T) = n_0 T^{-\gamma} \qquad (5\text{-}5)$$

At the lower energies the power law index $\gamma = 2.6 \pm .1$ and at the higher energies $\gamma = 4.2 \pm .3$. These power laws appear to fit the data quite well, with representative values of χ^2 being ~0.5-1.0. The specific values of γ used above are the values obtained from fitting all of the data as will be discussed in chapter VI. At this point it is sufficient to note that there is a good fit obtained using these power law functions and varying only n_0. The four spectra shown in figure V-2 are derived from data taken at approximately 24 hour intervals. As indicated by the arrow, the energy at which the power law functions intersect is changing with time. In fact this energy is decreasing approximately exponentially with a time constant of about 200 hours. That is,

$$\frac{1}{T}\frac{dT}{dt} \simeq -1/200 \text{ hours}$$

This is our first direct observation of the existence of energy change processes in the interplanetary medium. In the following chapter, we will discuss theoretical models in an attempt to explain and understand these observations.

Figure V-2

Adjusted differential density spectra of protons from the 7 June 1969 solar flare during the decay of this event. The dashed lines are power law fits to the spectra; the arrow indicates the motion of the intersection in the two power laws which are fit to each spectrum.

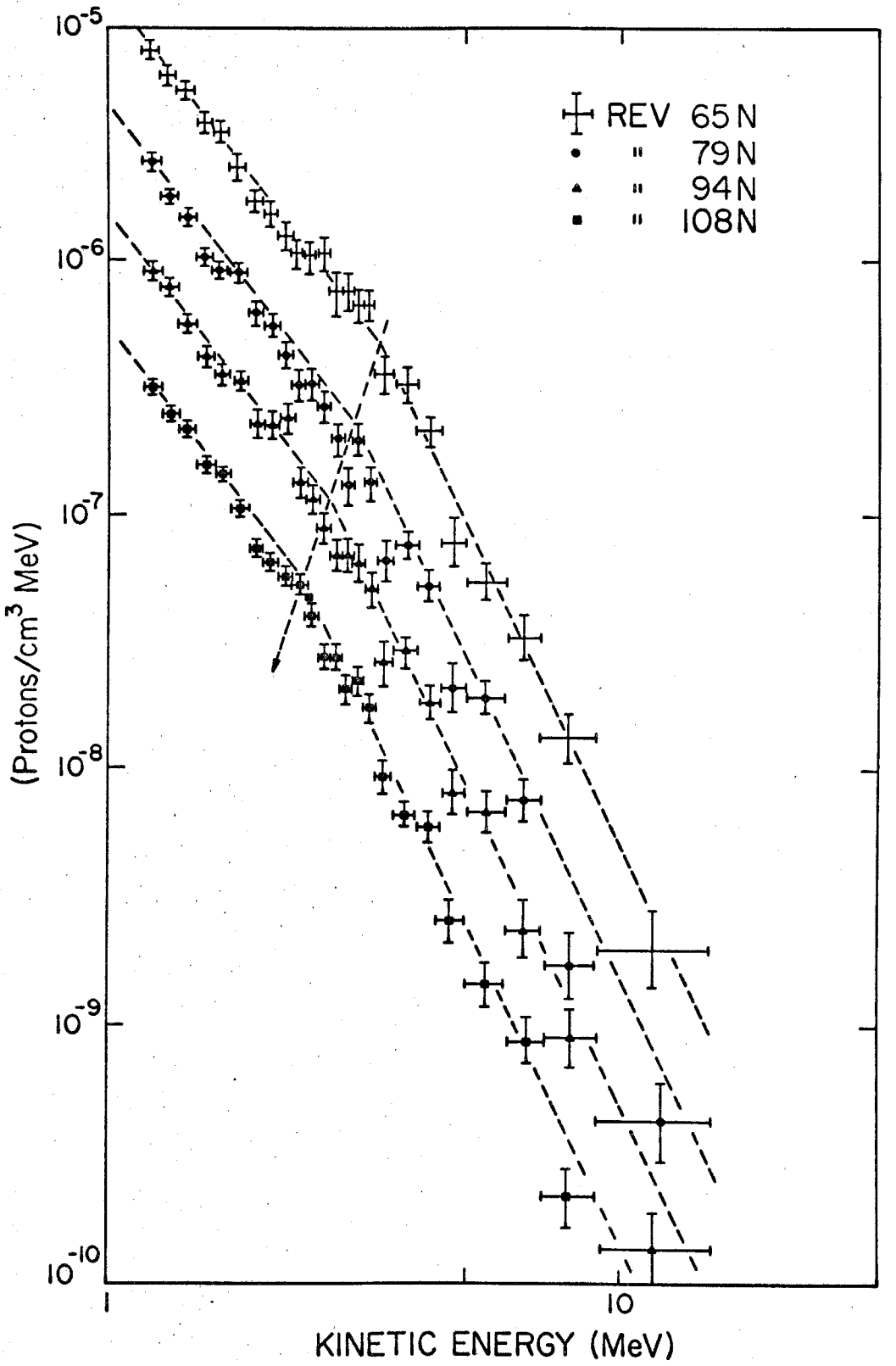
REV 65N
" 79N
" 94N
" 108N
(Protons/cm³ MeV)
KINETIC ENERGY (MeV)
10⁻⁵
10⁻⁶
10⁻⁷
10⁻⁸
10⁻⁹
10⁻¹⁰
1
10

VI. DISCUSSION AND RESULTS

A) Background

The general properties of interplanetary space are taken to be those predicted by Parker (33, 34) and later confirmed by extensive observations (35, 36, 37). In this model, the average interplanetary magnetic field is an extension of the general solar field which has been drawn outward into a spiral pattern by the solar wind. The solar wind is itself an extension of the solar corona and is blowing radially outward from the sun. There are significant fluctuations present in the magnitude and direction of the interplanetary magnetic field. Figure VI-1 illustrates schematically these features with a view of the interplanetary field in the equatorial plane of the sun. The angle Ψ of the average magnetic field with the radial direction is given by

$$\Psi = \tan^{-1}\left(\frac{\Omega_\odot r}{V_{sw}}\right) \qquad (6\text{-}1)$$

$\Omega_\odot$ = angular velocity of the sun $\sim 2.9 \times 10^{-6} \text{sec}^{-1}$

r = radial distance from the sun

V_{sw} = solar wind speed

Typical values for the magnitude of the interplanetary magnetic field are ~1 gauss at the sun and ~5 gamma

Figure VI-1

Schematic view of the interplanetary magnetic field projected in the equatorial plane of the sun (5). $\Omega_\odot$ is the angular speed at which the sun rotates; Ψ is the angle of the average spiral field with the radial direction $\hat{e}_r$. V_{sw} is the solar wind velocity. The magnetic lines of force do not actually cross, but are twisted in three dimensions.

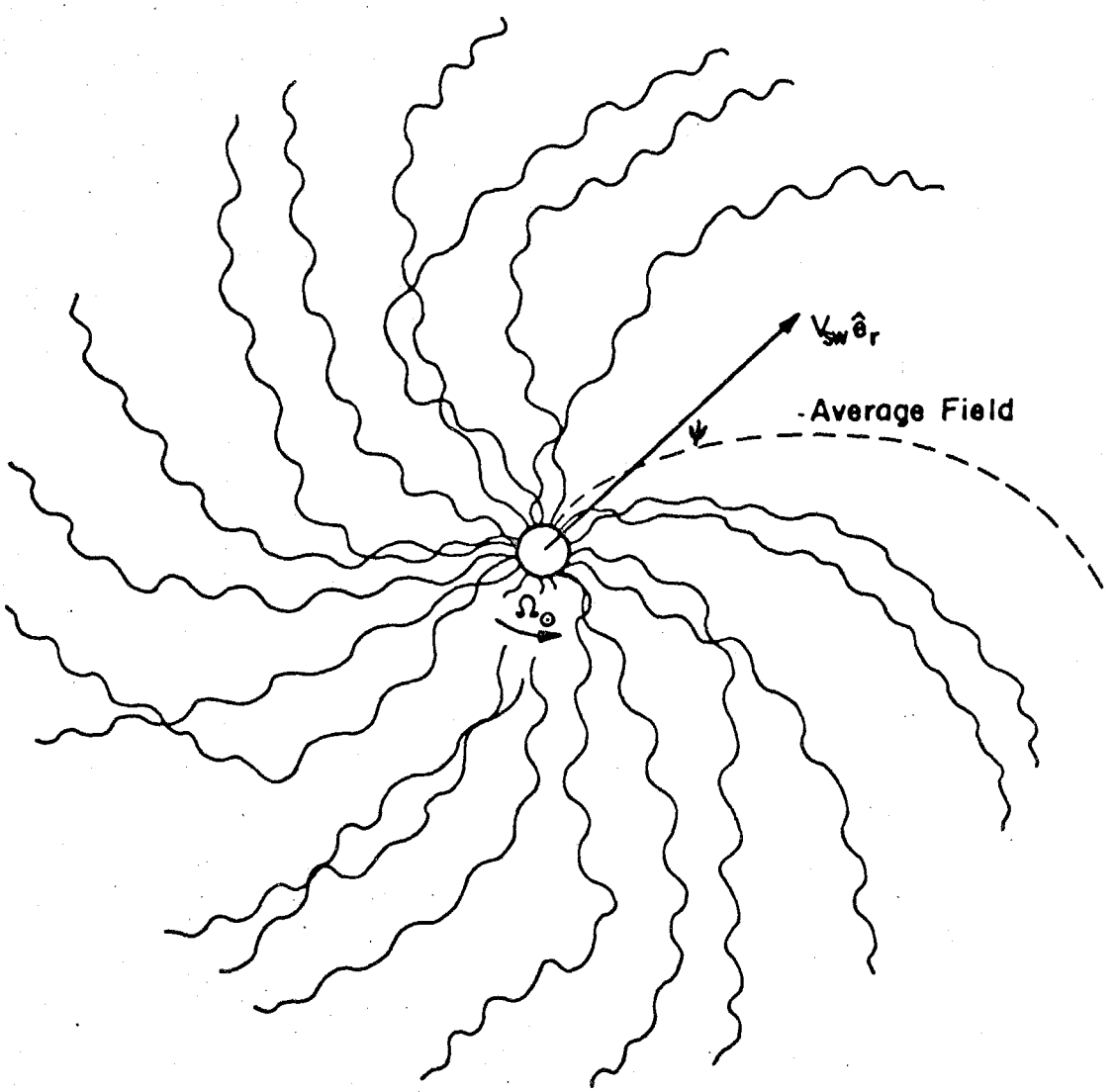
$V_{sw}\hat{e}_r$
Average Field
Ψ
$\Omega_\odot$

(1 gamma = 1 x 10^{-5} gauss) at 1 AU. The solar wind speed is typically 300-400 km/sec (5). At 1 AU, with a solar wind speed of 400 km/sec, the angle Ψ as given by equation 6-1 is

$$\Psi \simeq 48°.$$

The fluctuations in the interplanetary magnetic field act as scattering centers for the energetic charged particles which are present in space (38, 39). This scattering results in a random walk or diffusion of these particles through the field. The idea of interplanetary diffusion was first postulated by Meyer, Parker and Simpson in 1956 (40), but it was not until 1958 when Parker postulated the existence of the solar wind that there was a simple model which contained diffusion as a natural consequence. Parker also pointed out (34) that the fluctuations in the magnetic field, which are frozen into the solar wind plasma, will tend to convect particles away from the sun at the solar wind speed. In addition the non-vanishing divergence of the solar wind velocity as the plasma expands in space results in the adiabatic cooling of particles which are diffusing in the interplanetary medium (41, 42).

These physical process - diffusion, convection and energy changes - can be incorporated into a single equation which describes the conservation of particles with kinetic

energy T at a point in space (5, 41).

$$\frac{\partial n}{\partial t} = \nabla\cdot(\underline{\kappa}\nabla\cdot n) - \nabla\cdot(n\vec{V}_{sw}) - \frac{\partial}{\partial T}\left(n\frac{dT}{dt}\right) \qquad (6\text{-}2)$$

where

$n(r,t,T)$ is the differential density of particles with kinetic energy T to T + dt.

$\vec{V}_{sw}$ is the solar wind velocity.

$\underline{\kappa}$ is the diffusion tensor.

In a coordinate system with Z axis along the average magnetic field we have

$$\kappa_{ij} = \begin{pmatrix} \kappa_\perp & -\kappa_d & 0 \\ \kappa_d & \kappa_\perp & 0 \\ 0 & 0 & \kappa_\parallel \end{pmatrix}$$

where $\kappa_\parallel$ and $\kappa_\perp$ are the components along and perpendicular to the average field; κ_d is the diffusion coefficient due to curvature and gradient drifts (5, 41).

The diffusion tensor is a function of position, particle energy and time, and the magnitudes of the components of this tensor are related to the interplanetary magnetic field. An analytical form for this relationship was derived by Jokipii in 1966-1967 (8, 9, 10), the result

being that the diffusion tensor components $\kappa_{\parallel}$ and $\kappa_{\perp}$ are related to the power contained in the fluctuations of the magnetic field. Specifically Jokipii (5) has shown that, if the power spectrum of the fluctuations of the magnetic field is in the form of a power law in wave number k, that is,

$$P_{xx}(k) = Ak^{-\alpha} \qquad (6\text{-}3)$$

where A and α are constants

xx refers to a transverse component of the magnetic field

k is the wave number $k = 2\pi f/V_{sw}$

where f = frequency

then
$$\kappa_{\parallel} = c\left[\frac{\alpha(\alpha-2)}{9A}\right] B_0^{\alpha}\, e^{\alpha-2}\, R^{2-\alpha}\, \beta \qquad (6\text{-}4)$$

where c is the speed of light

B_0 is the average magnitude field strength

R is the particle rigidity ($R = Pc/Ze$)

β is the particle speed in units of c ($\beta = v/c$)

Also, for any form of the power spectrum,

$$\kappa_{\perp} = \frac{1}{2}\frac{\beta c}{B_0^2} P_{xx}\ (k = 0) \qquad (6\text{-}5)$$

The antisymmetric part of the diffusion tensor is given by

$$\kappa_d = \frac{1}{3}\beta c\, r_c \frac{B_0}{|B_0|}$$

where r_c = cyclotron radius $\left(r_c = R/|B_0|\right)$ (6-6)

Using the magnetic field observations from Mariner IV as analyzed by Jokipii and Coleman (43), and Jokipii and Parker (44), explicit forms for $\kappa_{\parallel}$ and $\kappa_{\perp}$ are found (5) which can be taken as estimates correct to about 50%. These are:

$$\kappa_{\parallel} \sim 5 \times 10^{21} \beta R^{\frac{1}{2}} \qquad 0.1 \lesssim R \lesssim 1 \text{ GV} \quad (10 \lesssim T \lesssim 500 \text{ MeV}) \qquad (6\text{-}7a)$$

$$\kappa_{\perp} \sim 2 \times 10^{21} \beta \text{ cm}^2/\text{sec} \qquad R \lesssim 1 \text{ GV} \quad (T \lesssim 500 \text{ MeV}) \qquad (6\text{-}7b)$$

$$\kappa_{\parallel} \sim 5 \times 10^{21} \beta R^2 \text{ cm}^2/\text{sec} \qquad R \gtrsim 1 \text{ GV} \quad (T \gtrsim 500 \text{ MeV}) \qquad (6\text{-}7c)$$

$$\kappa_{\perp} \sim 4 \times 10^{21} \beta \text{ cm}^2/\text{sec} \qquad R \gtrsim 1 \text{ GV} \quad (T \gtrsim 500 \text{ MeV}) \qquad (6\text{-}7d)$$

For rigidities less than ~0.1 GV (≲10 MeV protons), Jokipii (45) has argued that the parallel diffusion coefficient should become rigidity independent, giving:

$$\kappa_{\parallel} \sim 1.8 \times 10^{21} \beta \text{ cm}^2/\text{sec} \qquad R \lesssim 0.1 \text{ GV} \quad (T \lesssim 10 \text{ MeV}) \qquad (6\text{-}8)$$

Observations from Mariner IV (43) also indicate that $\kappa_{\parallel}$ is constant between 1.0 and 1.5 AU. However, due to the uncertainty in the value for this coefficient as derived from the Mariner data, it is not possible to completely rule out any spatial dependence for $\kappa_{\parallel}$. Theoretical considerations (46, 47) indicate that the perpendicular diffusion coefficient should vary as r^2 (r = radial distance from the sun.

As was already mentioned, one energy change process affecting energetic charged particles as they propagate in the solar wind is the adiabatic energy loss due to the expansion of the solar wind. This results in a rate of change of kinetic energy given by (41)

$$\frac{dT}{dt} = \frac{1}{3} \alpha T \, (\nabla \cdot \vec{V}_{sw}) \qquad (6\text{-}9)$$

where

$$\alpha = \frac{T + 2T_0}{T + T_0}, \quad T_0 = \text{rest energy}$$

There are probably other energy change processes which occur while particles are moving in the solar wind. Parker (34) has discussed the effects of Fermi acceleration mechanisms (2, 48) in the solar wind and concludes that except at energies less than ~10 MeV for protons, the effects of Fermi acceleration are negligible. We will initially consider only uniform adiabatic deceleration of cosmic rays in the theoretical models which we will investigate. Using the explicit form for energy loss given by equation 6-9, we have from equation 6-2

$$\frac{\partial n}{\partial t} = \nabla \cdot (\underline{\underline{\kappa}} \nabla n) - \nabla \cdot (n \vec{V}_{sw}) + \frac{1}{3} \nabla \cdot \vec{V}_{sw} \frac{\partial}{\partial T} (n \alpha T) \qquad (6\text{-}10)$$

This equation first appeared in 1965 (41), and at present there are only limited solutions for special forms of the parameters $\underline{\underline{\kappa}}$ and $\vec{V}_{sw}$.

B) Discussion

Although there has been no general solution to the transport equation 6-10, we can investigate solutions to this equation for limiting parameter values. First, we consider the relative magnitudes of the various terms of the right hand side of the equation. To do this let L be the characteristic scale length for variations in the differential density n, $L \simeq \frac{n}{|\nabla n|}$, and assume that the solar wind velocity is radial and constant. We will also consider only radial diffusion in determining these relative magnitudes. Finally, assume that the differential density spectrum is a power law in kinetic energy so that

$$n(T) = n_0 T^{-\gamma} \qquad (6\text{-}11)$$

Then each of the terms of the right hand side of equation 6-10 can be approximated as follows:

Term			Process	
$\nabla\cdot(\underline{\underline{\kappa}}\nabla n)$	$\simeq$	$\frac{\kappa_{\parallel} n}{L^2}$	Diffusion	(6-12a)
$\nabla\cdot(n\vec{V}_{sw})$	$\simeq$	$\frac{nV_{sw}}{L}$	Convection	(6-12b)
$\frac{1}{3}(\nabla\cdot\vec{V}_{sw})\frac{\partial}{\partial T}(n\alpha T)$	$\simeq$	$\frac{2V_{sw}}{3r}\alpha n(\gamma-1)$	Adiabatic Deceleration	(6-12c)

During the decay phase of a solar flare, we know that the particles emitted from the sun have extended into space filling a region that extends beyond the orbit of the earth ($r \sim 1$ AU). In this case, we expect that the scale length L will be of the order of 1 AU, and we will take $L = r$ for the comparison of terms. Doing this we find that the diffusion term will dominate when

$$\kappa_{\parallel} >> \frac{2\ V_{sw}}{3}\ \alpha(\gamma-1)\ r \qquad (6\text{-}13a)$$

For typical parameter values,

$$r = 1 \text{ AU}$$
$$V_{sw} = 400 \text{ km/sec}$$
$$\gamma = 3.5$$

this becomes

$$\kappa_{\parallel} >> 10^{21} \text{ cm}^2/\text{sec} \qquad (6\text{-}13b)$$

When equation 6-13 is valid, the convection and adiabatic deceleration terms can be neglected and the transport equation is

$$\frac{\partial n}{\partial t} = \nabla\cdot(\underline{\underline{\kappa}}\nabla n). \qquad (6\text{-}14)$$

Similarly, if

$$\kappa_{\parallel} << 10^{21} \text{ cm}^2/\text{sec} \qquad (6\text{-}15)$$

then the convection and deceleration terms will dominate and in the limit where diffusion can be neglected the transport equation becomes

$$\frac{\partial n}{\partial t} = -\nabla\cdot(n\vec{V}_{sw}) + \frac{1}{3}(\nabla\cdot\vec{V}_{sw})\frac{\partial}{\partial T}(n\alpha T) \qquad (6\text{-}16)$$

1) Diffusion Model

Solutions to equation 6-14 for various forms of the diffusion tensor and boundary conditions have appeared in the literature (31, 40). The earliest application of this equation to solar flare observations is the 1956 paper by Meyer et al. (40) in which solutions to equation 6-14 for isotropic radial diffusion were discussed. The observation by these authors of an exponential decay of the particle fluxes indicated the presence of a boundary to the region in which these particles diffuse. The Meyer et al. observations were at energies greater than 2 GeV for protons. Another solution to equation 6-14 was given by Burlaga (31). This solution considers the effects of anisotropic diffusion in a bounded medium, and was used by Burlaga to fit observations of solar flare protons with energies greater than 100 MeV.

In both of these examples, the values of $\kappa_{\parallel}$ which are obtained by fitting the observations to the models are of the order of 1×10^{22} cm^2/sec. This value for the

diffusion coefficient is compatible with the conditions necessary for the neglect of convection and adiabatic deceleration, i.e. equation 6-13b. It is worth pointing out that the values for $\kappa_{\parallel}$ predicted by Jokipii in equations 6-7 also indicate that diffusion is an important process for particle transport at these energies. Using equation 6-7a, we find $\kappa_{\parallel} \simeq 1.5 \times 10^{21}$ cm^2/sec at 100 MeV, and using equation 6-7c we find $\kappa_{\parallel} \simeq 3.5 \times 10^{22}$ cm^2/sec at 2 GeV. Also, the values of the parallel and perpendicular diffusion coefficients down to about 10 MeV which are derived from galactic cosmic ray observations are in good agreement with the values computed from equations 6-7 (5).

The fits made by Burlaga to several solar flare observations indicate that the boundary of the diffusion region is between 2 and 3 AU. The best estimate for the boundary radius is 2.3 ±0.3 AU. This value is in good agreement with values derived from the modulation of galactic cosmic rays (5).

At energies greater than 100 MeV, Burlaga has been able to fit not only the decay, but also the rise of many solar flare events using the transport equation 6-14. This is not surprising since the scale length L for variations in the differential density is probably smaller than 1 AU at times early in the flare and we expect diffusive processes

to be dominant when compared to convection or deceleration processes.

Observations at low energies ($\lesssim$10 MeV) of the decay of solar flare events can also be fit to the diffusion equation 6-14. For example, Lanzerotti (49) fits observations for solar flare protons from 2-20 MeV to a diffusion model assuming isotropic radial diffusion, and finds that the diffusion coefficient is approximately constant over this energy interval, with a value $\kappa_{\parallel} \simeq 2.3 \times 10^{21}$ cm^2/sec. Lanzerotti also finds that the boundary of the diffusion region is about 2.5 AU. This value of the diffusion coefficient $\kappa_{\parallel}$ is necessary to produce the observed exponential decay time constant of about 15 hours. However, comparing this value of $\kappa_{\parallel}$ with the critical value given in equation 6-13b, we find that it is important to consider the effects of convection and adiabatic deceleration. It is of interest to note that the value for $\kappa_{\parallel}$ which one gets from equation 6-7 for 10 MeV protons differs considerably from Lanzerotti's value. That is,

$$\kappa_{\parallel} \text{ (equation 6-7)} = 2.7 \times 10^{20} \text{ cm}^2/\text{sec}$$

$$\kappa_{\parallel} \text{ (Lanzerotti)} = 2.3 \times 10^{21} \text{ cm}^2/\text{sec}$$

While it is possible that the form for $\kappa_{\parallel}$ derived by Jokipii is not correct, it is also possible that the value which is obtained by fitting observations at low energies to equation 6-14 is incorrect, or at least the interpretation of this number as a diffusion coefficient is incorrect.

Observations of the 7 June 1969 flare which are reported in this thesis can also be fit to equation 6-14. We have used the solution derived by Burlaga (31) for anisotropic diffusion as the form of the theoretical model with which to fit our data. [In the limit of long times, this becomes equivalent to the model used by Lanzerotti (49).] For the decay phase of a flare this solution is

$$n(r,t,T) \simeq \frac{n_0(T)}{2rD^2} \sin\left(\frac{\pi r}{D}\right) \exp\left(-\frac{\pi^2 \kappa_{\parallel} t}{D^2}\right) \qquad (6\text{-}17)$$

where D = boundary radius beyond which $n(r,t,T) = 0$

Thus, in the application of this solution to observations made during the exponential decay of an event, the time constants from fits to exponential decay are related to the diffusion coefficient $\kappa_{\parallel}$ and the location of the boundary D.

$$\tau_{decay} = D^2/\pi^2\kappa_{\parallel} \qquad (6\text{-}18)$$

Taking D = 2.3 AU, we can calculate $\kappa_{\parallel}$ from the observed decay time constants. This gives $\kappa_{\parallel} \simeq (1.4\text{-}1.8) \times 10^{21}$ cm^2/sec

for energies from 1-10 MeV. Again the values of the diffusion coefficient indicate that the assumptions required for equation 6-14 to be valid are not necessarily correct and therefore the interpretation that the decay phase is dominated by diffusive processes may be incorrect.

2) Convection-Adiabatic Deceleration (CAD) Model

If the values for the diffusion coefficients given by equations 6-7 can be believed, we would expect that convection and adiabatic deceleration processes are important and perhaps even dominate the decay of solar flares in the energy range 1-10 MeV. Therefore, we will investigate a solution to equation 6-16 which was given by Forman (50). Observations of several solar flares with the Pioneer satellites (51) indicate the existence of a persistent, small radial anisotropy in the flux of low energy particles, that is, a net streaming of these particles away from the sun. Forman has shown that these observations imply that convection and adiabatic deceleration dominate the decay phase of these events. In addition, as will be shown below, the radial anisotropy observations imply that the term in equation 6-16 involving the radial gradient of the differential density is small compared to the other terms in this equation. Assuming a spherically symmetric solar wind, equation 6-16 becomes

$$\frac{\partial n}{\partial t} = - V_{sw} \frac{\partial n}{\partial r} - \frac{2 V_{sw}}{r} n + \frac{2 V_{sw}}{3r} \frac{\partial}{\partial T} (n\alpha T) \qquad (6\text{-}19)$$

Equation 6-19 (as is true for all preceding equations involving the differential density) tacitly assumes that the differential density is isotropic (52). A small anisotropy (~5-10%) does not alter any of these equations provided that the density considered is the true density (including solid angle dependence) integrated over solid angle (52). That is,

$$n_{used} = n_0(r,t) = \int n(r,\Omega,t)\, d\Omega \qquad (6\text{-}20)$$

For small anisotropies, we can expand the density in a Fourier series keeping only the lowest order terms.

$$n(r,\Omega,t) = \frac{n_0(r,t)}{4\pi} (1 + \delta \cos \theta) \qquad (6\text{-}21)$$

The net flux of particles with velocity w can be calculated from the density of these particles

$$|\vec{F}| = 2\pi \int_0^{\pi} n(r,\Omega,t)\, w \cos \theta \sin \theta \, d\theta \qquad (6\text{-}22a)$$

$$= \frac{1}{3} n_0 w \delta \qquad (6\text{-}22b)$$

Therefore, the anisotropy magnitude and direction (which

is in the direction of the flux) is

$$\vec{\delta} = \frac{3\vec{F}}{n_0 w} \qquad (6\text{-}23)$$

For the flux due to diffusion the corresponding anisotropy is (50)

$$\vec{\delta}_D = \frac{-3\underline{\underline{\kappa}}\nabla n}{nw} \qquad (6\text{-}24)$$

where the subscript on n has been suppressed as we have been doing in all of the previous equations. This would be the anisotropy observed in a frame of reference moving with the solar wind. In transforming to a coordinate system at rest with respect to the sun, an additional anisotropy in the flux is introduced. This is the Compton-Getting effect (53), and the resulting anisotropy is given by (50)

$$\vec{\delta}_{CG} = \left(2 + \alpha(\gamma + \tfrac{1}{2})\right) \frac{\vec{V}_{sw}}{w} \qquad (6\text{-}25)$$

where the density is assumed to be a power law in kinetic energy $n(T) = n_0 T^{-\gamma}$.

When the anisotropy due to diffusion (δ_D) is much less than that due to convection (δ_{CG}), Forman (50) has shown that

$$\frac{\partial n}{\partial r} << \frac{2}{r}\left(n - \frac{1}{3}\frac{\partial}{\partial T}(n\alpha T)\right) \qquad (6\text{-}26)$$

So we have from equation 6-19

$$\frac{\partial n}{\partial t} \simeq -\frac{2\ V_{sw}}{r}\, n + \frac{2}{3}\,\frac{V_{sw}}{r}\,\frac{\partial}{\partial T}\,(n\alpha T) \qquad (6\text{-}27)$$

When equation 6-27 is valid, the density at a time t can be calculated from the density at some other time t_0.

$$n(r,t,T) = \exp\left[-\frac{2\ V_{sw}}{3r}\,(t-t_0)\right] n(r,t_0,T_0) \qquad (6\text{-}28)$$

where

$$T_0 = T \exp\left[\frac{4\ V_{sw}}{3r}\,(t-t_0)\right]$$

This solution was obtained by Forman (50). In the case when the density spectrum is a power law in kinetic energy

$$n(T) = n_0 T^{-\gamma} \qquad (6\text{-}29)$$

then equation 6-28 yields

$$n(r,t,T) = \exp\left[-\frac{4\ V_{sw}}{3r}\,(\gamma + \tfrac{1}{2})\,(t - t_0)\right] n(r,t_0,T) \qquad (6\text{-}30a)$$

That is, exponential decay with a time constant

$$\tau_{decay} = \frac{3r}{4\ V_{sw}\,(\gamma + \tfrac{1}{2})} \qquad (6\text{-}30b)$$

We can use the observations of the 7 June 1969 flare, and also the observations of Lanzerotti (49) for the 28 May 1967 event to test this solution. The spectrum of the 7 June 1969 flare can be approximated by power laws in kinetic energy as discussed in section V. The 28 May 1967 event also has a power law density spectrum with a spectral index $\gamma \sim 3$. The decay time constants calculated using equation 6-30b are given in table VI-I as are the parameter values used and the observed time constants. As can be seen, there is good agreement between the observed and calculated time constants for the 7 June 1969 event, but not nearly so good for the 28 May flare. However, we lack sufficient information about the parameters V_{sw} and γ for the 28 May flare to make any detailed comparisons and we will not consider this event in the analysis which follows.

The CAD model also predicts the evolution of the spectrum of solar flare particles with time. Using equation 6-28, it is possible to calculate the density spectrum at any time t from the observed spectrum at an earlier time t_0. Conversely, if the spectrum at some time t is known, we can calculate n_{MB}, the map-back of the adjusted spectrum to a time t_0.

$$n_{MB}\left(t_0,T_0 = T \exp\left[\frac{4\ V_{sw}}{3r}\ (t-t_0)\right]\right) = \exp\left[\frac{2\ V_{sw}}{3r}(t-t_0)\right] n(t,T)\,a(t) \qquad (6\text{-}31)$$

TABLE VI-I

DECAY TIME CONSTANTS FOR CAD MODEL

$$\tau_{decay} = \frac{3r}{4\, V_{sw}\, (\gamma + \tfrac{1}{2})}$$

$r = 1.5 \times 10^{8}$ km = 1 AU

V_{sw} = 400 ±20 km/sec 7 June 1969 VELA observations (28)

= ~400 km/sec 28 May 1967 [estimate from Pioneer VI data (54)]

Event	Energy	γ	τ_{theory} (hrs.)	τ_{obs} (hrs.)
7 June 1969	~1	2.6±.1	25.2±1.4	23.2±.2
	~10	3.8±.1	18.2±1.1	18.4±.3
27 May 1967	~4-10	~3	~22	~15

In figure VI-2a, -b and -c we show the results of applying equation 6-31 to all of the adjusted spectra observed during the decay phase of the 7 June 1969 flare. (The spectra are referenced to time t_0 = 0227 UT on day 161.) Notice that in this equation there is only one parameter V_{sw}/r. We expect that r ≈ 1 AU, and measurements of V_{sw} from the VELA satellites (28) give V_{sw} = 400 ±20 km/sec at the earth. However, for the purposes of testing the CAD model we will assume V_{sw} to be an unknown parameter. Thus, figures VI-2a, -b and -c are for different values of the solar wind velocity V_{sw}. If the model is correct, we expect that all of the spectra at time t_0 computed using equation 6-31, will overlap resulting in a narrow band of data points on the plots.

In order to estimate the goodness of these mappings, we calculate the average spectrum at time t_0 which results from mapping with a particular value of V_{sw}. Then using this average spectrum as the 'correct' spectrum, we calculate the goodness of fit parameter χ^2 according to (32)

$$\chi^2 = \frac{1}{N} \sum_{\text{all data}} [n_i(T)_{\text{correct}} - n_i(T)_{\text{observed}}]^2/\sigma_i^2 \qquad (6\text{-}32)$$

where the σ_i are the statistical uncertainties in each mapped back data point, and N is the number of degrees of freedom.

Figure VI-2a, -b, -c

Results from mapping 72 adjusted differential density spectra for protons during the decay phase of the 7 June 1969 solar flare event to time 0227 UT on day 161. The map-back equation is 6-31 with the solar wind velocity (V_{sw}) = 350 km/sec (a)

= 400 km/sec (b)

= 450 km/sec (c)

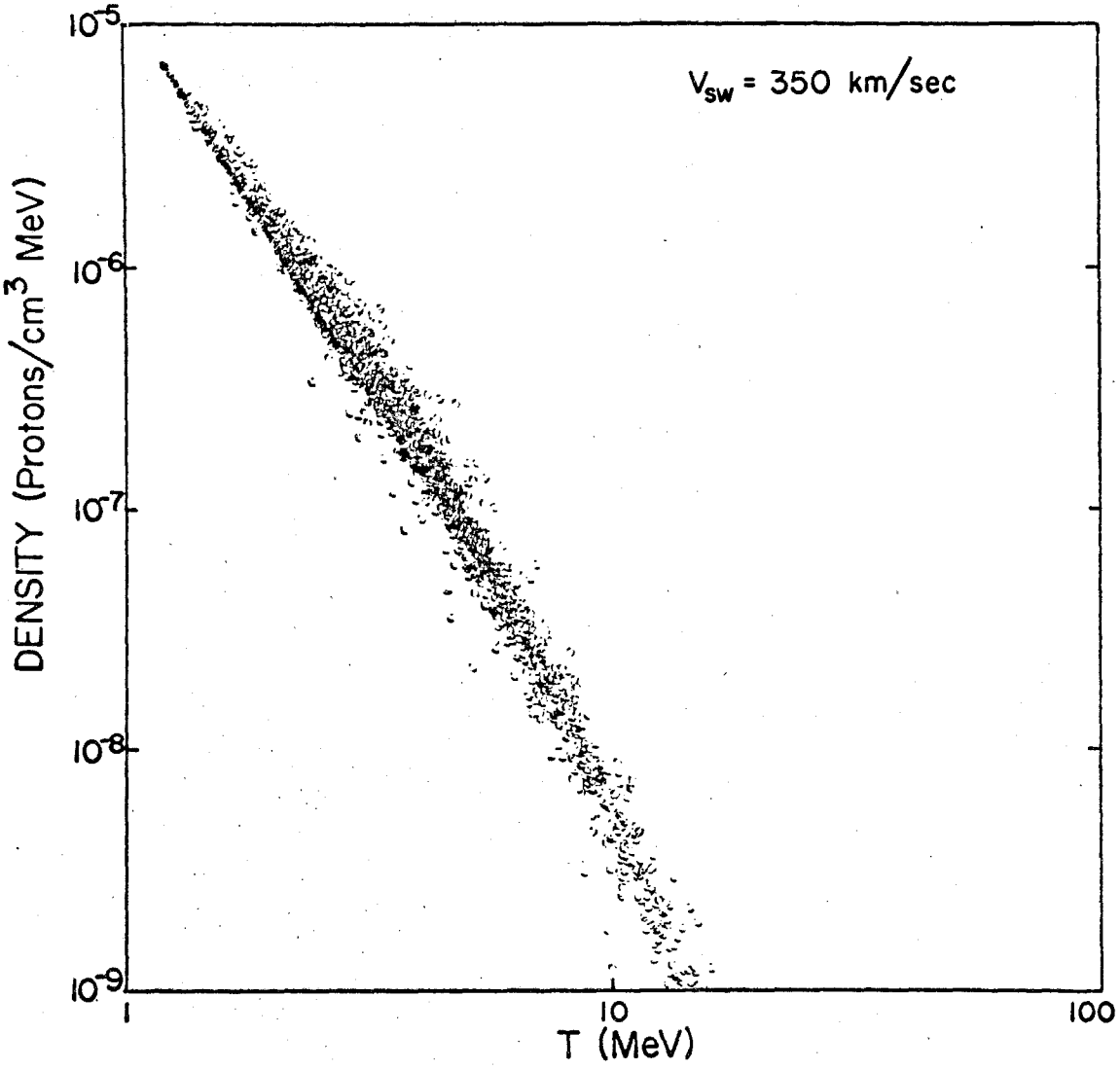
V_{sw} = 350 km/sec
DENSITY (Protons/cm^3 MeV)
10^{-5}
10^{-6}
10^{-7}
10^{-8}
10^{-9}
1
10
100
T (MeV)

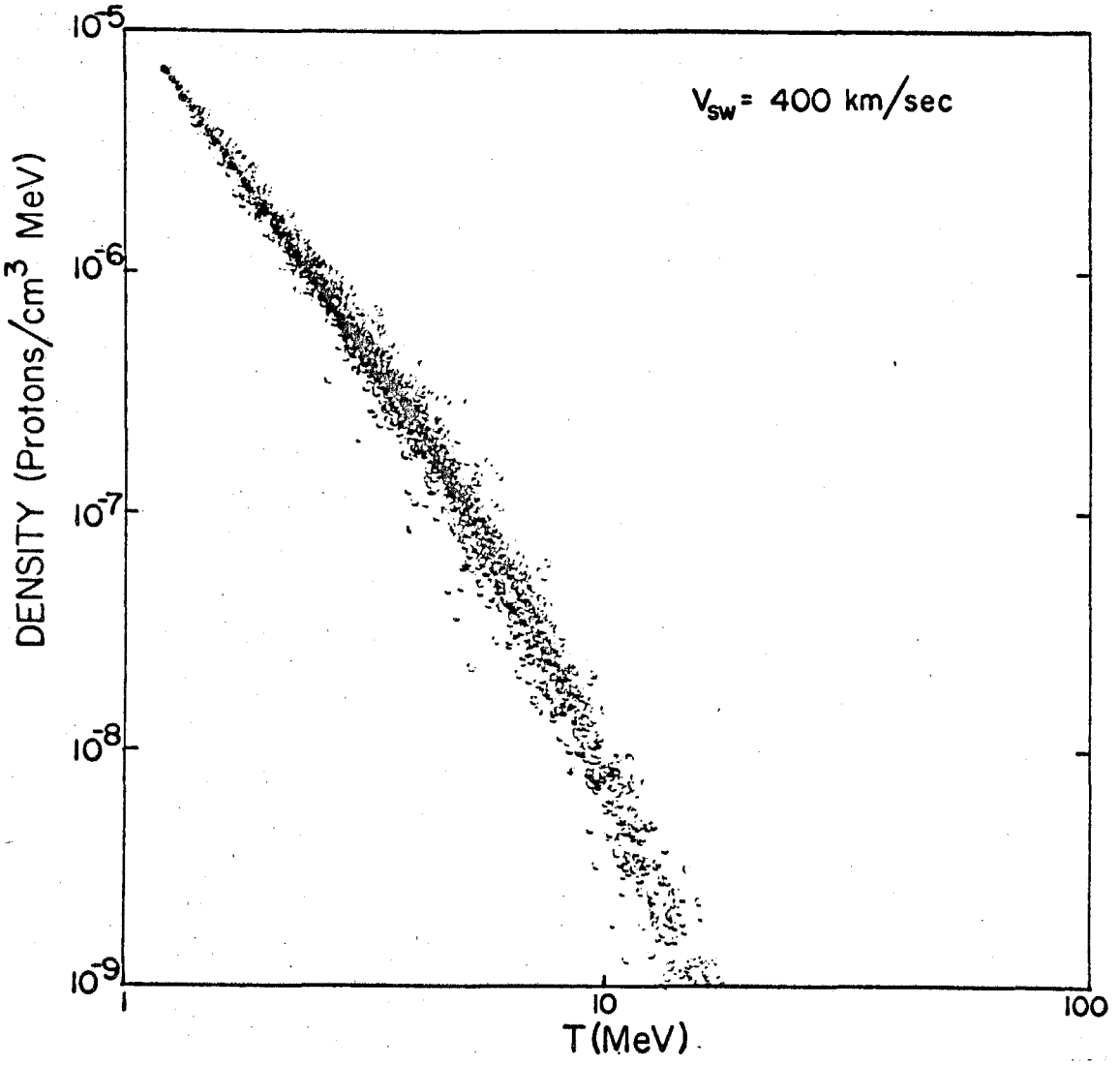
V_{sw} = 400 km/sec
DENSITY (Protons/cm^3 MeV)
10^{-5}
10^{-6}
10^{-7}
10^{-8}
10^{-9}
1
10
100
T(MeV)

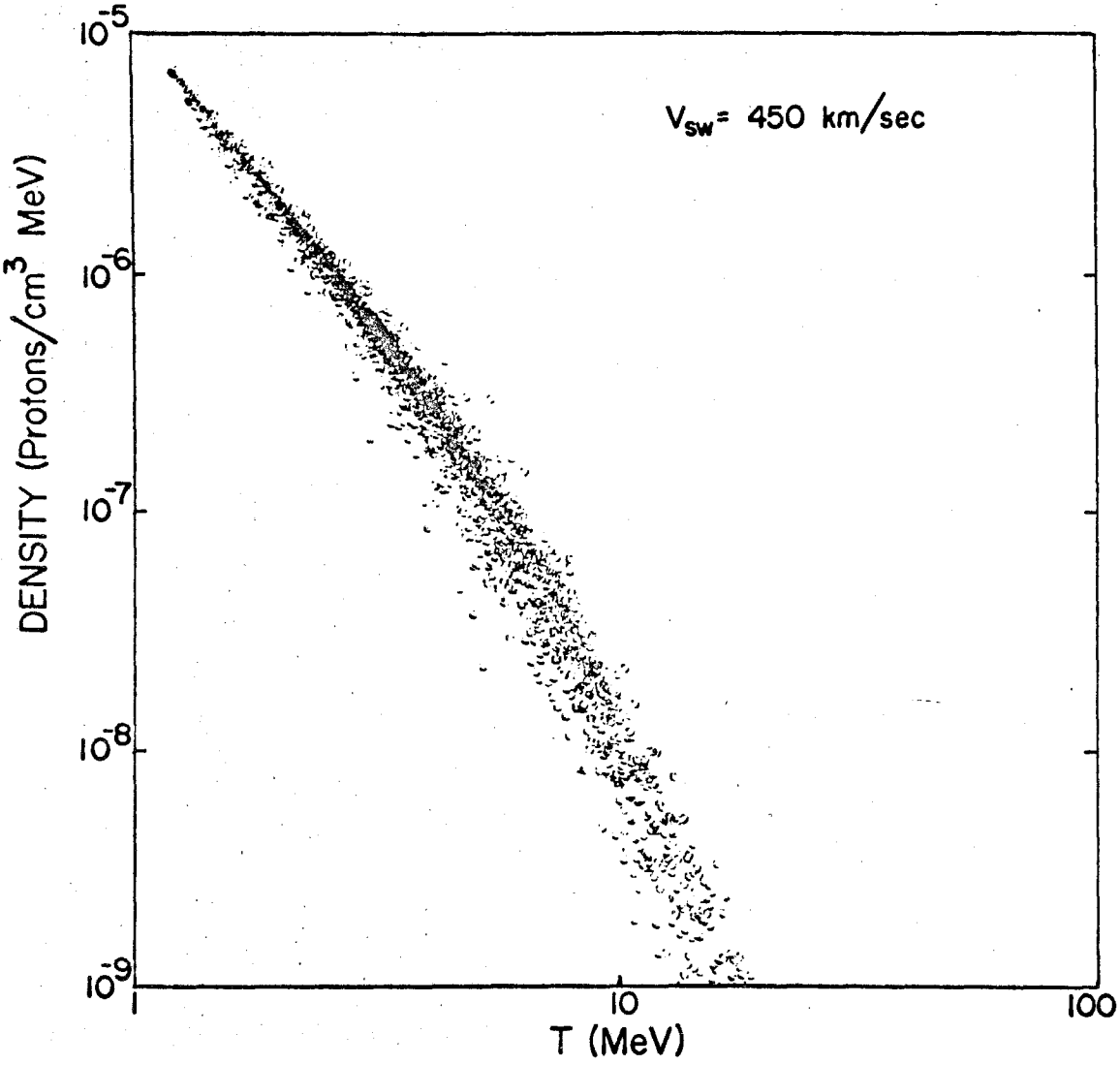
V_{sw}= 450 km/sec
DENSITY (Protons/cm^3 MeV)
10^{-5}
10^{-6}
10^{-7}
10^{-8}
10^{-9}
1
10
100
T (MeV)

In this manner we calculate χ^2 for various values of V_{sw} with the results shown in figure VI-3 which is a plot of χ^2 vs. V_{sw}. The minimum value of χ^2 of ~4 is at V_{sw} = 405 km/sec which agrees well with the expected value of 400 ±20 km/sec. Considering that there are 1756 degrees of freedom for this fit, the large value for χ^2 is an indication that there might be something wrong with the fit.

In chapter V we indicated that there appeared to be evidence for energy change processes during the decay phase of the 7 June 1969 solar flare. The CAD model of Forman assumes that the energy change is due to uniform adiabatic deceleration in a spherically symmetric expanding solar wind. Independent of the spectral mapping described above, we can investigate energy change processes by studying the behavior of the shape of the density spectrum as a function of time. As discussed in chapter V, the density spectra observed during the 7 June 1969 flare can be fit to two power laws in kinetic energy. The energy at which these power law functions intersect represents a feature of the spectrum which can be followed in time.

The CAD model predicts that the shape of the density spectrum will not change with time (50). That is, the energy dependence of the spectrum between energies T_1

Figure VI-3

Goodness of fit parameter χ^2 vs. velocity of the solar wind (V_{sw}) for the map-back procedure given by equation 6-31.

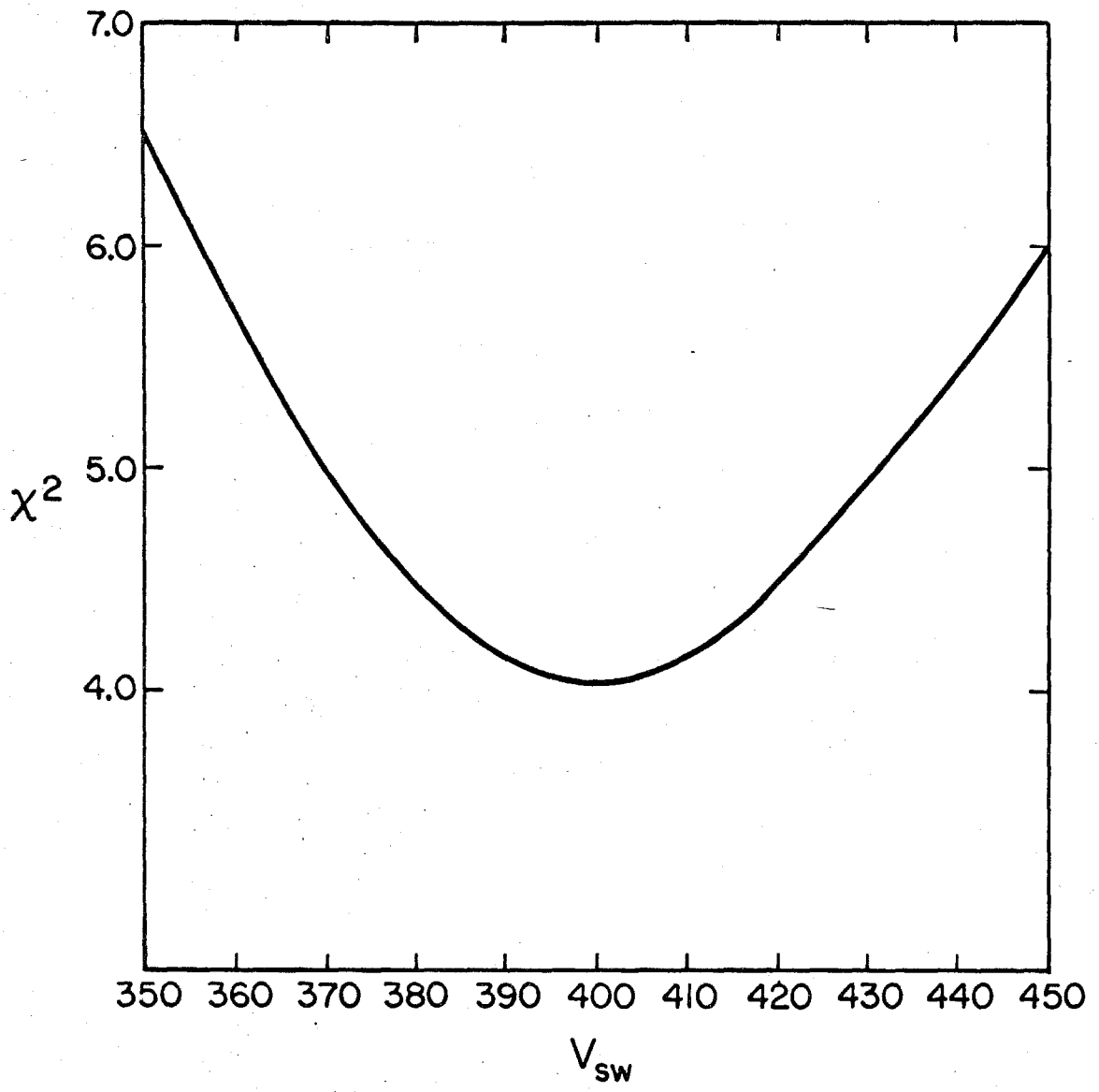
7.0
6.0
5.0
4.0
χ^2
350 360 370 380 390 400 410 420 430 440 450
V_{sw}

and T_2 at some time t_0 will be the same as the energy dependence of the spectrum between energies T_1' and T_2' at a later time t where

$$T_1' = T_1 \exp\left[-\frac{4\ V_{sw}}{3r}(t - t_0)\right]$$
$$T_2' = T_2 \exp\left[-\frac{4\ V_{sw}}{3r}(t - t_0)\right] \qquad (6\text{-}33)$$

This is illustrated schematically in figure VI-4. Thus when one spectrum can be fit by a power law in kinetic energy $n = n_0 T^{-\gamma}$, then all spectra should be fit to the same power law (varying only the normalization, n_0) provided that these fits are made between energies which are at all times included in the power law part of the spectrum. For the 7 June 1969 flare, the spectral indicies γ for which the power law fits are made are found from the average spectrum (figure VI-5) which was obtained from the map-back procedure described previously. In this case we fit the absolute density spectra to the following functions:

$$n_{abs}(T) = n_0 T^{-2.6} \qquad T < 2.5 \text{ MeV} \qquad (6.34a)$$

$$n_{abs}(T) = n_0 T^{-3.8} \qquad T > 4.0 \text{ MeV} \qquad (6.34b)$$

The intersection energies of the resultant least squares fits are plotted vs. time in figure VI-6. Since the

Figure VI-4

Schematic representation of the evolution of a differential density spectrum of solar flare particles according to the CAD model. The energy dependence of the spectrum at time t_0 between energies T_1 and T_2 is the same as that of the spectrum at time t between energies T_1' and T_2'.

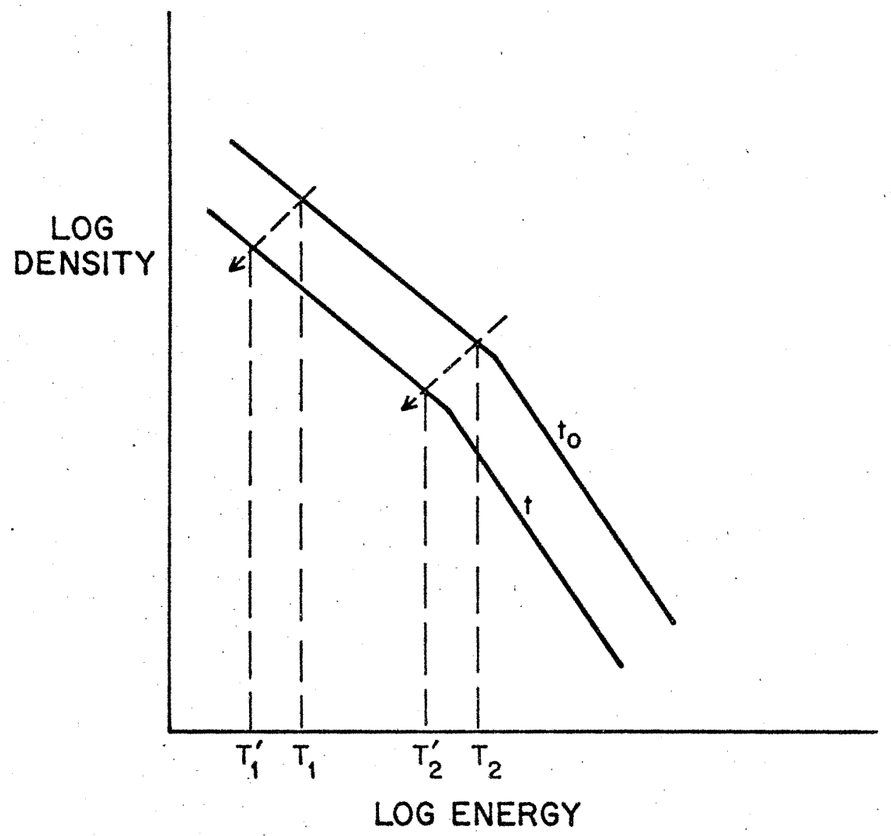
LOG
DENSITY
t_o
t
T_1'
T_1
T_2'
T_2
LOG ENERGY

Figure VI-5

Average differential density spectrum for protons for the map-back shown in figure VI-2b. T_0 is the intersection energy for the two power laws in kinetic energy which are fit to the average spectrum.

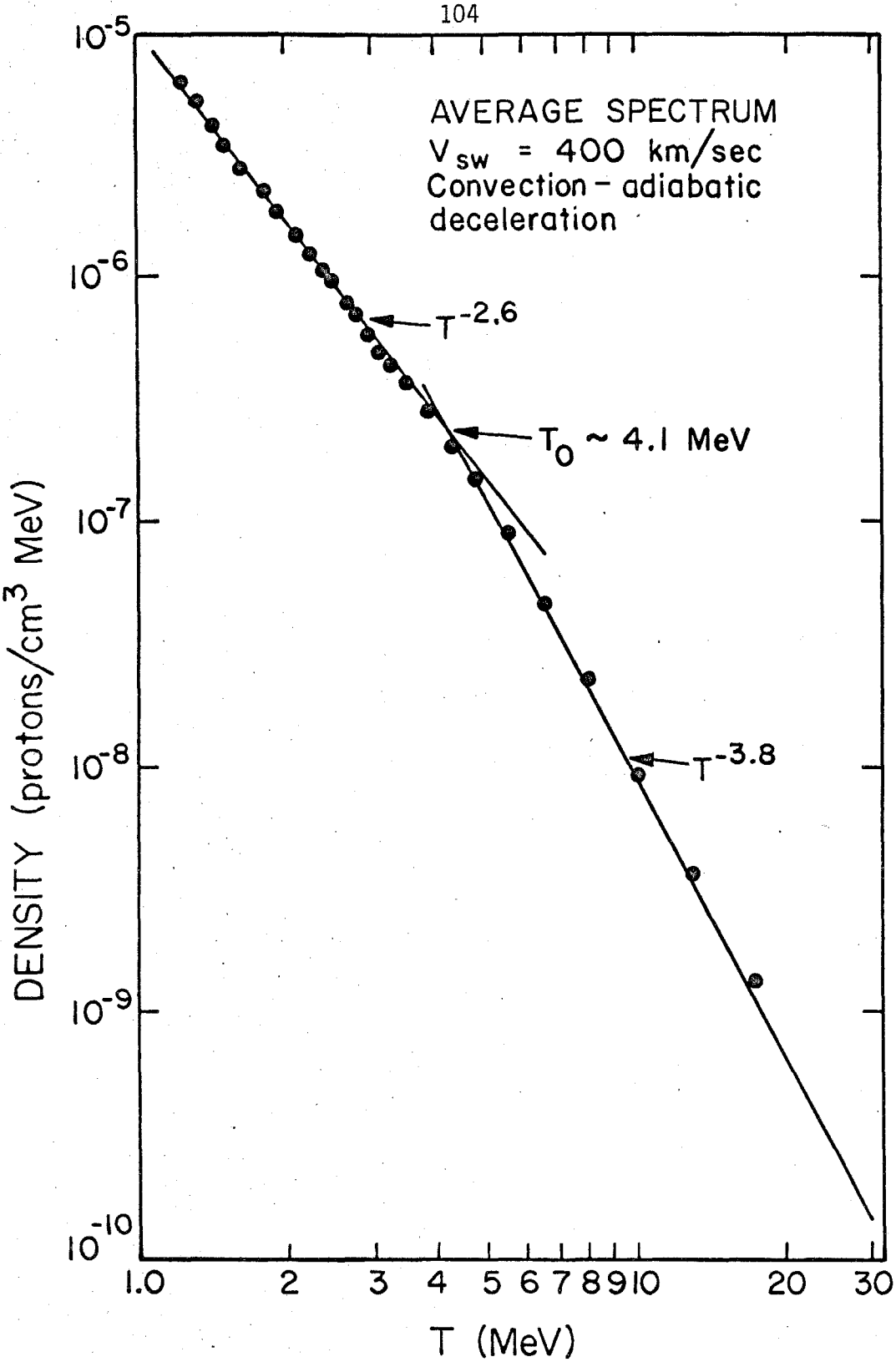
AVERAGE SPECTRUM
V_{sw} = 400 km/sec
Convection – adiabatic deceleration
$T^{-2.6}$
$T_0 \sim 4.1$ MeV
$T^{-3.8}$
DENSITY (protons/cm^3 MeV)
10^{-5}
10^{-6}
10^{-7}
10^{-8}
10^{-9}
10^{-10}
1.0
2
3
4
5
6
7
8
9
10
20
30
T (MeV)

Figure VI-6

Intersection energy for the two power law functions given by equation 6-34 that are fit to each of the 72 absolute differential density spectra observed during the decay of the 7 June 1969 solar flare vs. universal time. The solid line is an exponential fit to these data. The dashed line is the expected variation for uniform adiabatic deceleration. t_0 is 0227 UT on day 161.

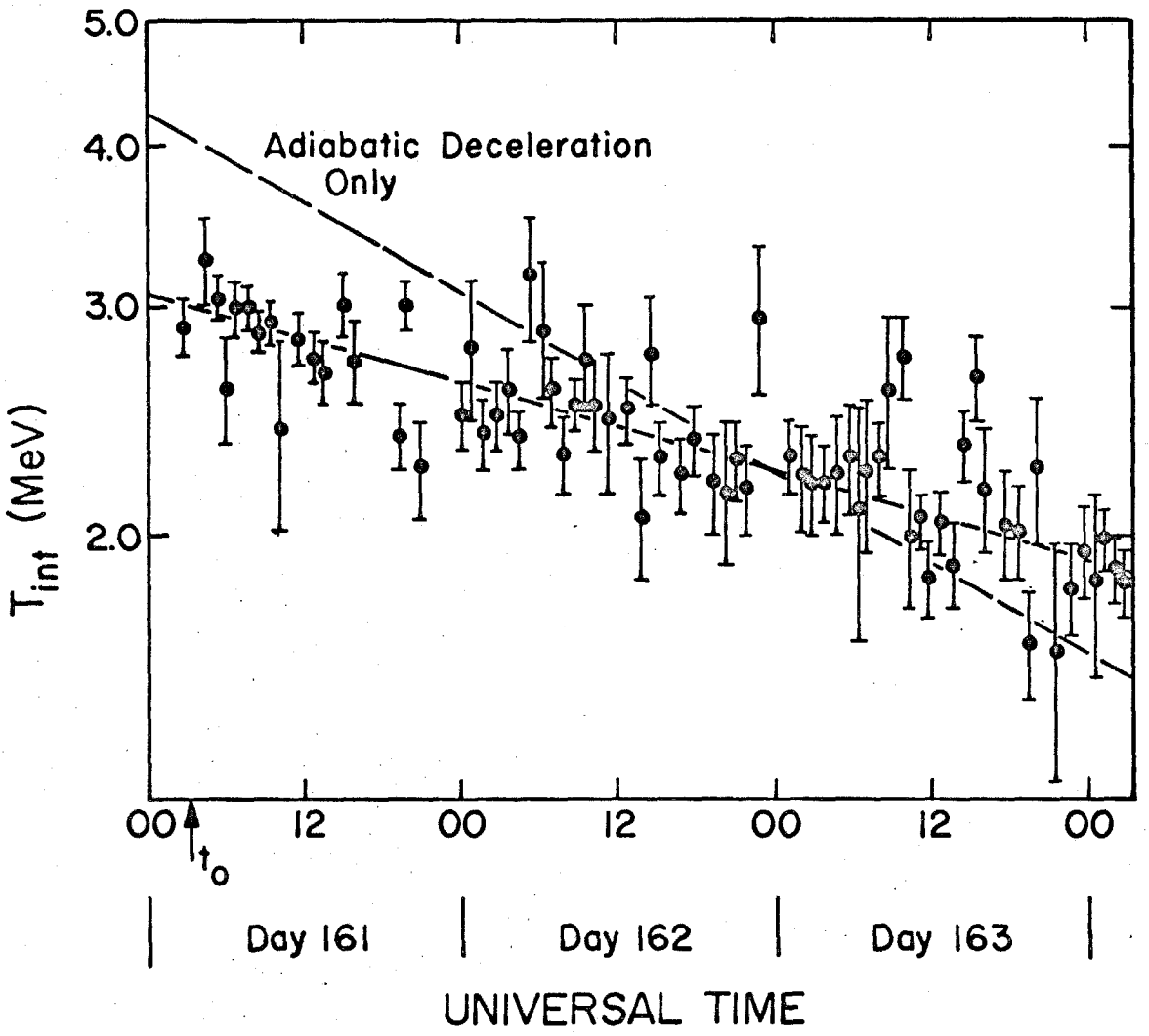
5.0
4.0
3.0
2.0
Adiabatic Deceleration
Only
T_{int} (MeV)
00
12
00
12
00
12
00
t_o
Day 161
Day 162
Day 163
UNIVERSAL TIME

expected rate of change of energy as given by equation 6-9 is exponential with time, we have plotted log (T_{int}) vs. time. The uncertainties in the data points are the uncertainties which result from the least squares fits of the data to the power laws given by equation 6-34. The curve shown in figure VI-6 is the result of fitting an exponential function of time to the data.

$$T(t) = T_0 \exp(-t/\tau_E) \qquad (6\text{-}35a)$$

Using a linear regression technique (33), we fit the function

$$\ln(T) = A + Bt \qquad (6\text{-}35b)$$

to the data plotted. The results of this fit are

$$A = 1.11 \pm 0.01$$

$$B = 0.0062 \pm 0.0003$$

with a linear correlation coefficient of 0.88 and a goodness of fit parameter $\chi^2 = 1.2$. This gives

$$\tau_E = 161 \pm 7 \text{ hours}$$

$$T_0 = 3.02 \pm 0.03 \text{ MeV}$$

We can compare the value of τ_E so obtained with the expected value assuming that the rate of change of energy is given

by equation 6-9

$$\tau_E = \frac{3r}{4\ V_{sw}} \qquad (6\text{-}36)$$

Using the observed value of V_{sw} = 400 ±20 km/sec, we get

$$\tau_E = 78 \pm 4 \text{ hours}$$

This is clearly not in agreement with the fitted value of 161 hours. Also, the intersection energy at t_0 for this fit differs significantly from that obtained from the average spectrum (figure VI-5). That is,

$$T_0(\text{fit}) = 3.02 \pm 0.03 \text{ MeV}$$

$$T_0(\text{average}) = 4.1 \pm 0.8 \text{ MeV})$$

3) Convection-Energy Change (CEC) Model

We interpret the inconsistencies encountered in fitting data to the CAD model as an indication of the existence of a competing acceleration process in the solar wind which has the same functional form as the adiabatic deceleration process. A possible process is Fermi acceleration (2, 34, 48). We will therefore consider a generalization of the CAD model which includes the effects of such acceleration processes. We will refer

to this as the convection-energy change model (CEC), and we proceed as follows:

Let the rate of change of energy be specified by a single parameter so that

$$\frac{dT}{dt} = -T/\tau_E \tag{6-37}$$

then use equation 6-2 to obtain

$$\frac{\partial n}{\partial t} = \nabla\cdot(\underline{\underline{\kappa}}\nabla n) - \nabla\cdot(n\vec{V}_{sw}) + \frac{1}{\tau_E}\frac{\partial}{\partial T}(nT) \tag{6-38}$$

Assuming, as was done for the CAD model, that diffusion effects are negligible, the solar wind is radial and constant, and that $\frac{\partial n}{\partial r}$ is small, equation 6-38 gives

$$\frac{\partial n}{\partial t} = -\frac{2\,V_{sw}}{r}n + \frac{1}{\tau_E}\frac{\partial}{\partial T}(nT) \tag{6-39}$$

Letting τ_C be the convective time constant, then

$$\frac{\partial n}{\partial t} = \frac{-3n}{\tau_C} + \frac{1}{\tau_E}n + \frac{T}{\tau_E}\frac{\partial n}{\partial T} \tag{6-40}$$

where

$$\tau_C = \frac{3r}{2\,V_{sw}}$$

To solve this equation, use the solution for the CAD model as a special case of this more general model and therefore try

$$n(t,T) = \exp\left[-(t-t_0)/\tau_1\right] n\left(t_0, T_0 = T \exp\left[(t-t_0)/\tau_2\right]\right) \tag{6-41}$$

This is a solution to the differential equation 6-40 provided that

$$\frac{1}{\tau_1} = \frac{3}{\tau_C} - \frac{1}{\tau_E} \tag{6-42a}$$

and

$$\frac{1}{\tau_2} = \frac{1}{\tau_E} \tag{6-42b}$$

It is interesting to note that in the case where only adiabatic deceleration is considered, then

$$\tau_E = \frac{1}{2}\tau_C \tag{6-43}$$

and using equations 6-42, we find

$$\tau_1 = \tau_C \tag{6-44a}$$

$$\tau_2 = \tau_E = \frac{1}{2}\tau_C \tag{6-44b}$$

which gives the solution obtained by Forman (50), i.e., the CAD model.

The solution, equation 6-41, can be used to fit the observed data by varying both τ_1 and τ_2. To do this, we invert equation 6-41 giving

$$n_{MB}\left(t_0,T_0 = T \exp\left[(t-t_0)/\tau_2\right]\right) = \exp\left[(t-t_0)/\tau_1\right] n(t,T)\, a(t) \qquad (6\text{-}45)$$

and use the same map-back procedure as was used for the CAD model, except that both time constants are varied. Examples of the mappings obtained in this manner are shown in figures VI-7a, -b and -c. The goodness of fit parameter χ^2 is plotted vs. τ_1 and τ_2 in figure VI-8. The values for minimum χ^2 ($\chi^2 = 1.7$) are

$$\tau_1 = 32 \pm 3 \text{ hours}$$

$$\tau_2 = 210 \pm 20 \text{ hours}$$

The average spectrum for these values of τ_1 and τ_2 is shown in figure VI-9 and from this spectrum, the power law functions used to fit all of the absolute spectra are

$$n_{abs}(T) = n_0 T^{-2.6} \qquad T < 2.5 \text{ MeV} \qquad (6\text{-}46a)$$

$$n_{abs}(T) = n_0 T^{-4.2} \qquad T > 4.0 \text{ MeV} \qquad (6\text{-}46b)$$

As was done for the CAD model, the spectra observed are fit to these power law functions and in figure VI-10 the

Figure VI-7a, b, c

Results from mapping 72 adjusted differential density spectra for protons during the decay phases of the 7 June 1969 solar flare event to time 0227 UT on day 161. The map-back equation is 6-45 with τ_1 = 30 hours, τ_2 = 210 hours (a)

τ_1 = 32 hours, τ_2 = 210 hours (b)

τ_1 = 34 hours, τ_2 = 210 hours (c)

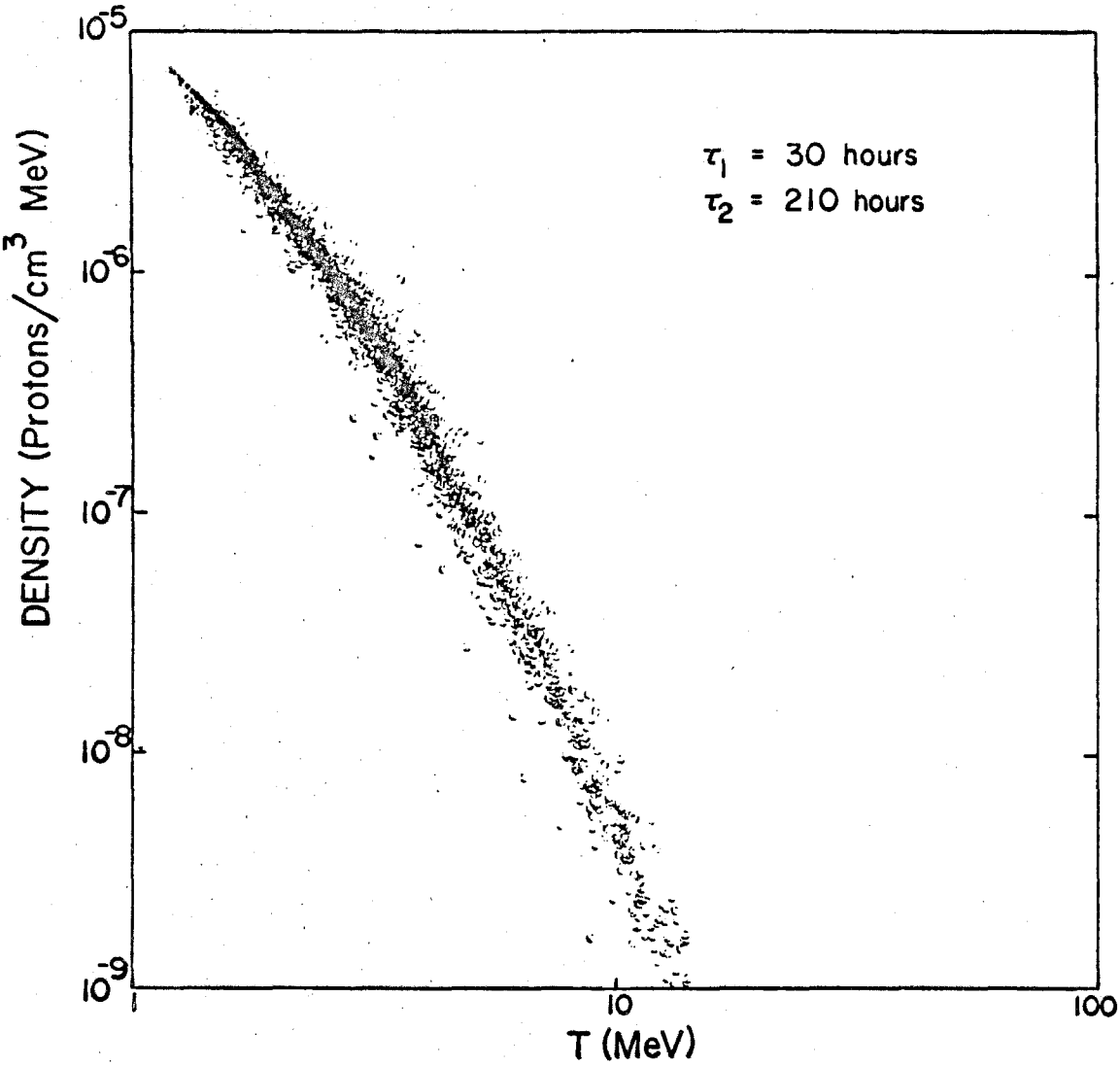
10^{-5}
10^{-6}
10^{-7}
10^{-8}
10^{-9}
DENSITY (Protons/cm^3 MeV)
τ_1 = 30 hours
τ_2 = 210 hours
1
10
100
T (MeV)

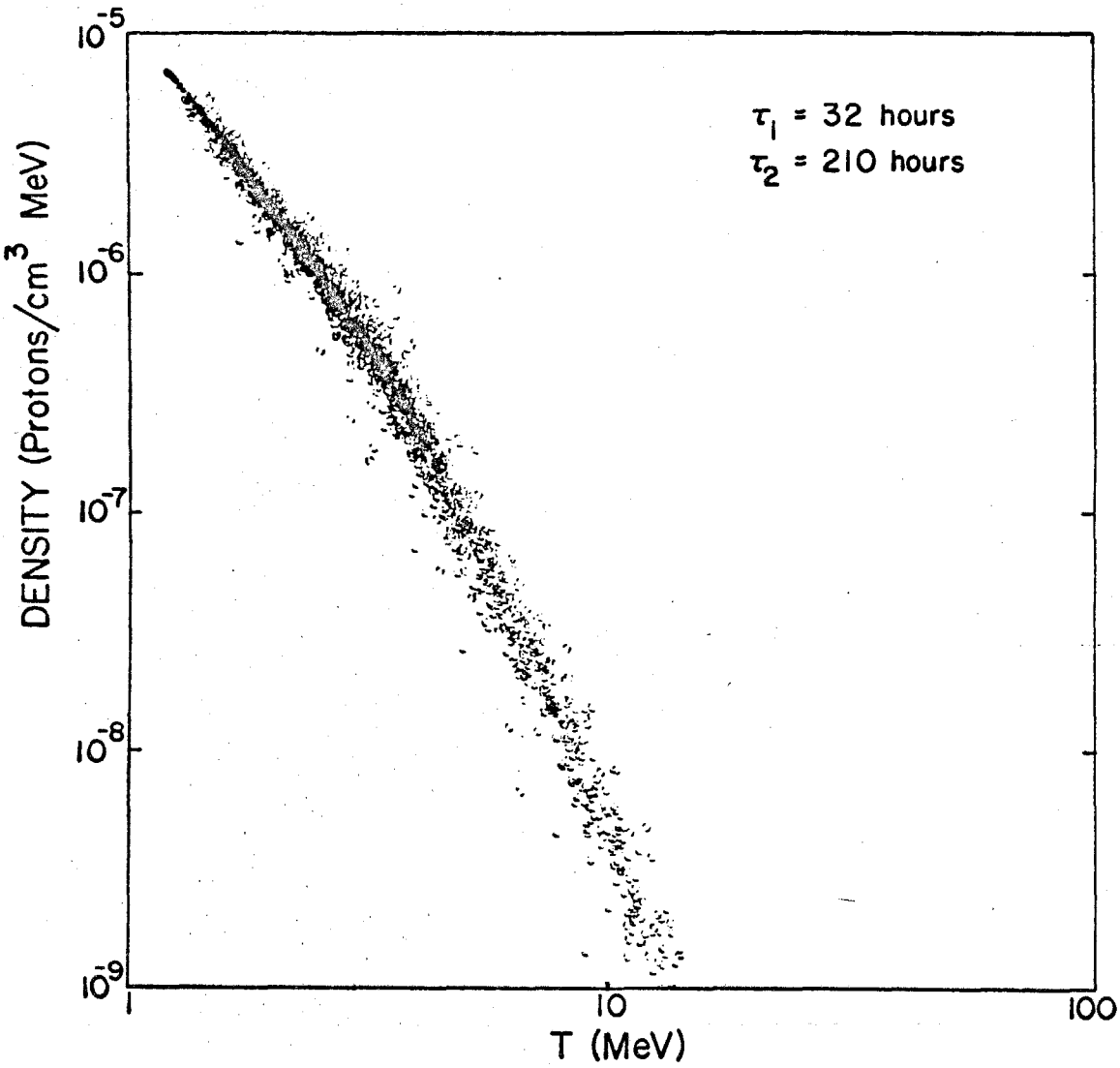
10^{-5}
10^{-6}
10^{-7}
10^{-8}
10^{-9}
DENSITY (Protons/cm^3 MeV)
τ_1 = 32 hours
τ_2 = 210 hours
1
10
100
T (MeV)

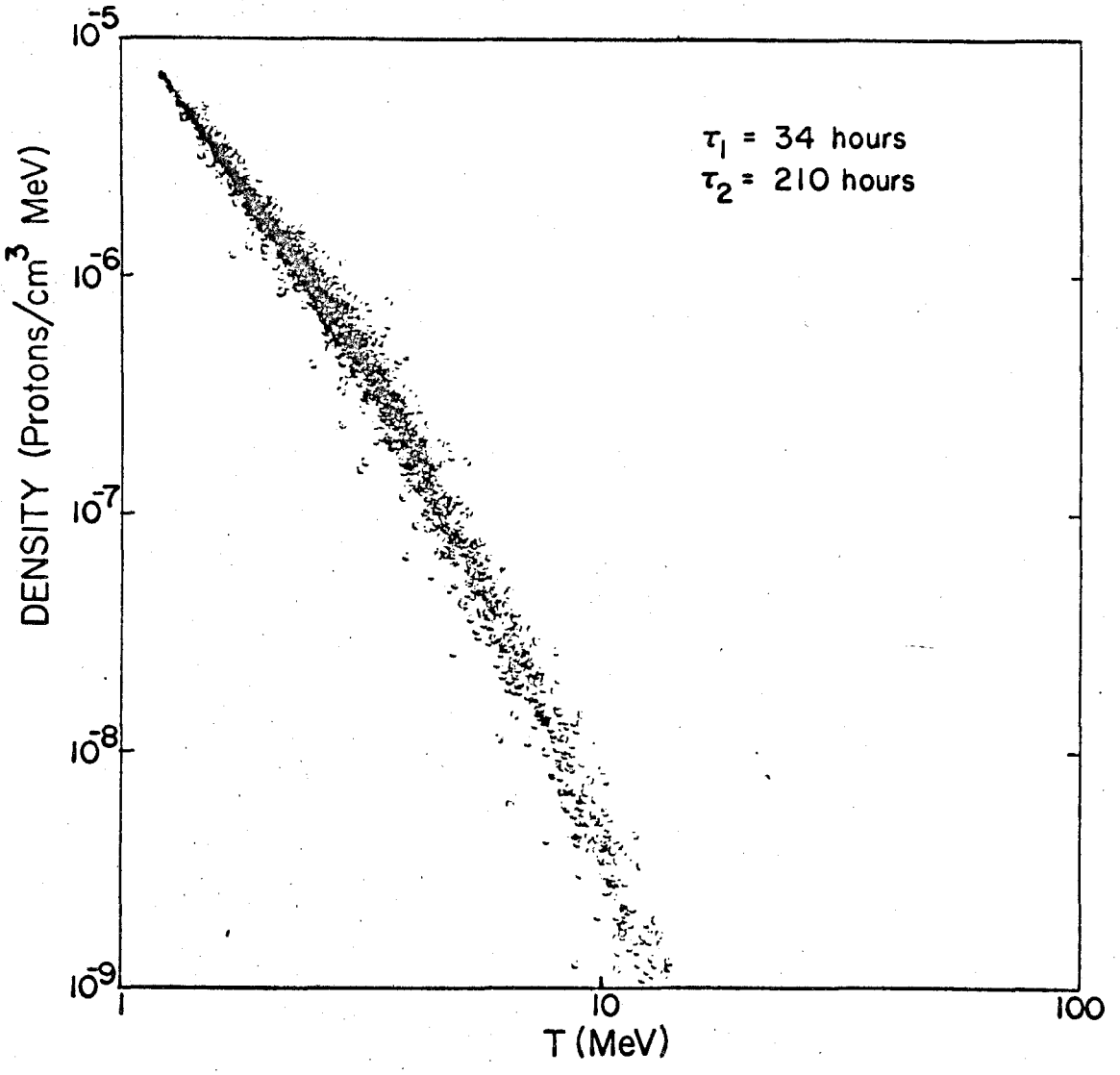
10^{-5}
10^{-6}
10^{-7}
10^{-8}
10^{-9}
DENSITY (Protons/cm^3 MeV)
τ_1 = 34 hours
τ_2 = 210 hours
1
10
100
T (MeV)

Figure VI-8

Goodness of fit parameter χ^2 vs. τ_1 and τ_2 for the map-back procedure given by equation 6-45.

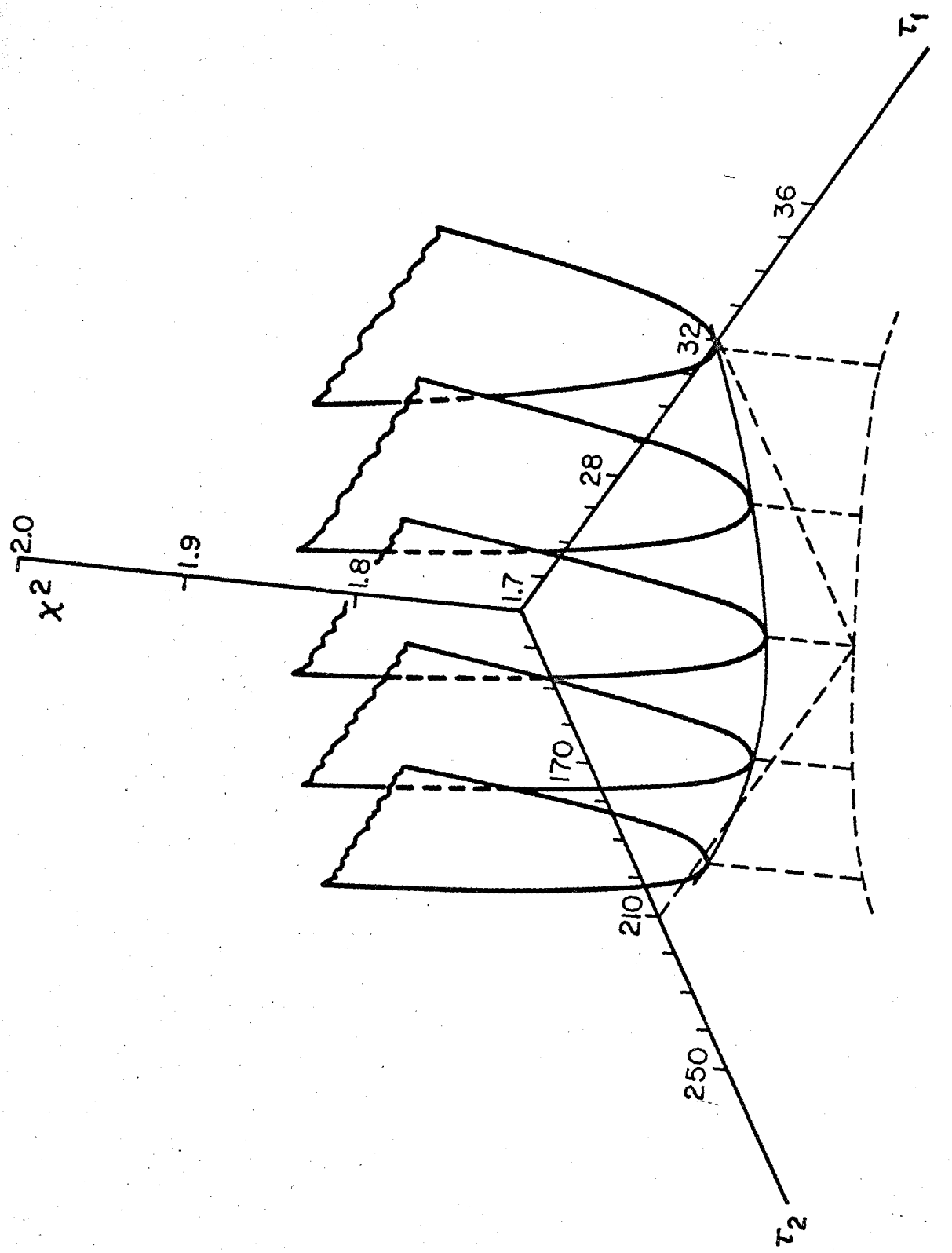
τ_1
36
32
28
χ^2
2.0
1.9
1.8
1.7
170
210
250
τ_2

Figure VI-9

Average differential density spectrum for protons for the map-back shown in figure VI-7b. T_0 is the intersection energy for the two power laws in kinetic energy which are fit to the average spectrum.

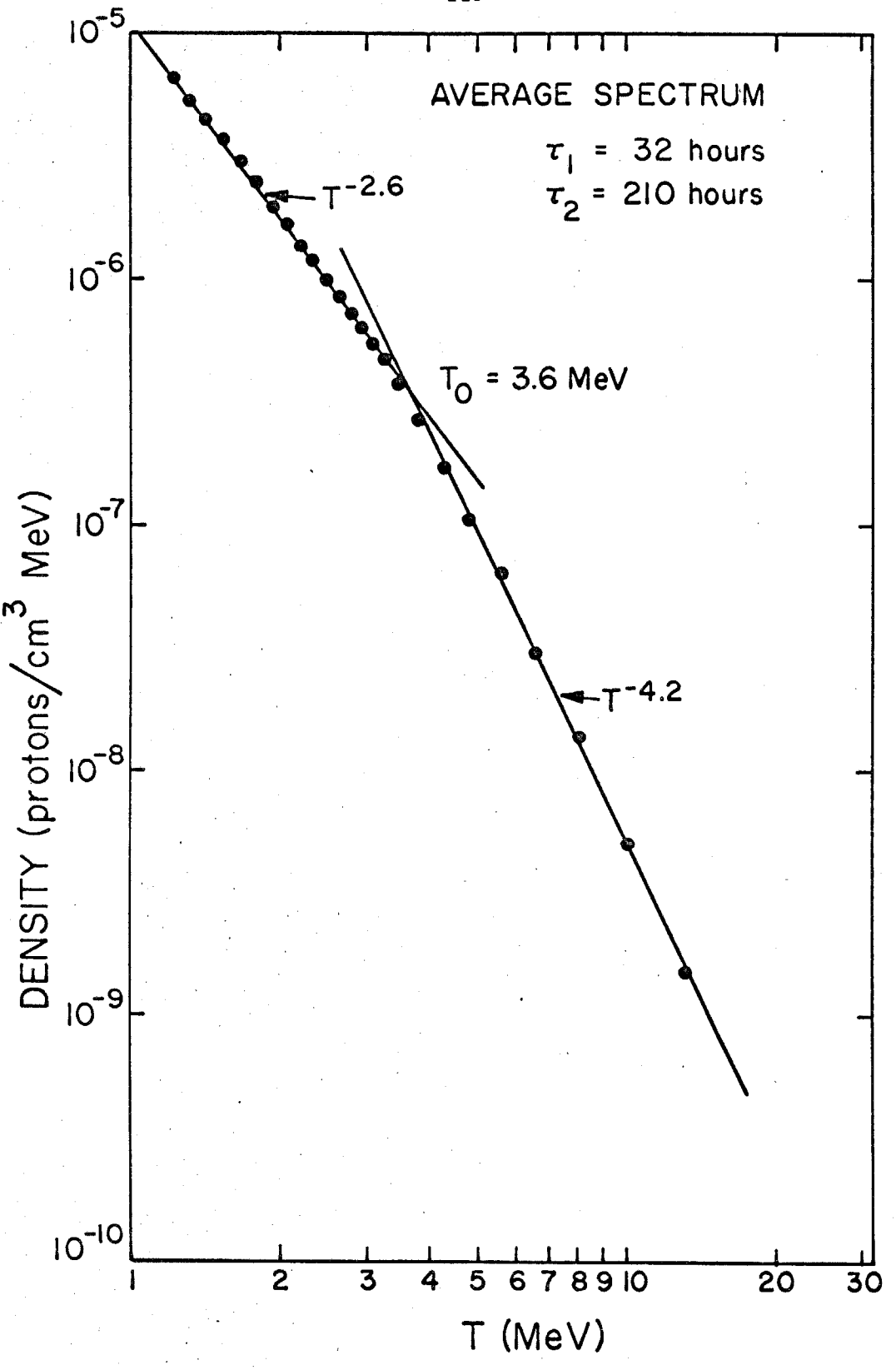
AVERAGE SPECTRUM
τ_1 = 32 hours
τ_2 = 210 hours
$T^{-2.6}$
T_0 = 3.6 MeV
$T^{-4.2}$
DENSITY (protons/cm^3 MeV)
10^{-5}
10^{-6}
10^{-7}
10^{-8}
10^{-9}
10^{-10}
1
2
3
4
5
6
7
8
9
10
20
30
T (MeV)

Figure VI-10

Intersection energy for the two power law functions given by equation 6-46 that are fit to each of the 72 absolute differential density spectra observed during the decay of the 7 June 1969 solar flare vs. universal time. The solid line is an exponential fit to these data. The dashed line is the expected variation for uniform adiabatic deceleration. t_0 is 0227 UT on day 161.

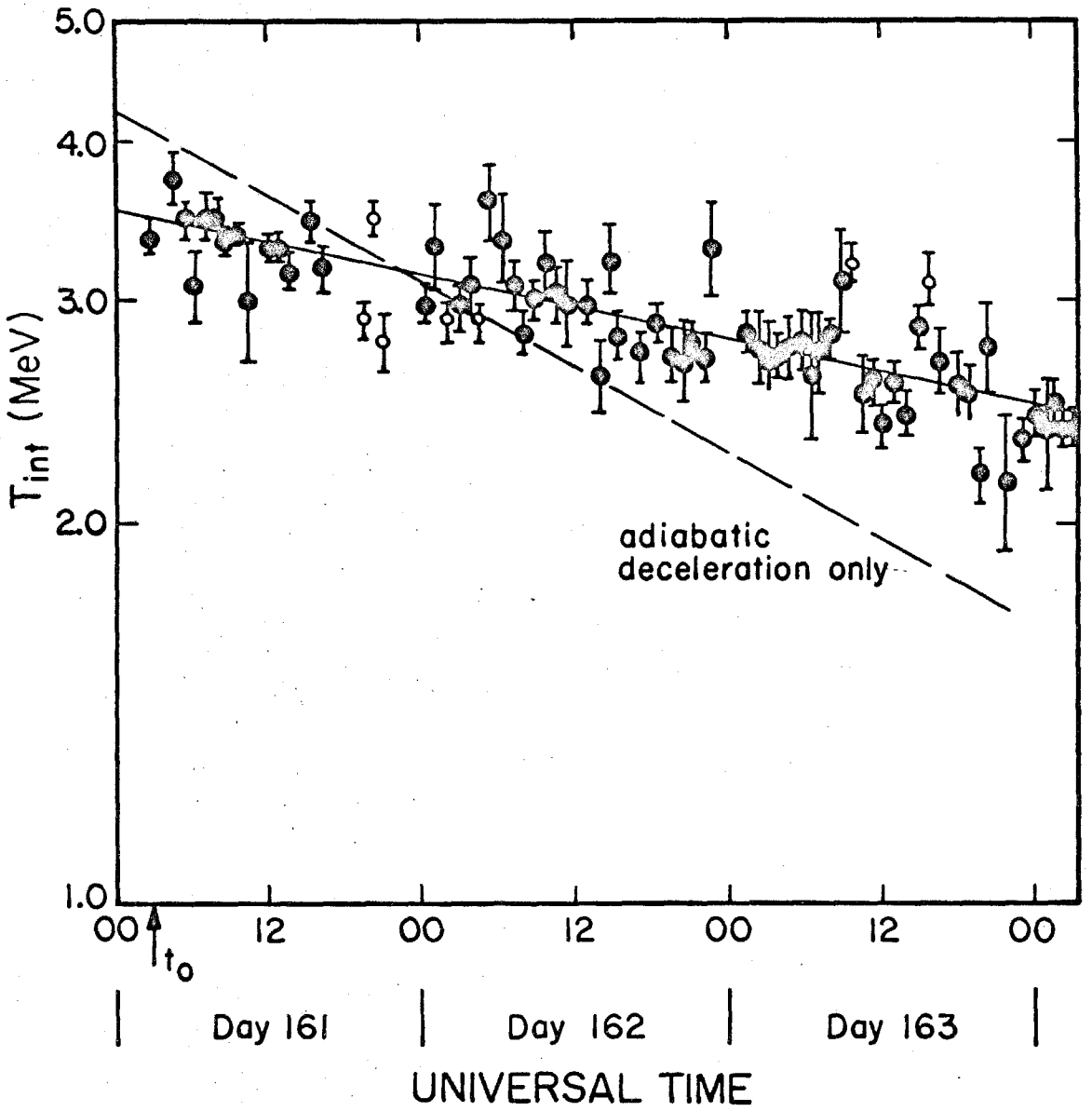
5.0
4.0
3.0
2.0
1.0
T_{int} (MeV)
adiabatic
deceleration only
00
12
00
12
00
12
00
t_o
Day 161
Day 162
Day 163
UNIVERSAL TIME

intersection energy vs. time is plotted. The data are fit to equation 6-37 using the linear regression technique discussed in section VI B2 resulting in

$$A = 1.25 \pm 0.01$$

$$B = 0.0048 \pm 0.0002$$

or

$$\tau_E = 207 \pm 7 \text{ hours}$$

$$T_0 = 3.48 \pm 0.03 \text{ MeV}$$

with a linear correlation coefficient of 0.88 and $\chi^2 = 1.1$. Notice that this value of τ_E agrees well with the value for τ_2 obtained from the mapping. Also, the value of T_0 from this fit agrees with the value obtained from the average spectrum. That is,

$$T_0(\text{fit}) = 3.48 \pm 0.03 \text{ MeV}$$

$$T_0(\text{average}) = 3.6 \pm 0.5 \text{ MeV}$$

Using the value $\tau_2 = 210 \pm 20$ hours, and the solar wind velocity of 400 ±20 km/sec, τ_1 can be calculated from equation 6-42a and compared with the value obtained from the mapping.

$$\frac{1}{\tau_1}\ (\text{calculated}) = (4.0 \pm 0.3) \times 10^{-6}\ \text{sec}^{-1}$$

$$\frac{1}{\tau_1}\ (\text{mapping}) = (8.7 \pm 0.8) \times 10^{-6}\ \text{sec}^{-1}$$

These values do not agree, indicating that the interpretation of τ_1 as due to uniform convection is incorrect.

4) Diffusion-Convection-Energy Change (DCEC) Model

One possible source for the disagreement between the observed and expected values for τ_1 is that the effects of diffusion are in fact not negligible. The observed decay is exponential, and we expect that the inclusion of diffusion will not affect the rate of change of energy. Therefore, we will include diffusion processes in the theoretical model by modifying the interpretation of τ_1 in equation 6-41. We expect that the inclusion of diffusive processes will result in faster decay of solar flare events by introducing an additional loss mechanism. Thus, we modify equation 6-42a to

$$\frac{1}{\tau_1} = \frac{3}{\tau_C} - \frac{1}{\tau_E} + \frac{1}{\tau_D} \qquad (6\text{-}47)$$

where τ_D gives the contribution of diffusive processes to the decay. With this form for τ_1 we can calculate the

value of τ_D necessary to get the calculated value of τ_1 to equal the value for τ_1 obtained from the mapping.

$$\frac{1}{\tau_D} = (4.7 \pm 0.9) \times 10^{-6} \text{ sec}^{-1}$$

If only diffusion were important, we know that the decay time constant would be given by equation 6-18. Although the transport equation 6-38 is non-linear, we will assume that within an order of magnitude the value for τ_D given by equation 6-18 is the correct form to be used in equation 6-47. Thus, using equation 6-18 and the value of τ_D which gives the right value for τ_1, we can find a value for $\kappa_{\parallel}$.

$$\kappa_{\parallel} \simeq (5.7 \pm 1.1) \times 10^{20} \text{ cm}^2/\text{sec}$$

This is the value of $\kappa_{\parallel}$ corresponding to a ~30 MeV proton if equation 6-7a is used. This would appear to indicate that the approximations used to estimate diffusive effects are not unreasonable.

5) Anisotropic Diffusion with a Boundary-Convection-Energy Change (ADBCEC) Model

We can conclude from the results of section VI B4, that the effects of diffusion in the propagation of 1-10 MeV protons are not negligible. Thus, it would be of interest

to consider a solution to the complete transport equation 6-38 even if only for special forms of the parameters $\underline{\underline{\kappa}}$ and τ_E. In appendix C, a solution to equation 6-38 is derived by modifying a solution given by Forman (55) to a similar equation. This solution predicts an exponential decay for solar flare fluxes if the differential density spectrum is a power law in kinetic energy. We will refer to this as the ADBCEC model. The significant result of the model for this discussion is equation C-23 which gives the exponential decay time constant for a power law differential density spectrum $n(T) = n_0 T^{-\gamma}$.

$$\tau_{decay} = \frac{4D}{\kappa_0 (j_{\eta,1})^2} \qquad (6\text{-}48)$$

where

$j_{\eta,1}$ = first root of the Bessel function $J_\eta(x)$

$\kappa_0 = \kappa_{\parallel}/r$

D = boundary radius

$\eta = 2\sqrt{(1-V/2\kappa_0)^2 + 2\ CV/\kappa_0}$

$C = 1 + (\gamma-1)/2\ V\tau_0$

$\tau_0 = \tau_E/r$

We will consider the application of this model to our data in the following section, where the decay time constants calculated and observed are discussed.

C) Model Summary and Analysis

We have considered several models for describing the propagation of low energy (1-10 MeV) solar flare protons in interplanetary space. These models can be used to predict the exponential decay time constants for the flux of particles observed near the earth during the decay phase of a flare. In table VI-II the equations for calculating these decay times and the calculated values for solar flare protons of ~1 MeV and ~10 MeV for the 7 June 1969 event are given.

In table VI-II the diffusion model has been treated differently from the other models listed in that we have used the observed decay times to calculate the model parameter $\kappa_{||}$ rather than calculating the decay time from the parameters as was done for the other models. We have done this to emphasize the fact that the assumption of a diffusion dominated decay is inconsistent with the approximations made in obtaining the diffusion transport equation 6-14.

The apparent agreement of the observed decay times with those calculated for the CAD model does not imply that this model is applicable to the 7 June 1969 solar flare. As was discussed in section VI B2, the CAD model does not predict the observed rate of change of energy for protons in the energy range 1-10 MeV. On the other hand the CEC

TABLE VI-II

SUMMARY OF PROPAGATION MODELS

Model	Decay Time Constant for a power law spectrum = $n_0 T^{-\gamma}$	Parameters	~1 MeV τ_{decay} (hrs)	~10 MeV τ_{decay} (hrs)
Diffusion*	$\frac{1}{\tau_{decay}} = \frac{\pi^2 \kappa_{\parallel}}{D^2}$	$\kappa_{\parallel}$ (1 MeV) = 1.4 x 10^{21} cm^2/sec $\kappa_{\parallel}$ (10 MeV) = 1.8 x 10^{21} cm^2/sec D = 2.3 AU	23.1	18.6
CAD	$\frac{1}{\tau_{decay}} = \frac{4\ V_{sw}(\gamma + \frac{1}{2})}{3r}$	r = 1 AU V_{sw} = 400 km/sec γ(1 MeV) = 2.6 γ(10 MeV) = 3.8	25.2	18.2
CEC	$\frac{1}{\tau_{decay}} = \frac{2\ V_{sw}}{r} + \frac{\gamma - 1}{\tau_E}$	r = 1 AU V_{sw} = 400 km/sec τ_E = 210 hours γ(1 MeV) = 2.6 γ(10 MeV) = 4.2	37.3	29.0

*For diffusion model the observed time constants are used to calculate $\kappa_{\parallel}$ to illustrate required values for this parameter.

TABLE VI-II (continued)

SUMMARY OF PROPAGATION MODELS

Model	Decay Time Constant for a power law spectrum = $n_0 T^{-\gamma}$	Parameters	~1 MeV τ_{decay}	~10 MeV τ_{decay}
DCEC	$\frac{1}{\tau_{decay}} = \frac{2 V_{sw}}{r} + \frac{\gamma-1}{\tau_E} + \frac{\pi^2 \kappa_{\parallel}}{D^2}$	same as CEC $\kappa_{\parallel} = 5.7 \times 10^{20} cm^2/sec$ D = 2.3 AU	22.8	19.5
ADBCEC	$\frac{1}{\tau_{decay}} = \frac{\kappa_0 (j_{\eta,1})^2}{4D}$	same as DCEC except		
		$\kappa_{\parallel} = 3.0 \times 10^{20} cm^2/sec$	27.0	22.6
		$\kappa_{\parallel} = 4.0 \times 10^{20} cm^2/sec$	24.1	20.3
		$\kappa_{\parallel} = 5.0 \times 10^{20} cm^2/sec$	21.7	18.5

model which correctly predicts the rate of change of energy gives decay times which are considerably longer than those observed. This is consistent with the discussion in section VI B3 where it was argued that the inclusion of diffusion in the CEC model would result in a faster decay of particles. As is apparent from the table, the decay time constants calculated for the DCEC model are shorter than those calculated for the CEC model. Also, these values of these decay times are in reasonable agreement with the observed decay times.

Calculated decay times using the ADBCEC model are listed in table VI-II for several values of $\kappa_{\parallel}$. As can be seen, the best agreement with the observed values for the decay times is for $\kappa_{\parallel}$ approximately 4×10^{20} to 5×10^{20} cm^2/sec. The difference between this value for $\kappa_{\parallel}$ and that used in the DCEC model is the result of the different approximations used for including the effects of diffusion. The approximate agreement of those values for $\kappa_{\parallel}$ indicates that the heuristic modification of the CEC model used to obtain the DCEC model is not unreasonable.

In table VI-II we have listed the decay time constants for a two power law fit to the spectrum of the 7 June 1969 solar flare. The observed spectrum for this flare is only approximately fit by these two power law

functions. There is in fact a continuous transition from one of these functions to the other. In figure VI-11 we have plotted the average power law index $\langle\gamma(T)\rangle$ which results from fitting the average spectrum obtained from the map-back procedure (described in section VI B3) to a power law function from T to T', where $T' = T \exp(\Delta t/\tau_E)$, $\Delta t = 72$ hours and $\tau_E = 210$ hours. This energy interval was chosen because the average spectrum was constructed from data spanning 72 hours of the decay. The lines shown in this figure are for the power laws fit to the average spectrum in figure VI-9.

The average power law indicies shown in figure VI-11 are used in calculating the decay time constants as a function of kinetic energy for the CEC model and the ADBCEC model. These decay times are plotted in figure VI-12 along with the observed decay times derived from exponential fits to the adjusted fluxes (see chapter V). Also shown in the figure is the difference in $1/\tau_{decay}$ between the observed values and those calculated from the CEC model.

From figure VI-11, which shows the variation of $\langle\gamma(T)\rangle$ with energy, and the plot of $1/\tau_{decay}$ for the CEC model shown in figure VI-12, it is clear that the energy dependence of the decay time constant is related to the spectrum. This

Figure VI-11

Average power law index $\langle\gamma(T)\rangle$ vs. kinetic energy T for the average differential density spectrum shown in figure VI-9.

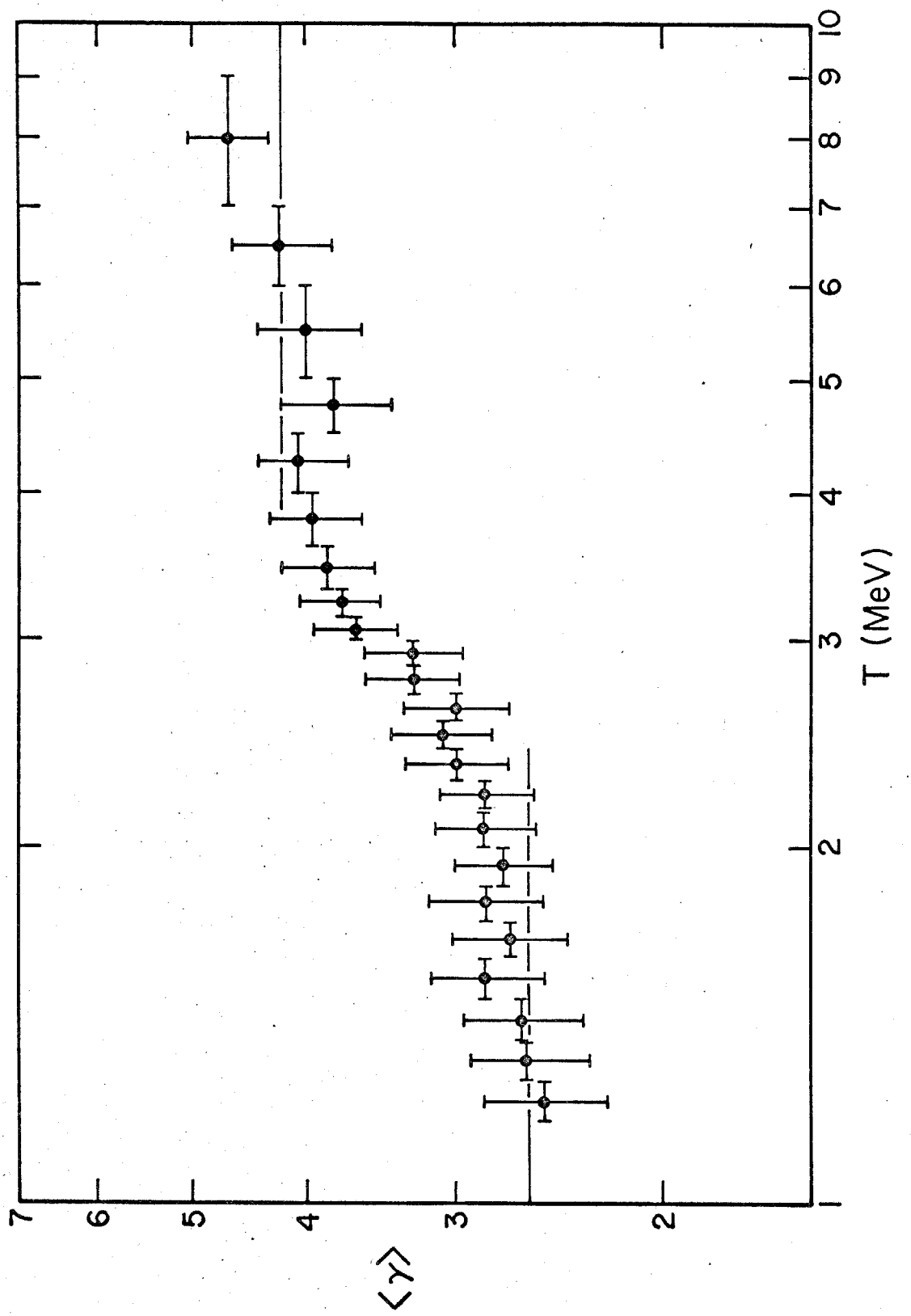
7
6
5
4
3
2
⟨γ⟩
1
2
3
4
5
6
7
8
9
10
T (MeV)

dependence is due to the energy change term in the transport equation 6-39. Thus, the strong correlation in the energy dependence of $<\gamma(T)>$ and $1/\tau_{decay}$ is further evidence for the importance of energy change processes in the propagation of 1-10 MeV protons.

The difference between the observed decay times and that calculated from the CEC model is essentially constant over the energy interval 1-10 MeV. This difference is attributed to the effects of diffusion as discussed in section VI B4. However, in that discussion we assumed that τ_D was independent of energy. In this case we have shown that this is indeed a correct assumption.

Using the form for the diffusion decay time constant given by equation 6-18, the value of the diffusion coefficient $\kappa_{\parallel}$ which is consistent with the difference between the observed decay times and those calculated from the CEC model is

$$\kappa_{\parallel} \simeq (6 \pm 1) \times 10^{20} \text{ cm}^2/\text{sec}$$

where the boundary distance D in equation 6-18 is taken to be 2.3 AU. This is the same value for $\kappa_{\parallel}$ that was obtained in section VI B4.

Using the average power law indicies shown in figure VI-11, the decay time constant can also be calculated from

the results of the ADBCEC model. The solid curves in figure VI-12 are the results of this calculation for several values of $\kappa_{\parallel}$. As for the CEC model, the energy dependence of $1/\tau_{decay}$ is contained in the variation of $\langle\gamma(T)\rangle$ with energy since in this model $\kappa_{\parallel}$ is assumed to be constant. There is good agreement of the decay times calculated using the ADBCEC model with $\kappa_{\parallel} \simeq 4 \times 10^{20}$ cm^2/sec and the observed time constants.

The values of $\kappa_{\parallel}$ obtained from the DCEC model (based upon the difference between the predicted decay times from the CEC model and the observed decay time) and the ADBCEC model are essentially the same. This value for $\kappa_{\parallel}$ is in reasonable agreement with the value given by equation 6-8 for a 10 MeV proton. However, the observed energy dependence of $\kappa_{\parallel}$ is not consistent with this equation. The energy dependence of $\kappa_{\parallel}$ as given in equation 6-8 is based on an argument by Jokipii (45) that the mean free path λ for low energy protons in a turbulent magnetic field becomes constant and equal to the correlation length of the magnetic field fluctuations. This gives the form for equation 6-8 since

$$\kappa_{\parallel} \alpha \beta\lambda. \qquad (6\text{-}49)$$

The results from the analysis of the 7 June 1969 flare indicate that for this event, $\kappa_{\parallel}$ is independent of energy

Figure VI-12

Exponential decay time constants vs. incident kinetic energy. The observed decay times are indicated by the filled circles. The uncertainties in these times are less than or equal to the size of the circles. The decay times calculated from the CEC model using the equation in table VI-II are indicated by the "x"'s. The difference in these decay times is shown by the open circles. The solid lines are calculated according to the ADBCEC model from equation 6-48 where the parameter κ_0 used is given by $r\kappa_0 = \kappa_{\parallel}' \times 10^{20}$ cm^2/sec and r = 1 AU.

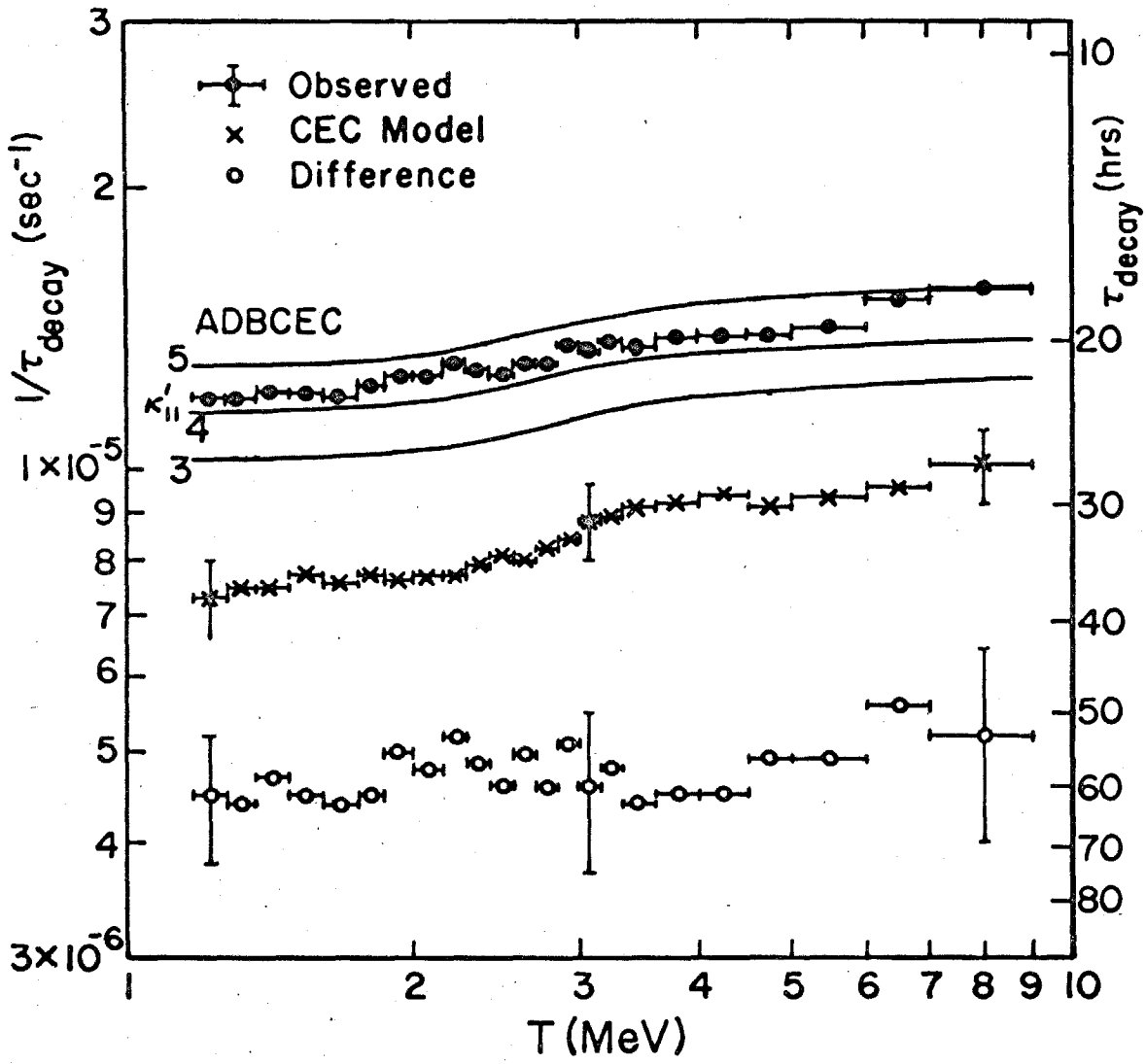
Observed
CEC Model
Difference
ADBCEC
κ'_{11}
5
4
3
$1/\tau_{decay}$ (sec^{-1})
τ_{decay} (hrs)
1×10^{-5}
9
8
7
6
5
4
3×10^{-6}
3
2
10
20
30
40
50
60
70
80
1
2
3
4
5
6
7
8
9
10
T (MeV)

(or β) for 1-10 MeV protons. Thus we conclude that the above theoretical agruement may not be appropriate.

There is little other observational evidence for the energy dependence of $\kappa_{\parallel}$ at these energies. A more complete set of data for several solar flare events and the interplanetary magnetic field are necessary to test the general importance of diffusion, convection and energy change processes in the propagation of solar flare particles.

VII. CONCLUSIONS

The various theoretical models considered in this thesis for the propagation of solar flare particles in the interplanetary medium are summarized in table VII-I. We have compared the observations of 1-10 MeV solar flare protons made with an experiment on board OGO-VI for the 7 June 1969 event with the predictions of these models.

As discussed in section VI B1, the assumption of a diffusion dominated decay is inconsistent with the approximations which were made in obtaining the diffusion transport equation 6-14. Also the observation of energy change processes indicates that the diffusion model is not sufficient for describing the propagation of these low energy particles.

Although the convection-adiabatic deceleration (CAD) model predicts the observed exponential decay time constants, we have shown in section VI B2 that the evolution of the observed density spectrum with time is not predicted by this model. Therefore, we conclude that the agreement of the predicted and observed time constants is fortuitous. By generalizing the CAD model we have constructed a model (DCEC) which correctly predicts the time behavior of the observed spectrum. This has required a

TABLE VII-I

PROPAGATION MODELS

Model	Assumptions
Diffusion	Effects of convection and energy change are neglected $\frac{\partial n}{\partial t} = \nabla \cdot (\underline{\underline{\kappa}} \nabla n)$
CAD	Convection and uniform adiabatic deceleration with no diffusion $\frac{\partial n}{\partial t} = -\frac{2 V_{sw} n}{r} + \frac{2}{3} \frac{V_{sw}}{r} \frac{\partial}{\partial T} (n \alpha T)$
CEC	Same as CAD model but energy loss is given by an exponential form $\frac{1}{T} \frac{dT}{dt} = -\frac{1}{\tau_E}$ $\frac{\partial n}{\partial t} = \frac{2 V_{sw} n}{r} + \frac{1}{\tau_E} \frac{\partial}{\partial T} (nT)$
DCEC	Heuristic modification of CEC model to include diffusion
ADBCEC	Specific solution to complete transport with all terms included $\frac{\partial n}{\partial t} = \nabla \cdot (\underline{\underline{\kappa}} \nabla n) - \nabla \cdot (n \vec{V}_{sw}) + \frac{1}{\tau_E} \frac{\partial}{\partial T} (nT)$

more general form for the energy change process, and the inclusion of diffusion. We have accomplished this in an approximate manner by modifying the interpretation of the parameters of the convection-energy change (CEC) model in which a generalized energy change process was incorporated. We also considered a solution to the complete transport equation for particular forms of the parameters $\underline{\underline{K}}$ and τ_E. This is the anisotropic diffusion with a boundary-convection-energy change (ADBCEC) model. These two methods for including the effects of diffusion result in approximately the same predictions for the decay time constants. As was already mentioned for the CEC model (section VI B3), the temporal evolution of the observed spectrum of the differential density is correctly predicted by the diffusion-convection-energy change (DCEC) model.

Thus, we conclude that in the energy range 1-10 MeV solar flare protons, from the 7 June 1969 event, propagating in interplanetary space are significantly affected by diffusion, convection and energy change processes. We find that in addition to uniform adiabatic deceleration in the expanding solar wind there is a competing acceleration process which reduces the net rate of change of energy. We also find that the observed exponential decay time constants of the particle fluxes are consistent with an energy

independent diffusion coefficient $\kappa_{\parallel}$ with a magnitude which is consistent with the value obtained from observations of the interplanetary magnetic field.

Appendix A

Low Energy (1-23 MeV) Proton Calibration of Range Telescope

The Range telescope of the flight unit (FU-1) for the California Institute of Technology Solar and Galactic Cosmic Ray Experiment on board OGO-VI was calibrated for protons from 1-23 MeV, using the Caltech Tandem Van de Graaff accelerator.

I) 1-12 MeV

In the energy range 1-12 MeV, the primary proton beam of the accelerator was scattered off a tantalum target. This coulomb scattering was used to reduce the beam intensity to a level compatible with the experiment (~1000 particles/sec). The scattered proton beam passed through a 4.5 mil Aluminum foil to produce range straggling, and was then momentum analyzed with a 24 inch magnetic spectrometer (56). The spectrometer was adjusted so that the energy spread of the analyzed beam at the experiment was not more than 1% of the incident proton energy. Figure A-1 illustrates the arrangement and setup for this calibration. Table A-I lists the data runs which were made with this configuration. Prior to these calibrations, the unit was exposed to a beam of alpha particles from a Th B (Pb^{212}) source. The data from that measurement were used to determine the thickness of the aluminized mylar window on the Range telescope.

II) 12-23 MeV

In the energy range 12-23 MeV, the reaction $B^{10}(He^3,p)\ C^{12}$ was used to produce protons of the required energy. The

Figure A-1

Setup for Tandem Van de Graaff accelerator calibration.

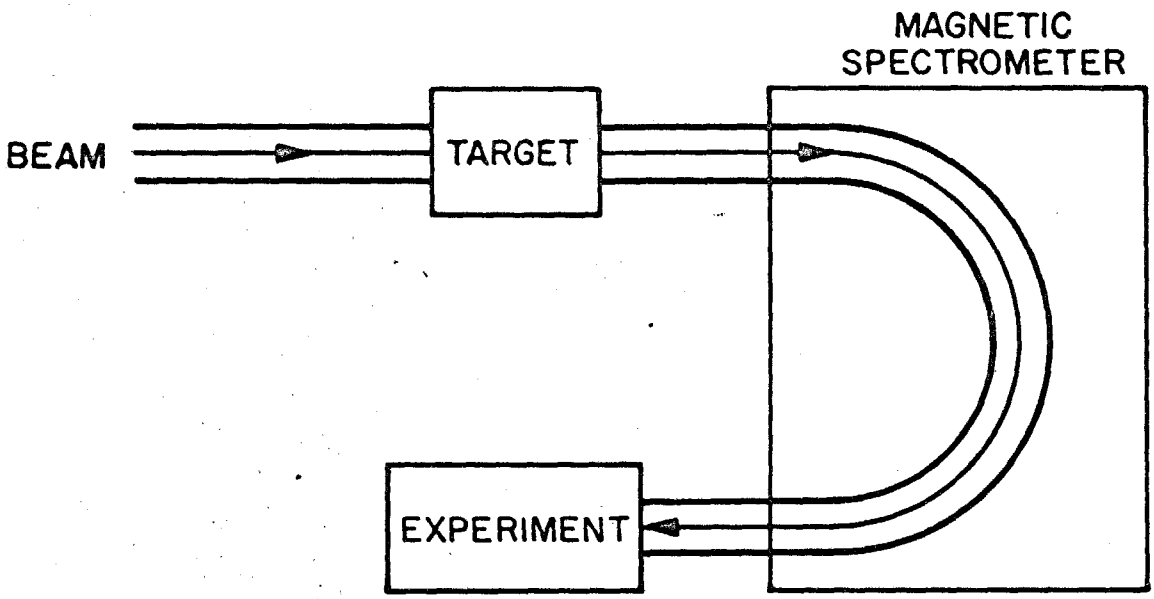
MAGNETIC
SPECTROMETER
BEAM
TARGET
EXPERIMENT

TABLE A-I

LOW ENERGY DATA RUNS

Run Number	Primary Beam Energy	Proton Energy
148	5.0 MeV	1.500 MeV
149	5.0	1.300
150	5.0	1.200
151	5.0	1.100
152	5.0	1.140
153	6.0	3.200
154	6.0	3.400
155	6.0	3.300
156	6.0	3.260
157	6.0	3.240
158	6.0	3.600
159	6.0	4.000
160	10.5	5.000
161	10.5	6.000
162	10.5	7.000
163	10.5	9.000
164	10.5	3.000
165	10.5	2.000
166	12.0	10.800
167	12.5	11.300

tantalum target was replaced with a boron target and the primary beam of the tandem accelerator was He^3. The resulting protons were momentum analyzed as in the low energy setup. Again the spectrometer was adjusted to give at least 1% energy resolution. The data runs in this energy range are summarized in table A-II.

III) Analysis

The data for each run were processed by computer to give the pulse height distribution in each detector (D1, D2, D3) and the correlated distributions in detectors D1 and D2 or D2 and D3. Examples of the reduced data are shown in figures A-2, -3 and -4. From this reduced data the electronic calibration of the pulse height analyzers is checked as follows:

1) Using the Th B data, the thickness of the mylar window is determined to be 2.32±3% mg/cm^2.
2) For protons which stop in D1, the energy which should be measured in this detector is calculated by correcting for the window, and compared with the observed energy loss. Figure A-5 summarizes this comparison. As can be seen, there is excellent agreement.
3) The resolution of the PHA is also checked. The full width at half maximum (FWHM) of energy loss

TABLE A-II

HIGH ENERGY DATA RUNS

Run Number	Primary Beam Energy	Proton Energy
168	12 MeV	22.94 MeV
169	12	22.70
170	12	22.50
171	12	22.30
172	12	20.50
173	12	19.00
174	12	19.00
175	12	22.50
176	12	22.70
177	12	22.90
178	12	17.80
179	12	18.20
180	12	17.40
181	12	12.75
182	12	12.50
183	12	13.00
184	12	13.20
185	12	12.64
186	12	12.86

Figure A-2

D1-PHA energy loss distribution in D1 for 1.500 MeV incident protons.

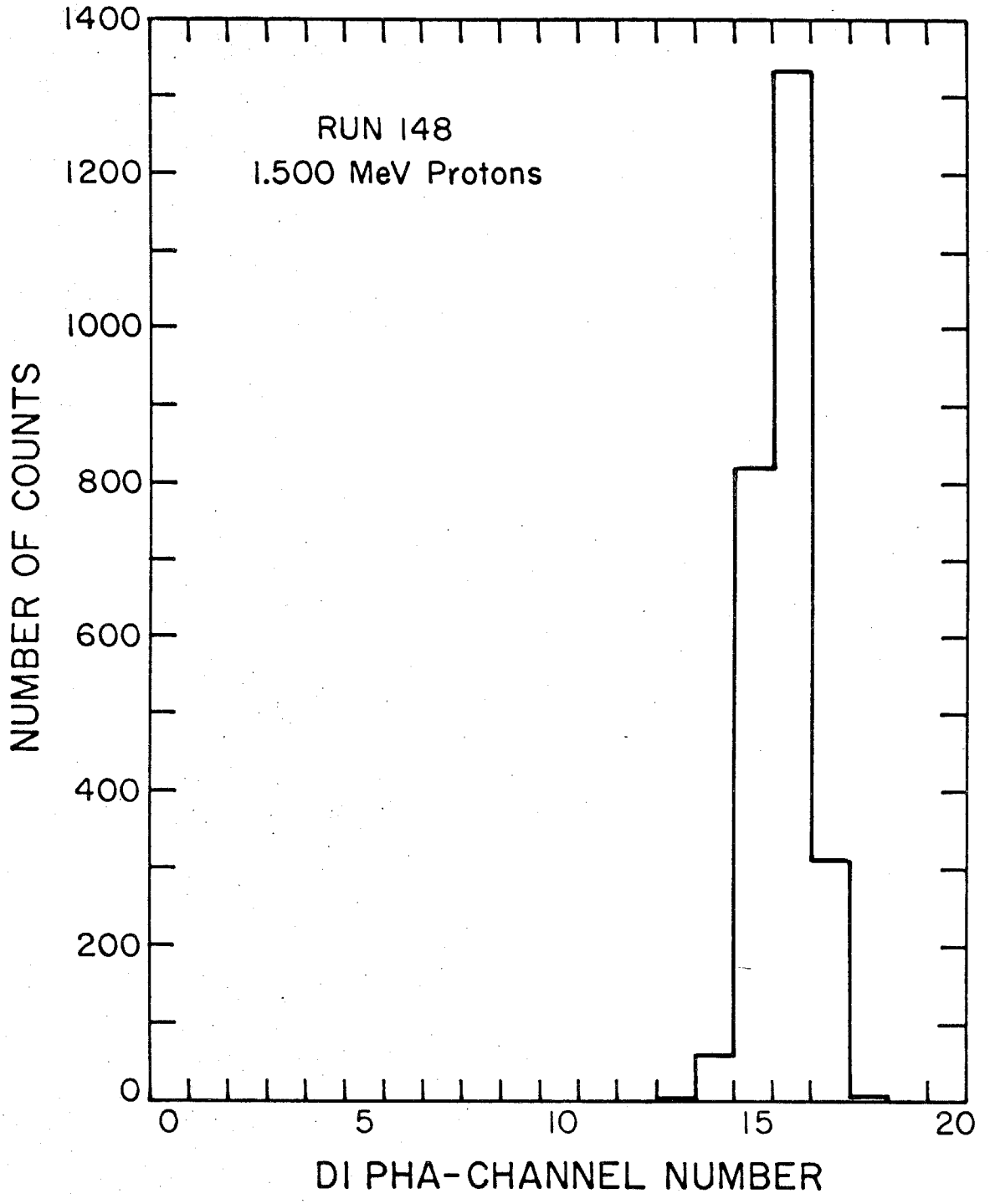
RUN 148
1.500 MeV Protons
NUMBER OF COUNTS
1400
1200
1000
800
600
400
200
0
0
5
10
15
20
DI PHA-CHANNEL NUMBER

Figure A-3

D1 vs. D2 pulse height distribution for 5.000 MeV protons. The number of events with a given pulse height in D1 and D2 is listed in the figure at the appropriate location in the D1-D2 pulse height matrix. The D1 and D2 pulse height scales are pseudo logarithmic. Therefore, the scale labels do not refer directly to pulse height channels for the D1 or D2 PHA. See appendix D.

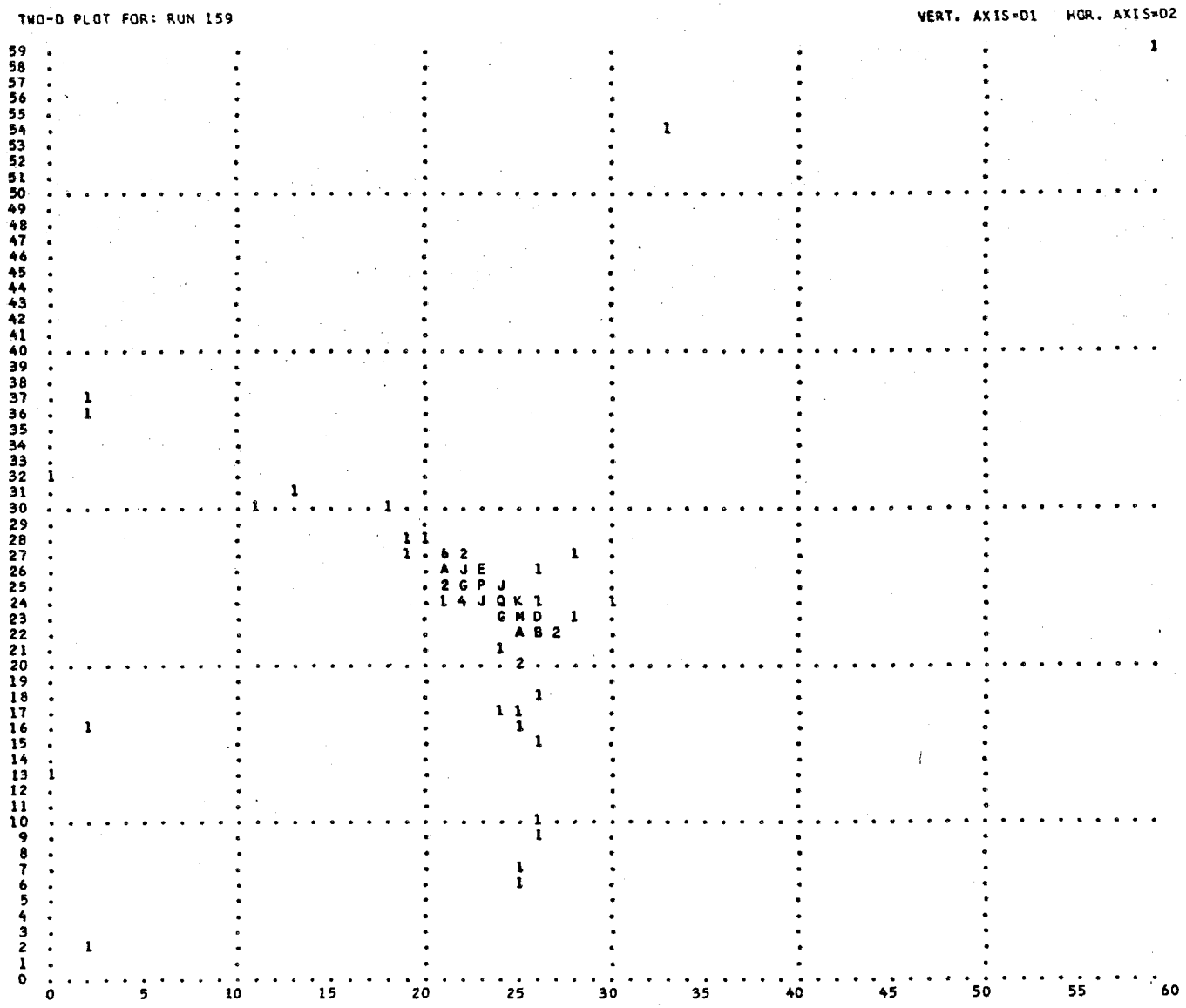
TWO-D PLOT FOR: RUN 159
VERT. AXIS=D1 HOR. AXIS=D2
0 5 10 15 20 25 30 35 40 45 50 55 60

Figure A-4

D2 vs. D3 pulse height distribution for 19.00 MeV protons. See figure A-3.

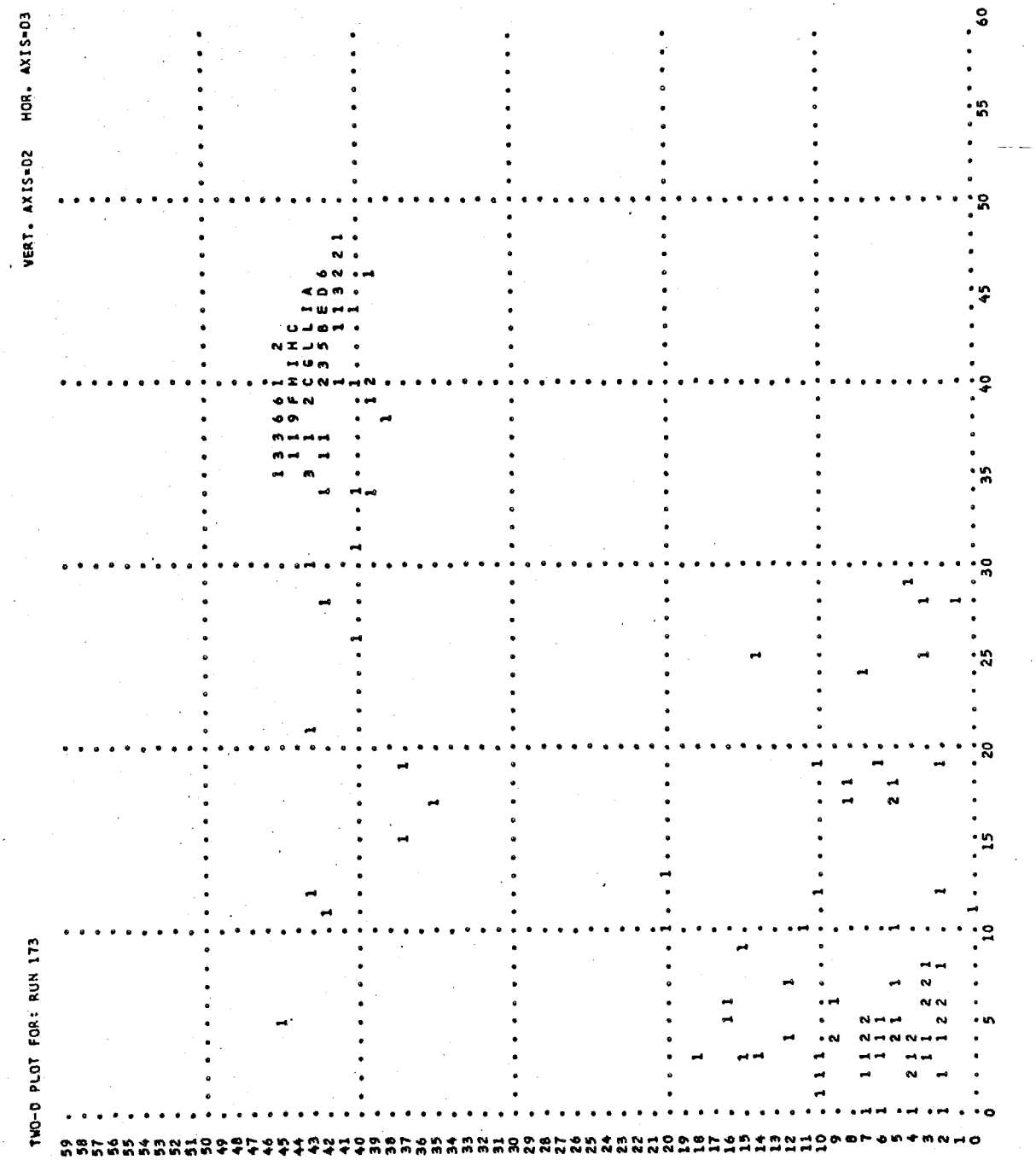
TWO-D PLOT FOR: RUN 173
VERT. AXIS=02 HOR. AXIS=03

Figure A-5

Comparison of electronic calibration for D1 and the accelerator calibration. The expected energy loss in D1 for the incident energy protons shown in the plot are calculated and plotted vs. the D1 PHA channel corresponding to the peak of the energy loss distributions in D1 for those peaks.

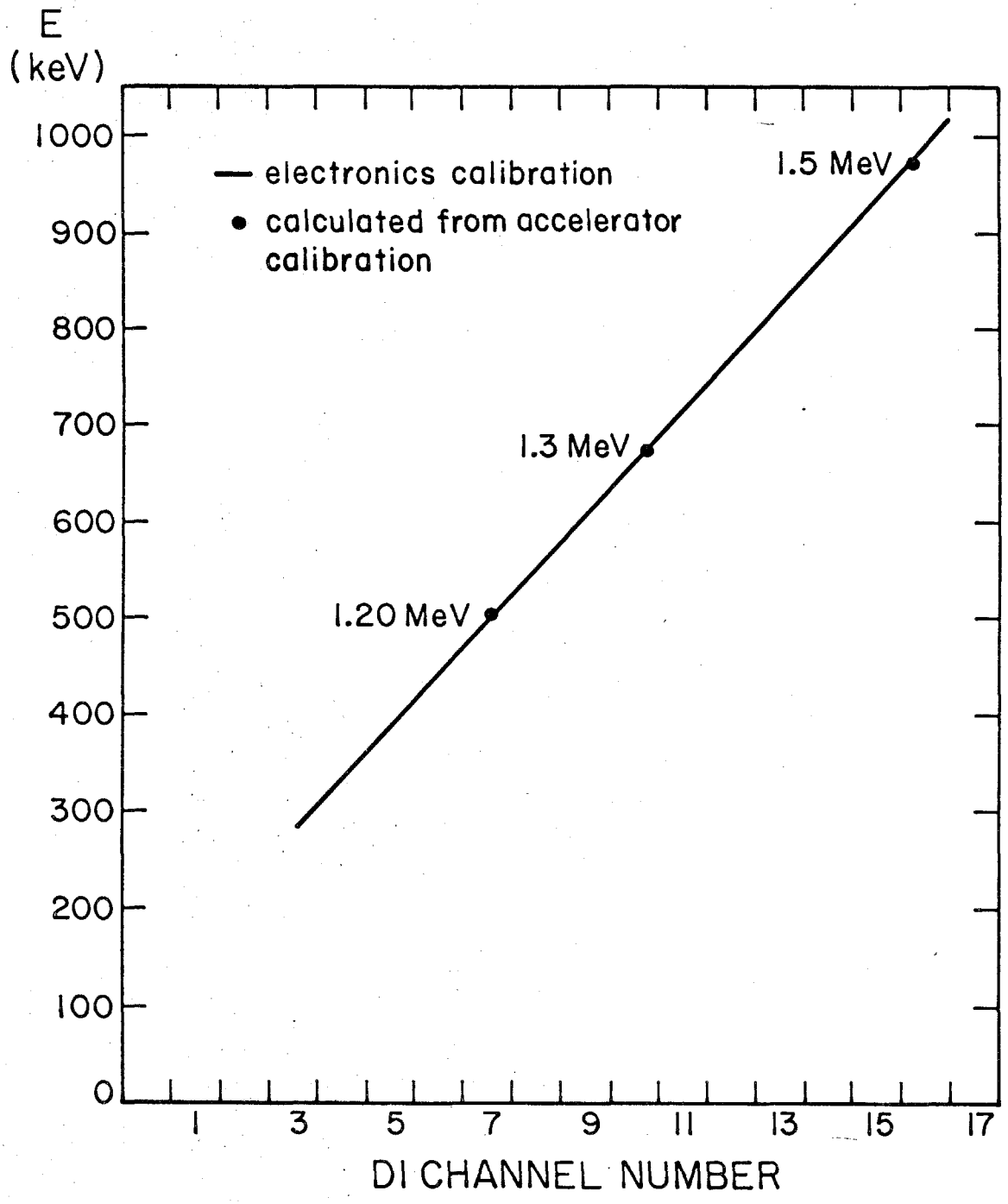
E
(keV)
1000
900
800
700
600
500
400
300
200
100
0
electronics calibration
calculated from accelerator calibration
1.5 MeV
1.3 MeV
1.20 MeV
1
3
5
7
9
11
13
15
17
DI CHANNEL NUMBER

distributions in D1 are compared with those predicted from the electronic calibrations. We find in both cases that the resolution is given by a sigma of ~20 keV.

The thicknesses of detectors D1, D2 and D3 and the thickness of absorber A2 are determined from the data as follows:

1) For each detector a plot of the percentage of incident protons which penetrate the detector as a function of energy is made. This will be an approximately Gaussian function since range straggling has this functional form. Figures A-6, -7 and -8 are the plots obtained for D1, D2 and D3.

2) The threshold energy for penetration is taken to be the 50% point on these plots. Using range-energy tables (25) for protons in lucite and silicon, the detector thicknesses can be determined by finding the range of the threshold energy proton and subtracting the thickness of any material in front of the detector.

3) A sample calculation is given below:
Aluminized mylar window thickness = 2.32 mg/cm^2
and assume mylar ≡ lucite for range-energy table

Figure A-6

Integral Gaussian plot of the percentage of protons penetrating D1 vs. the incident kinetic energy of these protons.

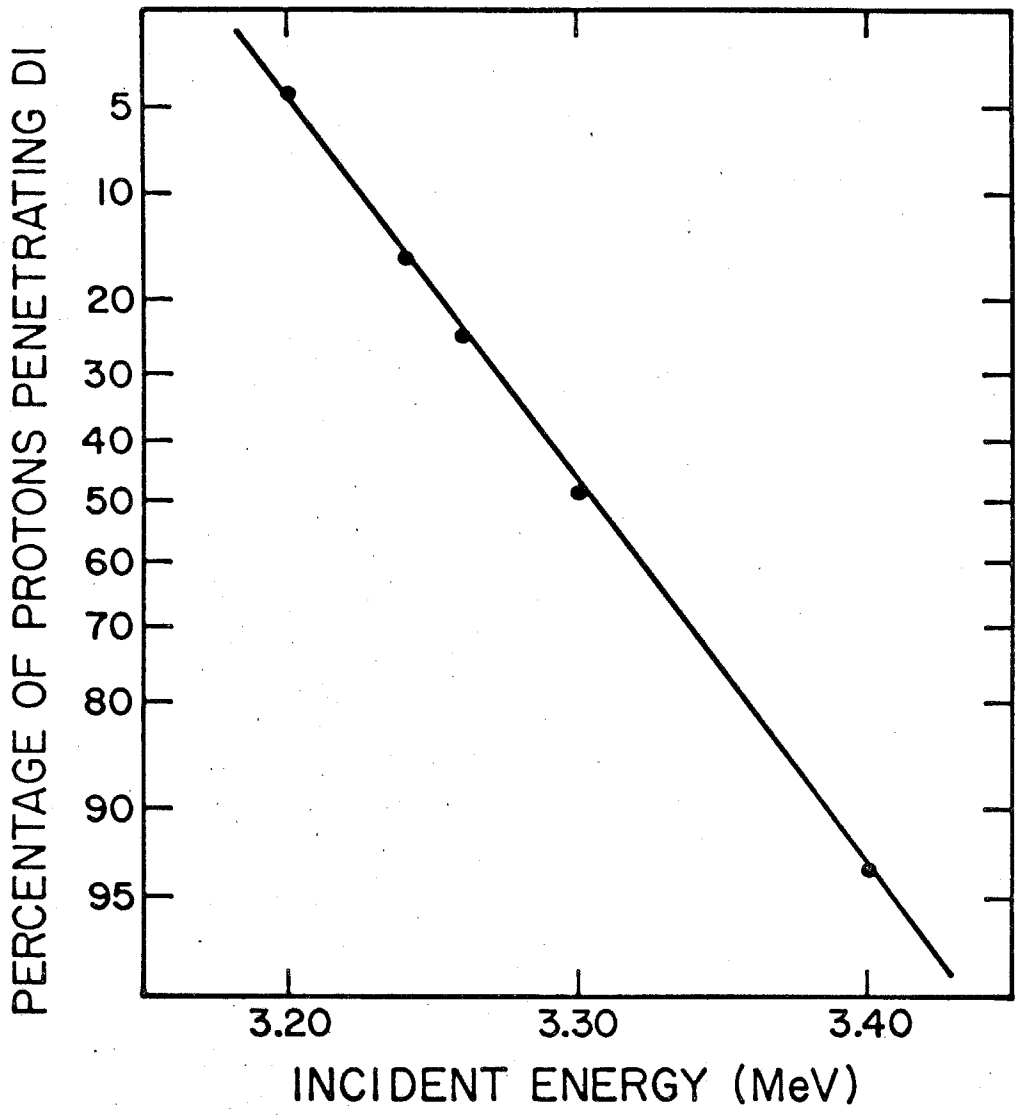
PERCENTAGE OF PROTONS PENETRATING DI
5
10
20
30
40
50
60
70
80
90
95
3.20
3.30
3.40
INCIDENT ENERGY (MeV)

Figure A-7

Integral Gaussian plot of the percentage of protons penetrating D2 vs. the incident kinetic energy of these protons.

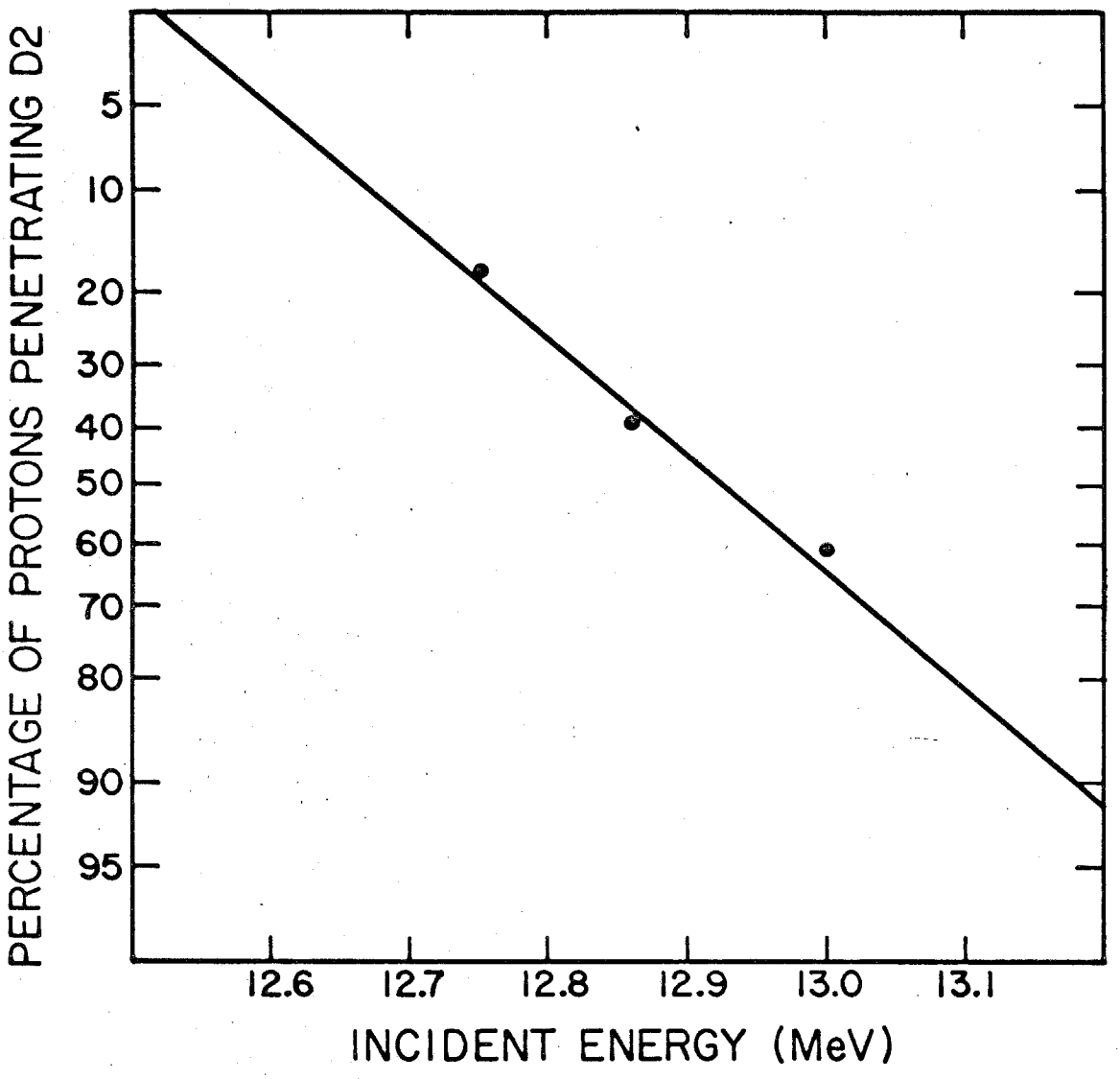
PERCENTAGE OF PROTONS PENETRATING D2
5
10
20
30
40
50
60
70
80
90
95
12.6
12.7
12.8
12.9
13.0
13.1
INCIDENT ENERGY (MeV)

Figure A-8

Integral Gaussian plot of the percentage of protons penetrating D3 vs. the incident kinetic energy of these protons.

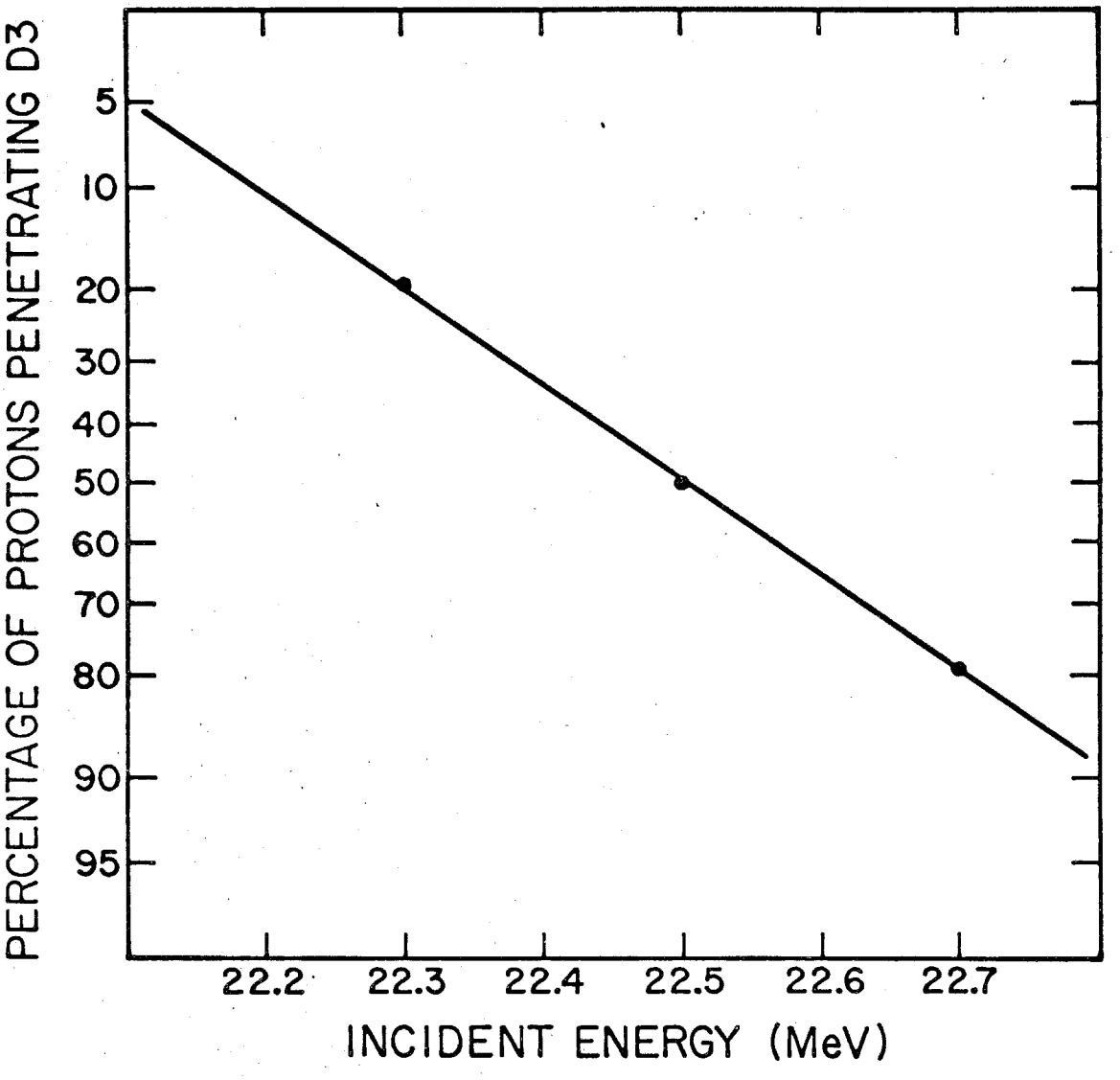
PERCENTAGE OF PROTONS PENETRATING D3
5
10
20
30
40
50
60
70
80
90
95
22.2
22.3
22.4
22.5
22.6
22.7
INCIDENT ENERGY (MeV)

use. The threshold energy for penetration of D1 = 3.31 MeV.

a) Energy of a 3.31 MeV proton after penetrating the mylar window.

$R_M(E) = R_M(3.31) - 2.32\ mg/cm^2 = 15.3\ mg/cm^2$

$E(R_M) = 3.05$ MeV

b) Range in silicon of a 3.05 MeV proton. This gives the thickness of D1

$R_{Si}(3.05) = 22.1\ mg/cm^2$ = thickness of D1

4) Similar calculations are made for each of the detectors and the results are given in table A-III.

The D1 vs. D2, and D2 vs. D3 pulse height plots define a band of pulse heights in which all protons should lie. For protons from 1-15 MeV, which are discussed in this thesis, the D1-D2 plots from the calibrations are used to construct this band. The construction and use of the band is discussed in section IV.

TABLE A-III

DETECTOR AND ABSORBER THICKNESSES

Absorber/Detector	Thickness
Window (Aluminized Mylar)	2.32 mg/cm^2
D1 (Silicon)	22.1
D2 (Silicon)	233
A2 (Aluminum)	206
D3 (Silicon)	227

Appendix B

User's Guide to OGO-VI Rate Plots

SRL Internal Report No. 21

S. S. Murray

June, 1970

EXPERIMENT

Instrumentation and Measurement

The cosmic ray experiment on OGO-VI (experiment F-20) consists of 3 charged particle telescopes. Each telescope is oriented so that it points away from the surface of the earth (-Z direction in spacecraft coordinates). These telescopes (Range, Čerenkov, Flare) monitor cosmic ray charged particles in various energy and flux intervals. The Range telescope allows differential flux measurements to be obtained for protons and helium nuclei with energy from ~1 MeV/nucleon to ~300 MeV/nucleon and integral flux determinations for higher energies. With the proper ground commands, this telescope can also monitor electrons with energies from 250 keV to 2 MeV. The Čerenkov telescope is capable of differential flux measurements for charge particles up to Z = 8 in the energy range from ~450 MeV/nucleon to ~1 GeV/nucleon. Integral fluxes are obtained for energies greater than 1 GeV/nucleon. Both of these telescopes are designed to be operative when the incident flux is less than 10^5 particles/m^2 sec. The Flare telescope is sensitive to protons and helium nuclei in the energy range 17 MeV/nucleon to ~100 MeV/nucleon. Because it has a very small geometrical factor compared with the other telescopes, this telescope is operable for incident fluxes up to 10^{10} particles/m^2 sec. The experiment has been described by Althouse *et al.* (B1) at the

IEEE Nuclear Science Symposium. The brief description which follows is therefore not intended to be complete.

The Range telescope (figure B-1) consists of seven totally depleted gold-silicon surface barrier detectors (D1-D7) mounted in a stack with five absorbers (A2-A6) sandwiched between the detectors. Surrounding the stack is a plastic scintillator cup which is viewed by a photomultiplier tube (D8). A 0.00075 inch aluminized mylar window which serves as a light shield covers the top of the scintillator. Table B-I lists the relevant characteristics of the detectors and associated electronics. The window coupled with the discriminator threshold of D1 sets the low energy threshold of the Range telescope at 1.17 MeV for protons. The discriminator thresholds for D2-D7 are set so that at least 99% of all minimum ionizing protons will trigger the circuit. D4-D7 have an additional discriminator which provides crude energy loss determinations in these detectors. The energy loss in D1-D3 is determined more accurately with the aid of three 256 channel pulse height analyzers. For low energy particles which do not reach D4 the energy losses in D1-D3 are recorded. For higher energy particles the energy losses in D2 and D3 are recorded along with information indicating the range of the particle.

The Čerenkov telescope consists of two totally depleted gold-silicon surface barrier detectors (D1', D2') mounted in

Figure B-1

Cross-sectional view of the Range telescope.

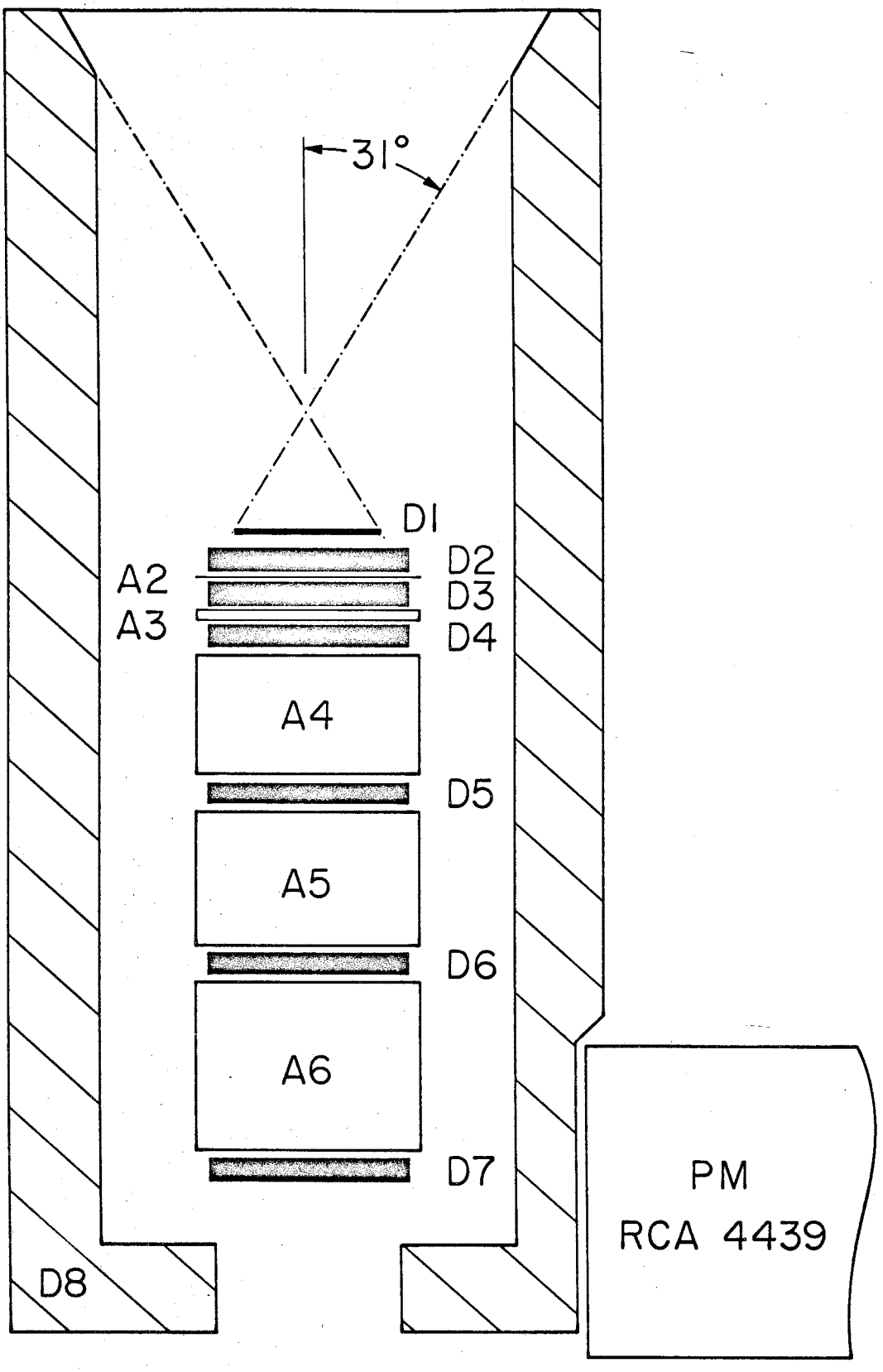
31°
D1
A2
A3
D2
D3
D4
A4
D5
A5
D6
A6
D7
D8
PM
RCA 4439

TABLE B-I

RANGE TELESCOPE DETECTORS

Detector	Thickness (mg/cm^2)	Area (cm^2)	Discriminator Thresholds Low (keV)	High keV)
D1	22.1±3%	2.01±6%	398±8	
D2	233	3.80	147±4	
D3	227	4.08	153±3	
D4	227	3.87	149±4	563±14
D5	236	4.01	142±4	559±14
D6	227	4.08	141±4	700±15
D7	236	4.08	148±4	841±19

RANGE TELESCOPE ABSORBERS

Absorber	Thickness (gm/cm^2)	
A2	0.205±1%	(Aluminum)
A3	2.94	(Mallory 2000 Tungsten Alloy)
A4	27.57	(Mallory 2000 Tungsten Alloy)
A5	30.98	(Mallory 2000 Tungsten Alloy)
A6	38.73	(Mallory 2000 Tungsten Alloy)
Window	0.00232±1%	(Mylar)

RANGE TELESCOPE ANTICOINCIDENCE

PM Tube	Scintillator	Threshold Energy Protons	Electrons	Gamma Rays	μ-Mesons
RCA 4438	NE 102 0.375" thick	8.9 MeV	0.62 MeV	0.42 MeV	3.5 MeV

an aluminum can which is on top of a 1 cm thick quartz window of a photomultiplier tube (D3'). This stack is surrounded by a plastic scintillator viewed by another photomultiplier tube. The top of this telescope is also covered by a .00075 inch aluminized mylar window. Figure B-2 shows a cross-sectional view of the Čerenkov telescope and table B-II lists the relevant characteristics of the detectors and associated electronics.

The Flare telescope consists of two totally depleted gold-silicon surface barrier detectors (D5', D6') and one absorber between them (equivalent to A2 in the Range telescope). These are mounted in a gold plated copper collimator which will stop protons up to ~100 MeV. An aluminum foil window simulates the window and detector D1 of the Range telescope so that the responses of D5' and D6' are essentially the same as those of D2 and D3 in the Range telescope. Figure B-3 shows a cross-sectional view of the Flare telescope, and table B-III lists the relevant characteristics of the detectors and associated electronics.

DATA

The experiment data are read by the spacecraft telemetry system and transmitted to the various ground stations. Each readout consists of data associated with the most recent event detected. An event is defined by a specific combination of logic signals from the telescopes. Table B-IV contains the

Figure B-2

Cross-sectional view of the Čerenkov telescope.

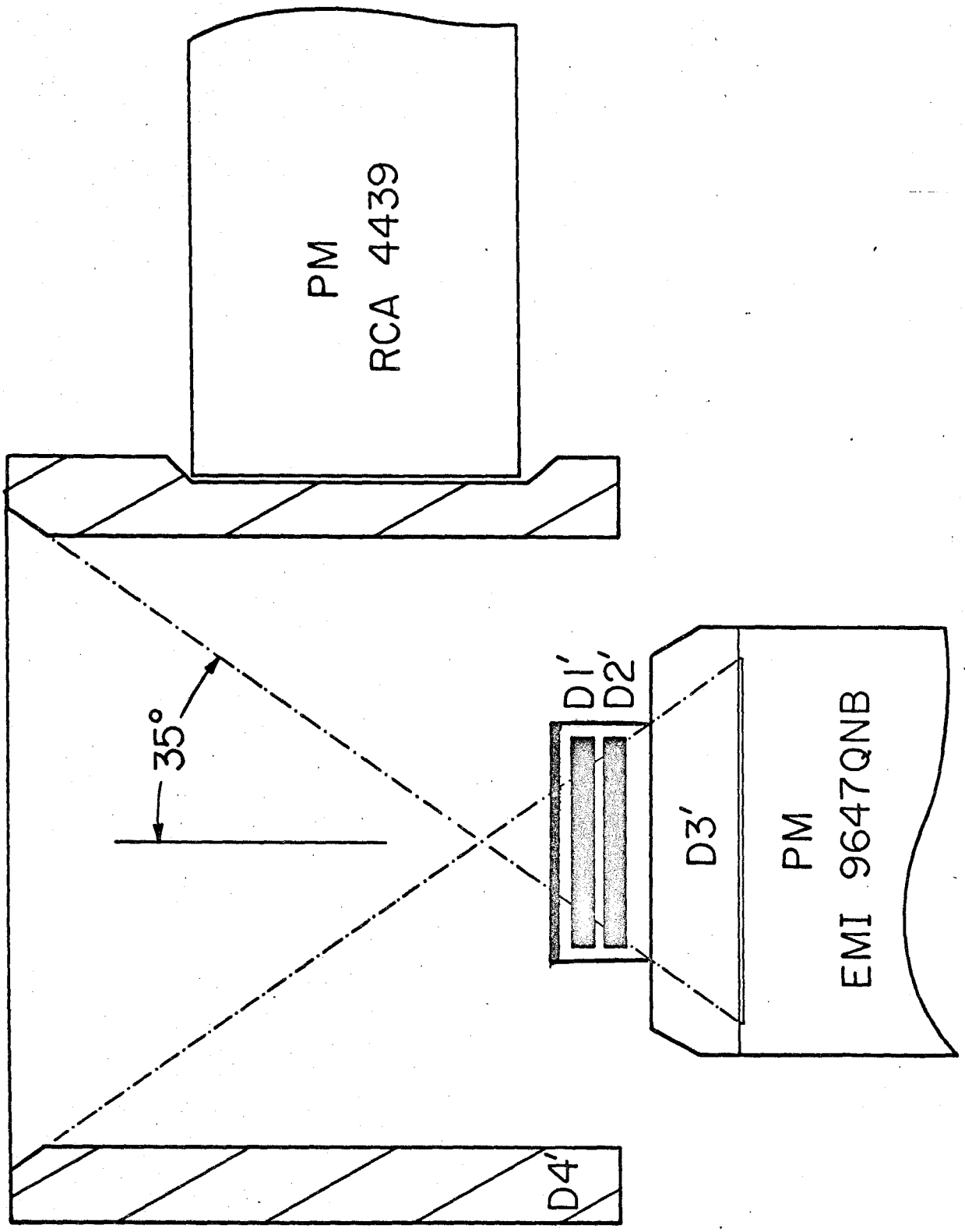
PM
RCA 4439
35°
D1'
D2'
D3'
PM
EMI 9647QNB
D4'

TABLE B-II

ČERENKOV TELESCOPE DETECTORS

Detector	Thickness (mg/cm^2)	Area (cm^2)	Discriminator Threshold (keV)
D1'	254±3%	4.30±6%	169±4
D2'	245±3%	4.30±6%	155±3
D3'*	1 cm quartz	~20	$(2.01\pm.03) \times 10^{-1}$

*D3' is the quartz Čerenkov radiator. Discriminator and amplifier saturation are given in units of the Čerenkov peak for a charge Z = 1 particle with velocity β = 1.

ČERENKOV TELESCOPE ANTICOINCIDENCE

PM Tube	Scintillator	Threshold Energy			
		Protons	Electrons	Gamma Rays	μ-Mesons
RCA 4438	NE 102 0.25"thick	10.2 MeV	0.70 MeV	0.42 MeV	4.0 MeV

Figure B-3

Cross-sectional view of the Flare telescope.

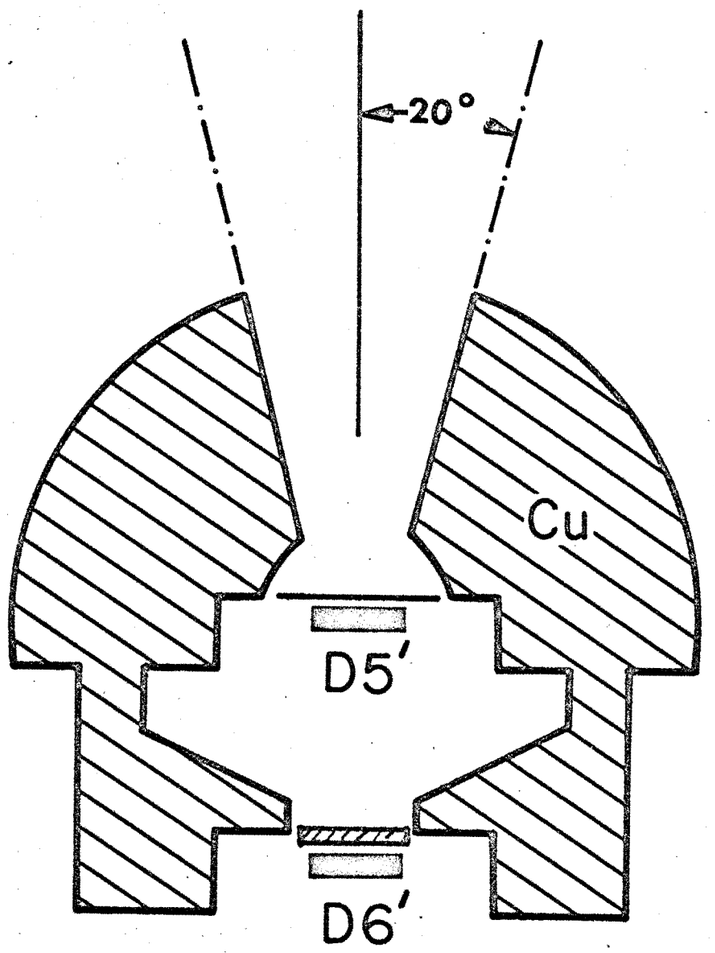
20°
Cu
D5′
D6′

TABLE B-III

FLARE TELESCOPE DETECTORS AND ABSORBERS

Detector	Thickness (mg/cm^2)	Area (cm^2)	Discriminator Threshold (keV)
D5'	245±3%	0.224±6%	408±5
D6'	233	0.203	370±5
WINDOW	29.5 (Aluminum)		
ABSORBER	194 (Aluminum)		

TABLE B-IV

EVENT ENERGY THRESHOLDS

Event	Threshold Energy (Protons MeV)	Geometrical Factor (cm^2-sterad)
$D1\overline{D8}$	1.17±3%	1.14±6%
$D1D2\overline{D8}$	3.31	1.14
$D2D3\overline{D8}$	17.9	1.62
$D2D3R4\overline{D8}$	45.2	1.38
$D2D3R5\overline{D8}$	152	0.824
$D2D3R6\overline{D8}$	230	0.480
$D2D3R7\overline{D8}$	309	0.259
$D1'D2'D3'\overline{D4'}$	350	2.58
D5'D6'	17.9	0.0231

Note: Geometrical factors for the Range telescope events are energy dependent. The values listed are for the threshold energies. Figure B-4 is a plot of the geometrical factor as a function of energy.

Figure B-4

Geometrical factor for the Range telescope vs. incident particle kinetic energy.

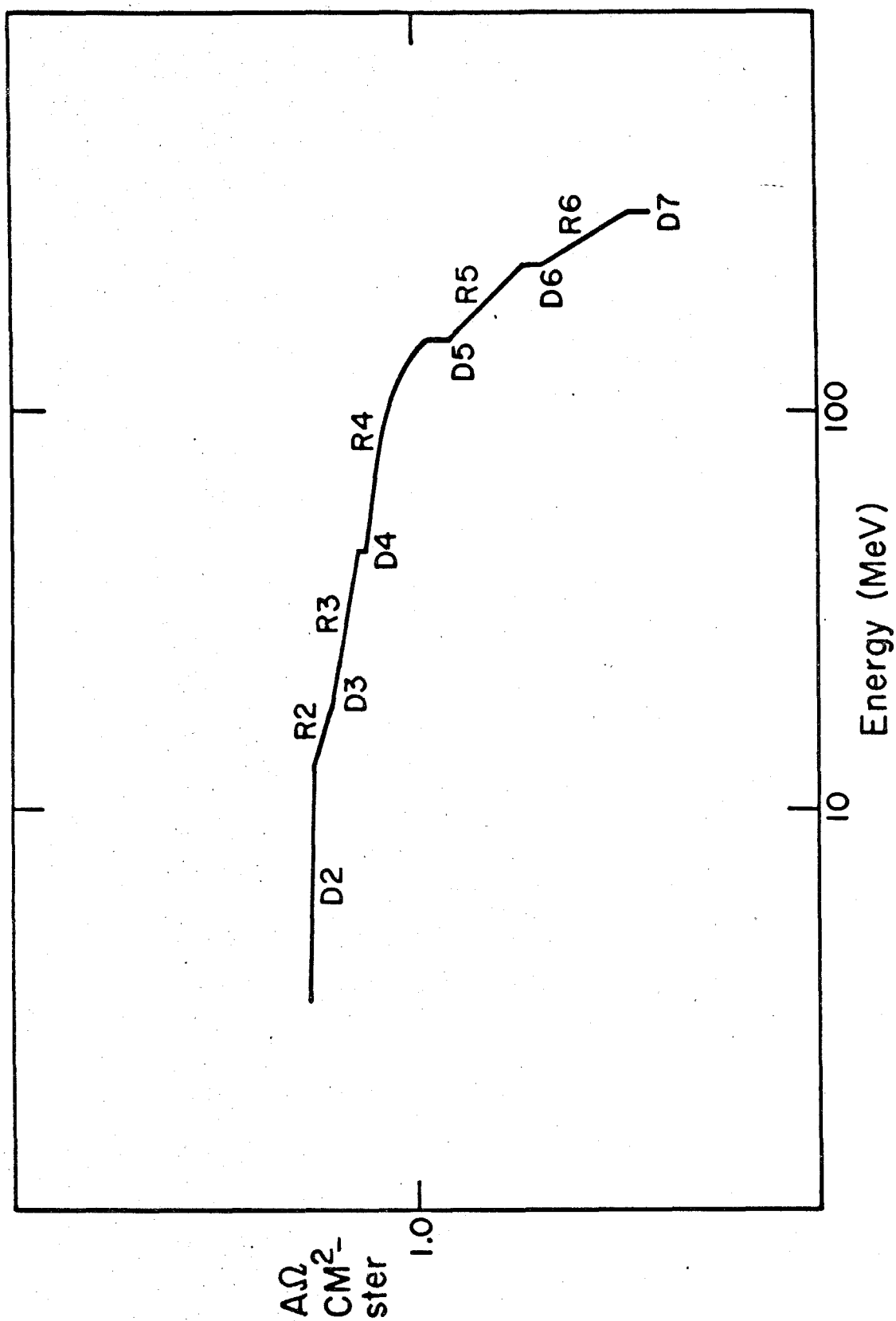
D2
R2
D3
R3
D4
R4
D5
R5
D6
R6
D7
1.0
10
100
Energy (MeV)
AΩ
CM2-
ster

definitions of events and the threshold energies at which they occur. For each event, appropriate energy loss and range data are recorded as well as the various coincidence and singles rates monitored by the experiment.

The user is referred to SRL Internal Report No. 19 (B2) for details concerning the data from this experiment. Summarized briefly, the data in any readout of the instrument consist of the following:

1) Event type indicators
2) New event flag
3) Pulse height information appropriate to the event
4) Range data when applicable
5) Commutated rate data
6) Temperature/Command mode data

From the above data various plots vs. universal time are made and recorded on 35 mm microfilm. Examples are shown in figures B-5, -6 and -7. This film is submitted to the National Data Center. The plots contain the following data:

1) Rates (plotted logarithmically vs. UT)
   (See table B-V.)
2) Representative pulse height data vs. UT
   (Scatter plots) (See table B-VI.)
3) Orbital data vs. UT
   (See table V-II.)

Figure B-5

Typical Rate Plot page 1.

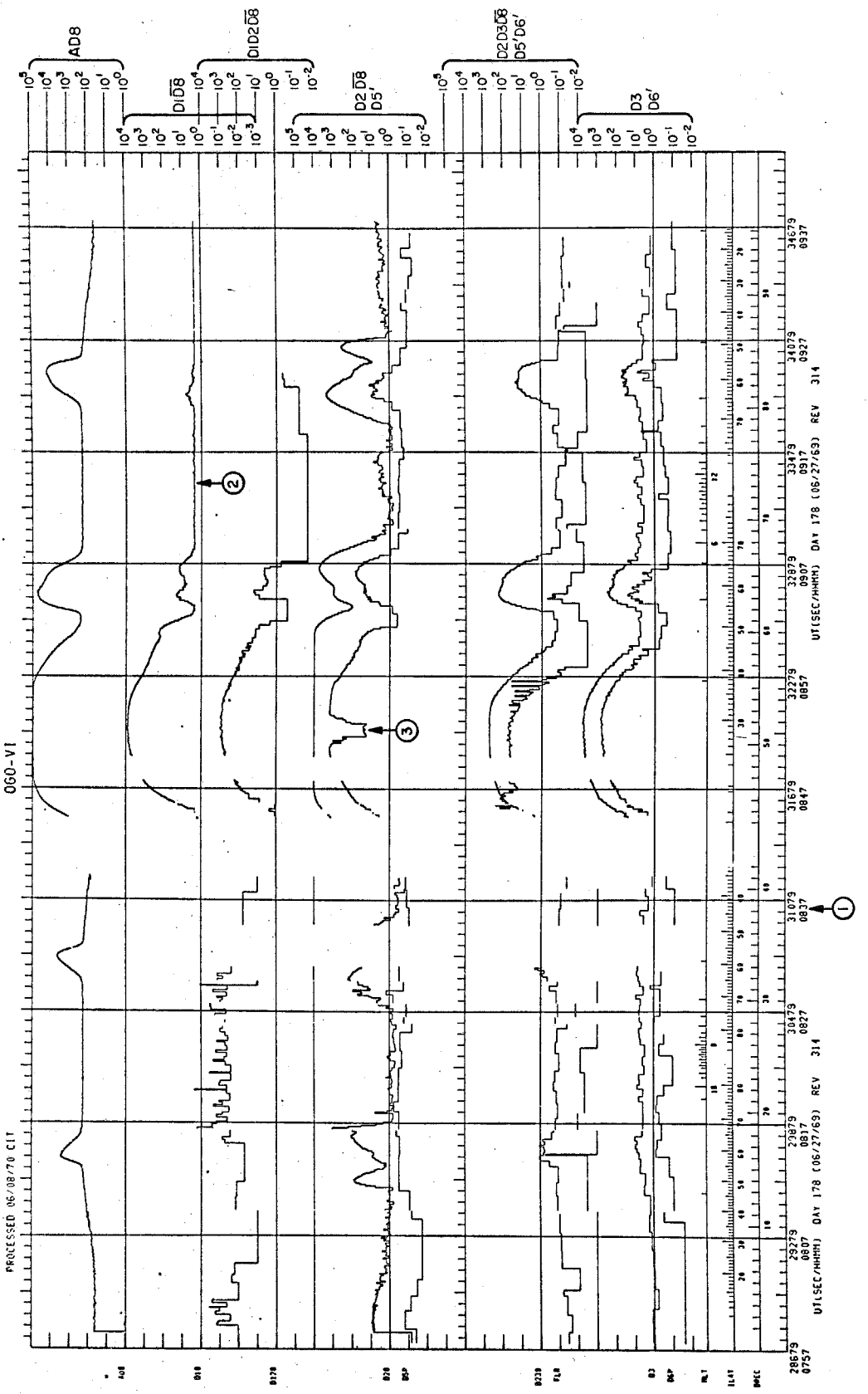
AD8
DiD8
DiD2D8
D2D8
D2D3D8
D5'D6'
D3
D6'
D5'
OGO-VI
PROCESSED 06/08/70 CIT
UT(SEC/HHMM) DAY 178 (06/27/69) REV 314
UT(SEC/HHMM) DAY 178 (06/27/69) REV 314
①
②
③

Figure B-6

Typical Rate Plot page 2.

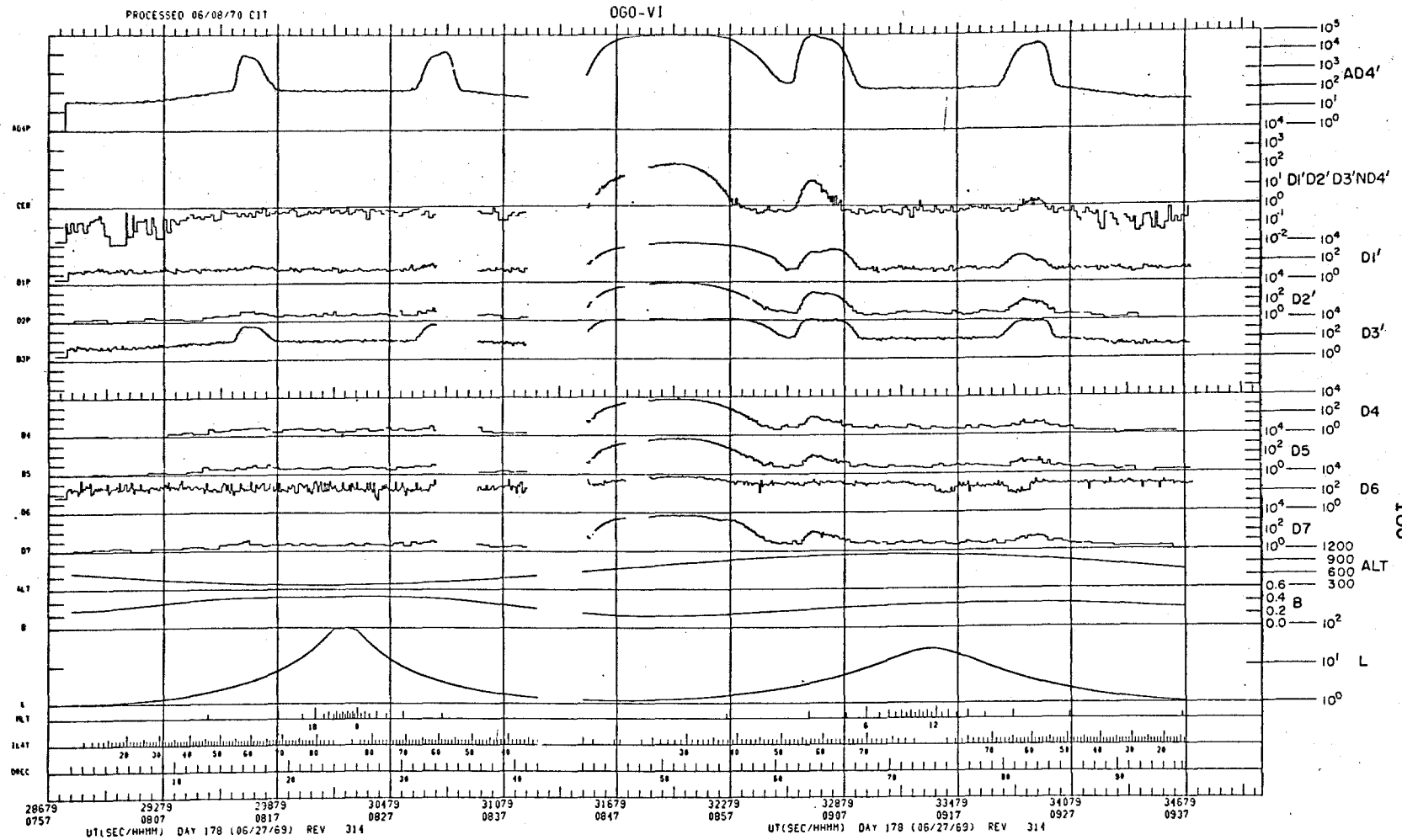
PROCESSED 06/08/70 CIT
OGO-VI
AD4P
CEB
D1P
D2P
D3P
D4
D5
D6
D7
ALT
B
L
MLT
ILAT
DREC
AD4'
D1'D2'D3'ND4'
D1'
D2'
D3'
D4
D5
D6
D7
ALT
B
L
28679 0757
29279 0807
29879 0817
30479 0827
31079 0837
31679 0847
32279 0857
32879 0907
33479 0917
34079 0927
34679 0937
UT(SEC/HHMM) DAY 178 (06/27/69) REV 314
UT(SEC/HHMM) DAY 178 (06/27/69) REV 314

Figure B-7

Typical Rate Plot page 3.

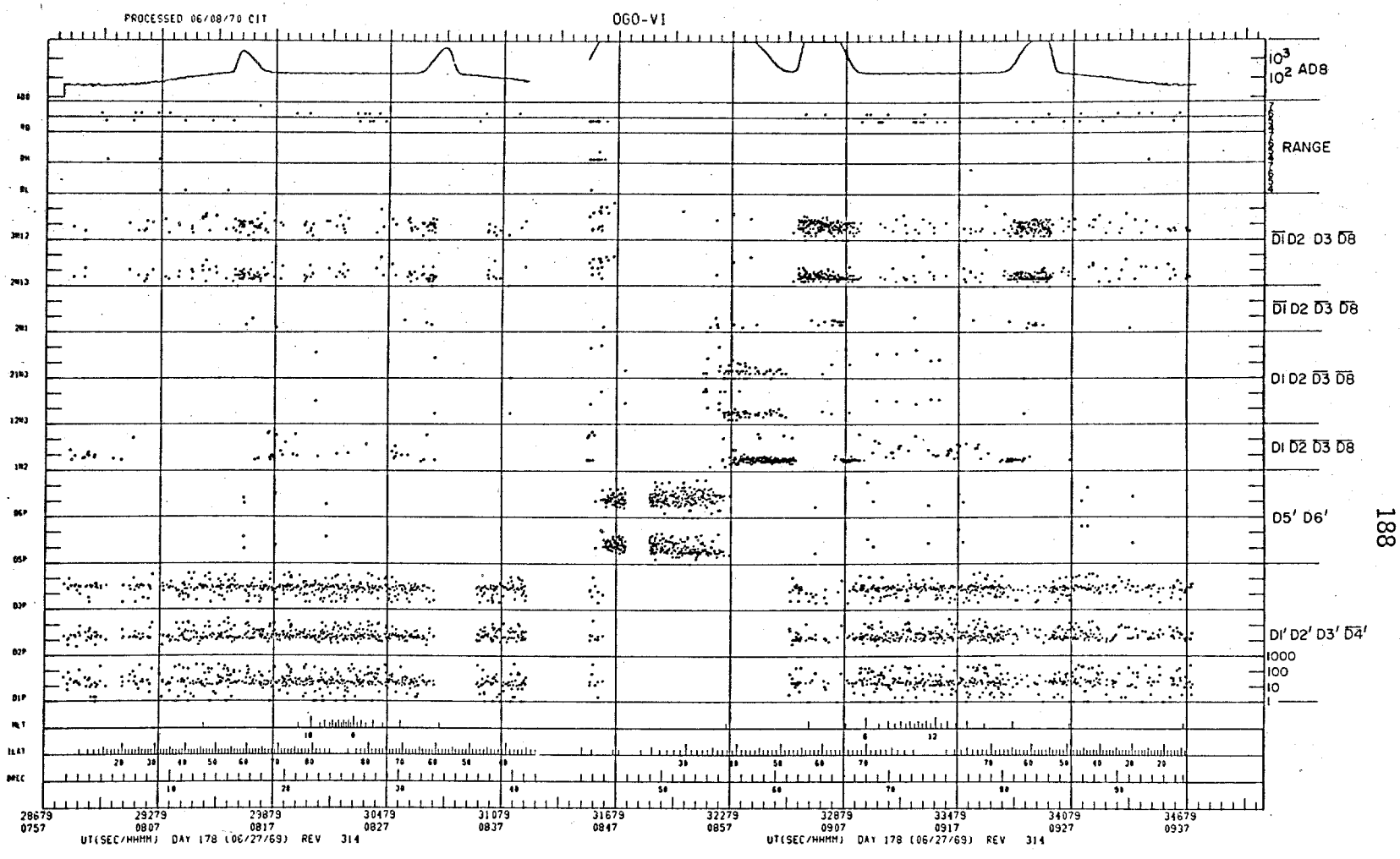
PROCESSED 06/08/70 CIT
OGO-VI
10^3
10^2 AD8
RANGE
$\overline{D1}$ D2 D3 $\overline{D8}$
$\overline{D1}$ D2 $\overline{D3}$ $\overline{D8}$
D1 D2 $\overline{D3}$ $\overline{D8}$
D1 $\overline{D2}$ $\overline{D3}$ $\overline{D8}$
D5′ D6′
D1′ D2′ D3′ $\overline{D4}$′
1000
100
10
1
28679
0757
29279
0807
29879
0817
30479
0827
31079
0837
31679
0847
32279
0857
32879
0907
33479
0917
34079
0927
34679
0937
UT(SEC/HHMM) DAY 178 (06/27/69) REV 314
UT(SEC/HHMM) DAY 178 (06/27/69) REV 314

TABLE B-V

RATES*

Rate	Plot Label	Scale†	Min Max (sec^{-1})
D8	AD8	1	10^0- 10^5
D1$\overline{D8}$	D18	1	10^{-3}-10^4
D1D2$\overline{D8}$	D128	1	10^{-2}-10^4
D2$\overline{D8}$	D28	1	10^{-3}-10^4
D5'	D5P	1	10^{-3}-10^5
D2D3$\overline{D8}$	D238	1	10^{-3}-10^4
D5'D6'	FLR	1	10^{-3}-10^5
D3	D3	1	10^{-2}-10^4
D6'	D6	1	10^{-2}-10^4
D4'	Ad4P	1	10^0-10^5
D1'D2'D3'$\overline{D4'}$	CER	1	10^{-2}-10^4
D1'	DIP	1/2	10^0-10^4
D2'	D2P	1/2	10^0-10^4
D3'	D3P	1/2	10^0-10^4
D4	D4	1/2	10^0-10^4
D5	D5	1/2	10^0-10^4
D6	D6	1/2	10^0-10^4
D7	D7	1/2	10^0-10^4

*Rates are plotted as $\log_{10}$ (rate) vs. time; tick marks drawn for each decade and labeled in the accompanying figures B-5, -6 and -7.

†Scale is relative scale; if plot is enlarged so that full scale in the vertical direction is 10 inches scale of 1 => 1/4"/decade.

TABLE B-VI

PULSE HEIGHT DATA

I) RANGE EVENTS WITH RANGE INDICATORS

A range event with range indicators means a D2D3$\overline{D8}$ coincidence with at least one of D4-D7 also in coincidence. These events are broken down into 3 categories for plotting.

RL) Only the low level range discriminators have been triggered (RL). The final range value (4, 5, 6 or 7) is plotted if all the preceding ranges have also fired.

RH) The high and low level discriminators have been triggered for each range indicator (RH). The final range value is plotted if all the preceding ranges have also fired.

RO) Combinations of high and low discriminators have been triggered (RO). The final range value is plotted if all the preceding ranges have also fired.

All other range events are not plotted.

II) OTHER EVENTS†

Event	Label	Pulse Height Plotted
$\overline{D1}$D2D3$\overline{D8}$	3N12	D3
$\overline{D1}$D2D3$\overline{D8}$	2N13	D2
$\overline{D1}$D2$\overline{D3}\overline{D8}$	2N1	D2
D1D2$\overline{D3}\overline{D8}$	21N3	D2
D1D2$\overline{D3}\overline{D8}$	12N3	D1
D1$\overline{D2}\overline{D3}\overline{D8}$	1N2	D1
D5'D6'	D6P	D6'
D5'D6'	D5P	D5'
D1'D2'D3'$\overline{D4'}$	D3P	D3'
D1'D2'D3'$\overline{D4'}$	D2P	D2'
D1'D2'D3'$\overline{D4'}$	D1P	D1'

†All pulse heights are plotted as $\log_{10}$ (pulse height) vs. time. A maximum of 1 event/sec is plotted.

TABLE B-VII

ORBITAL DATA

Datum	Plot Label	Comments	Units
Magnetic Local Time (B3)	MLT	MLT = $(\Phi_0-\Phi_s)/15+12$ where Φ_s = dipole longitude of sun (degrees) Φ_0 = dipole longitude of spacecraft (degrees)	Hours
Invariant Latitude	ILAT	ILAT = $\cos^{-1}(1/\sqrt{L})$ where L = McIlwain parameter (earth Radii)	Degrees
Orbital Record Number	DREC	Orbital data record number on CIT abstract tape	
Altitude	ALT	Altitude of spacecraft (from GSFC orbit tape)	Km
Magnetic Field	B	Magnetic field strength (from GSFC orbit tape)	Gauss
McIlwain Parameter	L	Magnetic shell parameter (from GSFC orbit tape)	Earth Radii

For each orbit of the satellite three pages of plots are produced. In addition to the information mentioned above, each plotted page contains a time line on which the satellite position in invariant latitude and magnetic local time is given. These plots are also labeled with the data date, day number, revolution number and date of processing.

Problems in Data

As presented, there are several annoying but relatively minor errors on the rate plots. Some of these are due to problems in the raw data; others are due to program bugs. Since these are minor problems, the data which were already plotted have not been replotted.

1) The most significant error deals with labels on the time axis. The time axis has one minute tick marks with a label every 10 minutes. An error in round off results in times (in seconds) that end in a "9" instead of a "0". Such times are 1 second too small, thus a time of xxx49 seconds should be read as xxx50 seconds. Whenever the printed time in seconds ends with a "9", the time in hours and minutes which is listed below will be 1 minute too small. Figure B-5(1) illustrates this.

2) Due to a problem with the raw data, a rate (usually $D1\overline{D8}$ or D5') will appear to be constant

for a long time (>10 minutes) at a value greater than 1 count/second. This can be recognized fairly easily since the normal statistical fluctuations in the rate are not present. Figure B-5(2) illustrates this problem.

3) Finally the D5' rate will occasionally appear to change drastically from a high rate to a lower rate. This is due to a program bug and is again easily spotted. Figure B-5(3) illustrates this problem.

Conclusions

We have tried to provide sufficient instruction to allow the use of the OGO-VI rate plots which are available in the National Data Center. However, in the actual use of these data questions may well arise which are not covered here. These should be referred to:

Dr. E. C. Stone
220 Downs Laboratory
California Institute of Technology
1201 E. California Boulevard
Pasadena, California 91109

REFERENCES

B1. W. E. Althouse et al., "A Solar and Galactic Cosmic Ray Satellite Experiment," IEEE Transactions on Nuclear Science, 15, pp 229-237 (1968).

B2. S. S. Murray, "OGO-F-20 Data Format," California Institute of Technology, Space Radiation Laboratory Internal Report No. 19 (1970).

B3. T. A. Fritz and D. A. Gurnett, "Diurnal and Latitudinal Effects Observed for 10 KeV Electrons at Low Satellite Altitudes," J. Geophys. Res. 70, 2485 (1965)

Appendix C

Anisotropic Diffusion with a Boundary Convection and Energy Changes (ADBCEC) Model

We will derive a solution to the transport equation 6-38 which is exact and in closed form using the following assumptions:

1) Solar wind is radial
2) Magnetic field is radial
3) Perpendicular diffusion coefficient increases as r^2
4) Parallel diffusion coefficient increases as r
5) Effective time constant for energy changes increases as r
6) Parameters are independent of energy
7) The density spectrum is a power law in kinetic energy
8) Impulsive injection of particles
9) Boundary conditions are that the density is zero at r = 0 and r = D.

The solution which we obtain is a generalization of the solution obtained for a similar set of assumptions by Forman (55).

We want to find a solution to the equation

$$\frac{\partial n}{\partial t} = \nabla\cdot(\underline{\underline{\kappa}}\nabla n) - \nabla\cdot(n\vec{V}) + \frac{1}{\tau_E}\frac{\partial}{\partial_T}(nT) \qquad (C\text{-}1)$$

in spherical coordinates we have

$$\frac{\partial n}{\partial t} = \frac{1}{r^2}\frac{\partial}{\partial r}\left[r^2\left(\kappa_{\parallel}\frac{\partial n}{\partial r} - nV\right)\right] + \frac{1}{r^2}\frac{\partial}{\partial \mu}\left[(1-\mu^2)\kappa_{\perp}\frac{\partial n}{\partial \mu}\right] + \frac{1}{\tau_E}\frac{\partial}{\partial T}(nT) \qquad (C\text{-}2)$$

where

$$\mu = \cos\theta$$

let

$$n(r,\mu,t,T) = R(r,t)\,\theta(\mu,t)\,T^{-\gamma} \qquad (C\text{-}3)$$

$$\kappa_{\parallel} = \kappa_0 r$$

$$\kappa_{\perp} = \kappa_1 r^2$$

$$\tau_E = \tau_0 r$$

$$\frac{\partial \Theta}{\partial t} = \kappa_1 \frac{\partial}{\partial \mu}\left[(1-\mu^2)\frac{\partial \Theta}{\partial \mu}\right] \qquad (C\text{-}4)$$

$$\frac{\partial R}{\partial t} = \kappa_0 r \frac{\partial^2 R}{\partial r^2} + (3\kappa_0 - V)\frac{\partial R}{\partial r} - \left(\frac{2V + (\gamma-1)/\tau_0}{r}\right)R \qquad (C\text{-}5)$$

The solution to C-4 subject to the intial condition of impulsive emission from a point source is well known (31, 57) giving:

$$\Theta(\theta,t) = \frac{1}{2}\sum_{n=0}^{\infty}(2n+1)e^{-n(n+1)t\kappa_1}P_n(\cos\theta) \qquad (C\text{-}6a)$$

$$\simeq \left(\frac{\theta}{\sin\theta}\right)^{\frac{1}{2}}\frac{e^{-\theta^2/4\kappa_1 t}}{\kappa_1 t} \qquad (C\text{-}6b)$$

where $P_n(\cos\theta)$ = Legendre polynomials

After a long time $\Theta(\theta,t)$ approaches a constant value of 1/2. Since we will be interested in the exponential decay phase of a flare, we will be primarily interested in the form of the radial solution to the density. Assuming R is of the form

$$R_n(r,t) = R_n(r)e^{-t/\tau_n} \tag{C-7}$$

we have from equation C-5

$$0 = \frac{d^2R_n}{dr^2} + \left(\frac{3-V/\kappa_0}{r}\right)\frac{dR_n}{dr} - \frac{2V/\kappa_0}{r^2}\left[1 + \frac{(\gamma-1)}{2V\tau_0}\right]R_n + \frac{R_n}{\tau_n\kappa_0 r} \tag{C-8}$$

$$\text{Set} \quad C = 1 + \frac{(\gamma-1)}{2V\tau_0} \tag{C-9}$$

$$\text{and let } \rho = \sqrt{\frac{r}{\kappa_0\tau_n}} \tag{C-10}$$

then

$$\frac{d^2R_n}{dr^2} = \frac{1}{4\kappa_0^2\tau_n^2}\left[\frac{1}{\rho^2}\frac{d^2R_n}{d\rho^2} - \frac{1}{\rho^3}\frac{dR_n}{d\rho}\right] \tag{C-11a}$$

$$\frac{dR_n}{dr} = \frac{1}{2\kappa_0\tau_n}\frac{1}{\rho}\frac{dR_n}{d\rho} \tag{C-11b}$$

and

$$\frac{d^2R_n}{d\rho^2} + \left[\frac{2(3-V/\kappa_0)-1}{\rho}\right]\frac{dR_n}{d\rho} + \left[4 - \frac{(8CV/\kappa_0)}{\rho^2}\right]R_n = 0 \tag{C-12}$$

let $$R_n = \rho^{\nu} v_n(\rho) \tag{C-13}$$

then $$\frac{d^2R_n}{d\rho^2} = \rho^{\nu}\frac{d^2v_n}{d\rho^2} + 2\nu\rho^{\nu-1}\frac{dv_n}{d\rho} + \nu(\nu-1)\rho^{\nu-2}v_n \tag{C-14a}$$

$$\frac{dR_n}{d\rho} = \rho^{\nu}\frac{dv_n}{d\rho} + \nu\rho^{\nu-1}v_n \tag{C-14b}$$

$$\frac{d^2v_n}{d\rho^2} + \left[\frac{2\nu+2(3-\frac{V}{\kappa_0})-1}{\rho}\right]\frac{dv_n}{d\rho} + \left[4 - \frac{\nu[\nu-1+2(3-\frac{V}{\kappa_0})-1]-8C\frac{V}{\kappa_0}}{\rho^2}\right]v_n = 0 \tag{C-15}$$

let $$\nu = V/\kappa_0 - 2 \tag{C-16a}$$

$$\eta^2 = (2-V/\kappa_0)^2 + 8C\ V/\kappa_0 \tag{C-16b}$$

then $$\frac{d^2v_n}{d\rho^2} + \frac{1}{\rho}\frac{dv_n}{d\rho} + \left[4 - \frac{\eta^2}{\rho^2}\right]v_n = 0 \tag{C-17}$$

Equation C-17 is just the familiar Bessel Equation with solutions

$$v_n(\rho) = C_1 J_\eta(2\rho) + C_2 Y_\eta(2\rho) \tag{C-18}$$

thus $$R_n(r) = r^{(V/2\kappa_0-1)}\left[C_1 J_\eta\left(2\sqrt{\frac{r}{\kappa_0\tau_n}}\right) + C_2 Y_\eta\left(2\sqrt{\frac{r}{\kappa_0\tau_n}}\right)\right] \tag{C-19}$$

and $$R(r,t) = \sum_n C_n e^{-t/\tau_n}\, r^{(V/2\kappa_0-1)}\, J_\eta\left(2\sqrt{\frac{r}{\kappa_0\tau_n}}\right) \tag{C-20}$$

where the solutions Y_η have been eliminated by the boundary condition at r = 0. The boundary condition at r = D determines τ_n in terms of the zeros of $J_\eta(x)$. Letting $j_{\eta,n}$ = n^{th} zero of $J_\eta(x)$, we have

$$\tau_n = \frac{4D}{\kappa_0 (j_{\eta,n})^2} \qquad \text{(C-21)}$$

The constants C_n can be determined from the initial condition.

Since we are interested only in the time behavior of the solution after a long time, we need only investigate the lowest order term in the sum C-20. That is

$$R(r,t) \simeq C_1 r^{(V/2\kappa_0 - 1)} J_\eta(j_{\eta,1}\sqrt{r/D}) \exp\left[-\frac{(j_{\eta,1})^2 \kappa_0 t}{4D}\right] \qquad \text{(C-22)}$$

When the observed decay is exponential, the time constant will be due to the exponential form of equation C-22 giving:

$$\tau_{decay} = \frac{4D}{\kappa_0 (j_{\eta,1})^2} \qquad \text{(C-23a)}$$

where $$\eta = 2\sqrt{(1 - V/2\kappa_0)^2 + 2CV/\kappa_0} \qquad \text{(C-23b)}$$

$$C = 1 + \frac{(\gamma - 1)}{2V\tau_0} \qquad \text{(C-23c)}$$

Appendix D

Interpretation of D1-D2 Data Plots

The D1-D2 data plots are computer generated representations of the D1 vs. D2 pulse height distribution of events analyzed by the experiment. The data are given by a plot symbol indicating the number of events with a specific D1-D2 pulse height channel pair which is listed in the appropriate location of the D1-D2 matrix. In table D-I the correspondence between the plot symbols and the number of events is given.

The D1 and D2 pulse height scales are pseudo logarithmic. Thus, the plot channels do not refer directly to actual D1 or D2 PHA channels. In table D-II the correspondence between plot channels and PHA channels is given.

TABLE D-I

INTERPRETATION OF D1-D2 PLOT SYMBOLS

Plot Symbol	Number of Events	Plot Symbol	Number of Events
1	1	I	64-79
2	2	J	80-99
3	3	K	100-124
4	4	L	125-159
5	5	M	160-199
6	6	N	200-249
7	7	O	250-319
8	8	P	320-399
9	9	Q	400-499
		R	500-639
A	10-11	S	640-799
B	12-15	T	800-999
C	16-19	U	1000-1259
D	20-24	V	1260-1589
E	25-31	W	1590-1999
F	32-39	X	2000-2519
G	40-49	Y	2520-3159
H	50-63	Z	3160- ∞

TABLE D-II

INTERPRETATION OF D1-D2 PLOT CHANNELS

Plot Ch.	PHA Ch.	Plot Ch.	PHA Ch.	Plot Ch.	PHA Ch.
1	0	21	24-25	41	85-89
2	1	22	26-27	42	90-94
3	2	23	28-29	43	95-100
4	3	24	30-31	44	101-106
5	4	25	32-33	45	107-112
6	5	26	34-35	46	113-119
7	6	27	36-37	47	120-126
8	7	28	38-39	48	127-133
9	8	29	40-42	49	134-141
10	9	30	43-45	50	142-149
11	10	31	46-48	51	150-157
12	11	32	49-51	52	158-166
13	12	33	52-54	53	167-175
14	13	34	55-58	54	176-185
15	14	35	59-62	55	186-195
16	15	36	63-66	56	196-206
17	16-17	37	67-70	57	207-217
18	18-19	38	71-74	58	218-229
19	20-21	39	75-79	59	230-241
20	22-23	40	80-84	60	242-255

REFERENCES

1. W. R. Webber, "The Modulation of Galactic Cosmic Rays by Interplanetary Magnetic Fields," in Proceedings of the Tenth International Conference on Cosmic Rays, Part A, ed. by J. R. Prescott (University of Calgary, Calgary, Canada 1967), pp 146-193.

2. E. Fermi, "On the Origin of Cosmic Radiation," Phys. Rev., 75 1169, 1949.

3. E. N. Parker, Interplanetary Dynamical Processes, Interscience Publishers, New York, 1963.

4. J. R. Jokipii and E. N. Parker, "On the Convection, Diffusion and Adiabatic Deceleration of Cosmic Rays in the Solar Wind." Astrophys. J., 160, 735, 1970.

5. J. R. Jokipii, "Propagation of Cosmic Rays in the Solar Wind," to be published in Reviews of Geophysics and Space Physics, 1971.

6. E. N. Parker, "The Passage of Energetic Charged Particles through Interplanetary Space," Planet. Space Sci., 13 9, 1965.

7. L. J. Gleeson and W. I. Axford, "Cosmic Rays in the Interplanetary Medium," Astrophys. J., 149 L115, 1967.

8. J. R. Jokipii, "Cosmic-Ray Propagation, 1, Charged Particles in a Random Magnetic Field," Astrophys. J., 146 480, 1966.

9. J. R. Jokipii, "Cosmic-Ray Propagation, 2, Diffusion in the Interplanetary Magnetic Field," Astrophys. J., 149, 405, 1967.

10. J. R. Jokipii, "Addendum and Erratum to Cosmic-ray Propagation, 1," Astrophys. J., 152, 671, 1968.

11. E. C. Roelof, "Transport of Cosmic Rays in the Interplanetary Medium," Canad. J. Phys., 46, 5990, 1968.

12. K. Hasselmann and G. Wibberentz, "Scattering of Charged Particles by Random Electromagnetic Field," Zeitschrift fur Geophysik, 34, 353, 1968.

13. W. E. Althouse et al., "A Solar and Galactic Cosmic Ray Satellite Experiment," IEEE Transactions on Nuclear Science, 15, 229, 1967.

14. S. S. Murray, "OGO-F-20 Data Format," California Institute of Technology, SRL Internal Report No. 19, 1970.

15. J. E. Lupton, private communication, 1969.

16. K. R. Symon, "Fluctuations in Energy Loss by High Energy Charged Particles in Passing through Matter," Thesis Harvard University, 1948.

17. OGO Experiment Bulletin F-52, "OGO-F Experiment Telemetry and Command Assignment," GSFC, 1967.

18. OGO Experiment Bulletin F-143, "OGO Operations Summary Report June 1969," Report No. 08672-6032-TO-00, p 5, 1969.

19. W. N. Hess, The Radiation Belt and Magnetosphere, Blaisdell Publishing Co., Massachusetts, 1968, pp 57-63.

20. E. G. Stassinopoulos, World Maps of Contours of B, L, and Flux Contours, NASA SP-3054, 1970.

21. E. Fermi, Nuclear Physics, University of Chicago Press, Chicago, 1950, pp 215-236.

22. E. C. Stone, "Time Dependence of Non-Störmer Cutoff for 1.5-MeV Protons in Quiet Geomagnetic Field," J. Geophys. Res., 69, 3577, 1964.

23. D. F. Smart, M. A. Shea and R. Gall, "The Daily Variation of Trajectory-Derived High Latitude Cutoff Rigidities in a Model Magnetosphere," J. Geophys. Res., 74, 4731, 1969.

24. R. D. Evans, The Atomic Nucleus, McGraw-Hill Book Company, New York, 1955, p 517.

25. J. F. Janni, Calculations of Energy Loss, Range, Pathlength, Straggling, etc, Tech. Report AFWL-TR-65-150, 1966.

26. G. Dearnaley, "The Channeling of Ions through Silicon Detectors," IEEE Transactions on Nuclear Science 11, 249, 1964.

27. E. F. Szajna and G. R. Stonesifer, OGO-F Data Processing Plan, GSFC X-565-69-157, 1969.

28. Environmental Data Service, ESSA, Solar-Geophysical Data, No. 299 - Part I, No. 300 - Part I, No. 304 - Part II, No. 305 - Part II.

29. R. A. Palmeira and G. F. Pieper, in Introduction to Space Science, ed. by W. N. Hess and G. D. Mead, Gordon and Breach, Science Publ., 1968, p 434.

30. F. B. McDonald, ed. Solar Proton Manual, NASA technical report, NASA-TR-R-169, 1963.

31. L. F. Burlaga, "Anisotropic Diffusion of Solar Cosmic Rays," J. Geophys. Res., 72, 4449, 1967.

32. P. R. Bevington, Data Reduction and Error Analysis for the Physical Sciences, McGraw Hill Book Company, New York, 1969.

33. E. N. Parker, "Dynamics of the Interplanetary Gas and Magnetic Field," Astrophys. J., 128, 664, 1958.

34. E. N. Parker, "Cosmic Ray Modulation by the Solar Wind," Phys. Rev., 110, 1445, 1958.

35. P. J. Coleman et al., "Measurements of Magnetic Fields in the Vicinity of the Magnetosphere and in Interplanetary Space: Preliminary Results from Mariner 4," Space Res., 6, 1966.

36. L. Davis Jr. et al., "Interplanetary Magnetic Measurements," in The Solar Wind, ed. by R. L. Mackin, Jr., and M. Neugabauer, Pergamon Press, New York, 1966, pp 35-50.

37. N. F. Ness et al., "Initial Results of the IMP 1 Magnetic Field Experiment," J. Geophys. Res., 69, 3531, 1964.

38. G. Cocconi, "On the Origin of the Cosmic Radiation," Phys. Rev., 83, 1193, 1951.

39. Ia. P. Terletskii and A. A. Logunov, "Energetic Spektr Pervichnoi Komponenti Kosmiche Skikh Luchei," J. Exptl. Theoret. Phys., (USSR), 21, 567, 1951.

40. P. Meyer, E. N. Parker and J. A. Simpson, "Solar Cosmic Rays of February 1956 and Their Propagation through Interplanetary Space," Phys. Rev., 104, 768, 1956.

41. E. N. Parker, "The Passage of Energetic Charged Particles through Interplanetary Space," Planet. Space Sci., 13, 9, 1965.

42. L. J. Gleeson and W. I. Axford, "Cosmic Rays in the Interplanetary Medium," Astrophys. J., 149, L115, 1967.

43. J. R. Jokipii and P. J. Coleman, Jr., "Cosmic Ray Diffusion Tensor and Its Variation Observed with Mariner 4," J. Geophys. Res., 73, 5495, 1968.

44. J. R. Jokipii and E. N. Parker, "Cosmic Ray Life and the Stochastic Nature of the Galactic Magnetic Field," Astrophys. J., 155, 799, 1969.

45. J. R. Jokipii, "Modulation of Low Rigidity Cosmic Rays and the Power Law Spectrum of the Interplanetary Magnetic Field in 1962 and 1965," Canad. J. Phys., 46, 5950, 1968.

46. J. R. Jokipii and E. N. Parker, "Random Walk of Magnetic Field Lines of Force in Astrophysics," Phys. Rev. Letters, 21, 44, 1968.

47. J. R. Jokipii and E. N. Parker, "Stochastic Aspects of Magnetic Lines of Force with Application to Cosmic Ray Propagation," Astrophys. J., 155, 777, 1969.

48. E. Fermi, "Galactic Magnetic Fields and the Origin of Cosmic Radiation," Astrophys. J., 119, 1, 1954.

49. L. J. Lanzerotti, "Low Energy Solar Protons and Alphas as Probes of the Interplanetary Medium: the May 28, 1968 Solar Event," J. Geophys. Res., 74, 2851, 1969.

50. M. A. Forman, "The Equilibrium Anisotropy in the Flux of 10-MeV Solar Flare Particles and Their Convection in the Solar Wind," J. Geophys. Res., 75, 3147, 1970.

51. K. G. McCracken, V. R. Rao and R. P. Bukata, "Cosmic-ray Propagation Processes, 1, a Study of the Cosmic-ray Effect," J. Geophys. Res., 72, 4293, 1967.

52. J. R. Jokipii, private communication, 1970.

53. A. H. Compton and I. A. Getting, "An Apparent Effect of Galactic Rotation on the Intensity of Cosmic Rays," Phys. Rev., 47, 817, 1935.

54. D. Intriligator, private communication, 1970.

55. M. A. Forman, "Convection-Dominated Transport of Solar Cosmic Rays," to be published, 1971.

56. D. E. Groce, "Magnetic Analysis of Reactions Leading to Excited States in Li^6 and B^{11}," Thesis, California Institute of Technology, 1963.

57. J. Feit, "Confinement of Cosmic Rays to Sectors of the Corotating Magnetic Field," J. Geophys. Res., 74, 5579, 1969.